KUOPION YLIOPISTON JULKAISUJA C. LUONNONTIETEET JA YMPÄRISTÖTIETEET 186
KUOPIO UNIVERSITY PUBLICATIONS C. NATURAL AND ENVIRONMENTAL SCIENCES 186

LASSE M. HEIKKINEN

Statistical Estimation Methods for Electrical Process Tomography

Doctoral dissertation

To be presented by permission of the Faculty of Natural and Environmental Sciences of the University of Kuopio for public examination in Auditorium, Microteknia building, University of Kuopio, on Friday 26th August 2005, at 12 noon

Department of Applied Physics
University of Kuopio

KUOPION YLIOPISTO

KUOPIO 2005

Distributor:
Kuopio University Library
P.O. Box 1627
FIN-70211 KUOPIO
FINLAND
Tel. +358 17 163 430
Fax +358 17 163 410
http://www.uku.fi/kirjasto/julkaisutoiminta/julkmyyn.html

Author´s address:
Department of Applied Physics
University of Kuopio
P.O. Box 1627
FIN-70211 KUOPIO
FINLAND
Tel. +358 17 162 350
Fax +358 17 162 373
E-mail: Lasse.Heikkinen@uku.fi

Supervisors:
Docent Marko Vauhkonen, Ph.D.
Department of Applied Physics
University of Kuopio

Professor Jari Kaipio, Ph.D.
Department of Applied Physics
University of Kuopio

Reviewers:
Professor Kyung Youn Kim, Ph.D.
Department of Electrical Engineering
Cheju National University
South-Korea

Robert G. Aykroyd, Ph.D.
Department of Statistic
University of Leeds
UK

Opponent:
Professor Markku Kataja, Ph.D.
Department of Physics
University of Jyväskylä
Finland

ISBN 951-27-0344-0
ISBN 951-27-0019-0 (PDF)
ISSN 1235-0486

Kopijyvä
Kuopio 2005
Finland

Heikkinen, Lasse M. Statistical estimation methods for electrical process tomography. Kuopio University Publications C. Natural and Environmental Sciences 186. 2005. 147 p.
ISBN 951-27-0344-0
ISBN 951-27-0019-0 (PDF)
ISSN 1235-0486

ABSTRACT

In process tomography the aim is to obtain information from the interior of the process equipments based on the measurements made on outside of the process. Various tomography techniques based on measurements of transmission, diffraction or electrical phenomena have been applied for this purpose. To date the most promising approach for process tomography involves use of electrical measurements. One this type of approach is Electrical Impedance Tomography (EIT) technique. EIT is an imaging modality in which the internal resistivity distribution is estimated based on the known injected currents and measured voltages on the surface of the object.

In this thesis, statistical estimation methods for electrical process tomography are proposed. The methods are presented from the Bayesian point of view. Four novel methods are developed. The first is an approach to estimate the electrode contact impedance which exist between a electrode and process liquid. The method is tested with two laboratory experiments. On the basis of the experiments it can be concluded that the estimation of the contact impedance improves the absolute conductivity estimates.

In the second approach, the effects of internal conductive structures on the reconstructed images in two-dimensional cases are considered. Furthermore, possible improvements in the reconstructions by taking into account the locations and resistivities of these structures are studied. It is shown that in some internal conductive structure geometries the prior information of the structure may improve the reconstructions substantially. The use of the internal structures as internal electrodes in two-dimensional cases is also studied with numerical simulations and laboratory experiments. It is shown that by utilizing internal structural information and using these internal structures as additional electrodes significant improvements in image reconstruction can be achieved.

In the third approach estimation of air volume fraction distribution is studied. The approach is tested with three-dimensional numerical simulations and laboratory experiments using air-water mixture. In the fourth approach a bulk volume fraction prior model is developed for the volume fraction estimation. Two dimensional numerical examples are used to demonstrate the proposed method. On the basis of these two approaches it can be concluded that EIT is a suitable technique for the air volume fraction estimation and the proposed prior model can assist in the estimation.

Universal Decimal Classification: 537.311.6
AMS (MOS) Classification: 62C10, 62C12, 93E10
INSPEC Thesaurus: electric impedance imaging; tomography; process monitoring; industries; Bayes methods; inverse problems; electrodes; electrical conductivity; contact resistance; electrical contacts; electric impedance; estimation theory

Acknowledgements

Work is done and now it is time for the speech of thanks. This work is carried out mainly in the Deparpment of Applied Physics, University of Kuopio during the years 1999 – 2004.

First of all I want to express my gratitude to my main supervisor Docent Marko Vauhkonen, PhD., for his excellent guidance and encouragement. I also wish to give special thanks to my second supervisor Professor Jari Kaipio, PhD., for giving me to opportunity to work in his excellent reasearch group. Without these people this thesis would have been only a naive fantasy. I also thank Professor Juhani Aittamaa, PhD., from Helsinki University of Technology and Professor Jari Käyhkö, PhD., from Lappeenranta University of Technology, for providing financial support for this work.

I want to thank the official reviewers Professor Kyung Youn Kim, PhD., and Dr. Robert G. Aykroyd, PhD., for their fruitful suggestions and comments for improving the manuscript.

I want to thank the staff in the Department of Applied Physics at the University of Kuopio for their support. Especially, I wish to thank the members of the Inverse problems research group. Many thanks to Tuomo Savolainen, MSc., for fruitful collaboration in the field of EIT hardware. Thanks to my colleague and former roommate Aku Seppänen, MSc., for many scientific and unscientific discussion during several years. Special thanks goes to Jari Kourunen, MSc. and to our student Mr. Juha Rastas. Their help have been invaluable in our EIT-laboratory. I also thank Matti Malinen, PhD. for his friendship and for giving valuable suggestions to the manuscript.

I want to thank my co-author Dr. Robert M. West, PhD., for the fruitful collaboration and for being my host during my three months visit at the University of Leeds at year 2002. I also thank my other co-authors Tanja Tarvainen, MSc. and Kimmo Leinonen for collaboration.

I want to express my invaluable gratitude to my parents Jouko and Hilkka for all support they have always given. Especially I want to thank my father for introducing me to hunting. Without this hobby my life would be unbalanced. I also warmly thank my brother Jukka for supporting me during my whole life.

Kuopio, 20 June 2005

Lasse Heikkinen

Abbreviations

2D	Two-dimensional
3D	Three-dimensional
BEM	Boundary element method
CEM	Complete electrode model
CM	Conditional mean
CT	Computerized tomography
ECT	Electrical capacitance tomography
EIT	Electrical impedance tomography
EMT	Electromagnetic inductance tomography
ERT	Electrical resistance tomography
FEM	Finite element method
GN	Gauss-Newton method
LS	Least square estimate
MAP	Maximum a posterior estimate
MCMC	Markov chain Monte Carlo method
ML	Maximum likelihood estimate
MRI	Magnetic resonance imaging
PET	Positron emission tomography
RE	Relative error
SPECT	Single photon emission computerized tomography
QMG	Finite element mesh generation package

Nomenclature

α	Regularization parameter
ϵ	Electrical permittivity
γ	Admittivity
Γ_v	Measurement noise covariance matrix
Γ_{w_t}	State noise covariance matrix
Γ_{pr}	Prior covariance matrix
$\Gamma_{x\|y}$	Conditional covariance matrix
μ	Magnetic permeability
ν	Outward unit normal
Ω	Domain
$\partial\Omega$	Boundary of the domain
ω	Angular frequency
$\pi(\cdot)$	Probability density
$\pi(\boldsymbol{f},\boldsymbol{g})$	Joint density of parameters and data
$\pi(\boldsymbol{f} \mid \boldsymbol{g})$	Posterior density
$\pi(\boldsymbol{g} \mid \boldsymbol{f})$	Likelihood density
σ	Electrical conductivity
ρ	Resistivity
ρ_c	Free charge density
$(\cdot)^T$	Transpose
$\lvert \cdot \rvert$	Absolute value
$\lVert \cdot \rVert$	Euclidean norm

$\boldsymbol{B}(\boldsymbol{x},t)$	Magnetic field
$\mathcal{B}$	Bilinear form
C, $\tilde{C}$	Normalization constant
$\boldsymbol{D}(\boldsymbol{x},t)$	Electric displacement
$\mathcal{D}$	Data space
det	Determinant
$\boldsymbol{E}(\boldsymbol{x},t)$	Electric field
$E(\cdot)$	Expectation
$E_{x\|y}$	Conditional expectation
$\boldsymbol{f}$	Stationary parameter vector
F	Cumulative distribution function
$\boldsymbol{g}$	Stationary data vector
$\boldsymbol{g}(t)$	Nonstationary data vector
$\boldsymbol{H}(\boldsymbol{x},t)$	Magnetizing field
I	Identity matrix or current pattern
$\mathtt{i}$	Imaginary unit

J	Jacobian
$\boldsymbol{J}$	Current density
$\boldsymbol{J}_{\mathrm{ohm}}$	Ohmic current
$\boldsymbol{J}_{\mathrm{s}}$	Current source
$K(\cdot)$	Forward operator
k	Time index
L	Number of the electrodes
$\mathcal{M}$	Parameter space
$\mathcal{M} \times \mathcal{D}$	Joint space of parameters and data
$N(x^*, \Gamma_x)$	Normal distribution with mean x^* and covariance Γ_x
P	Probability measure
S	Minimization functional or electrode surface
$\mathbb{R}^m$	m-dimensional real space
R	Correlation matrix
$\mathcal{R}$	Resistivity matrix
t	Time
$u(r)$	Electrical potential
$\boldsymbol{U}$	Voltages on the electrodes
$U(\cdot)$	Mapping between conductivity and voltage
$\boldsymbol{v}$	Noise vector
$\boldsymbol{V}$	Voltage data vector
W	Regularization energy functional
x	Spatial coordinate
z_ℓ	Electrode contact impedance

Contents

1 Introduction **13**

2 Modelling for process tomography **17**
2.1 Introduction 17
2.2 Electrical tomography techniques 19
2.2.1 Process applications of electrical tomography 20
2.3 Estimation methods for process tomography 21

3 Electrical impedance tomography (EIT) **31**
3.1 Introduction 31
3.2 Forward modelling of EIT 33
3.2.1 Observation model 33
3.3 Stastistical inversion in EIT 44
3.3.1 Likelihood density 44
3.3.2 Priors for EIT 45
3.3.3 Posterior density and solution strategies 51
3.4 Measurement strategies 54
3.4.1 Current injection 54
3.4.2 Voltage measurement 57

4 Estimation of contact impedance **58**
4.1 Introduction 58
4.2 Estimation procedure 59
4.2.1 Computation of the Jacobian with respect to the contact impedance 61
4.3 Laboratory experiments 62
4.3.1 First experiment 63
4.3.2 Second experiment 64
4.4 Summary 67

5 Internal structures **70**
5.1 Introduction 70
5.2 Prior models for known structures and resistivities 70

5.3 Numerical simulations 71
    5.3.1 Air-core imaging of the mixing vessel 74
    5.3.2 Connected conductive structures 76
5.4 Summary 84

6 Internal electrodes 87
6.1 Introduction 87
6.2 Internal electrodes and current patterns in EIT 88
6.3 Numerical simulations 88
6.4 Laboratory measurements 91
    6.4.1 Results of the reconstructions 94
    6.4.2 Anisotropic prior 98
6.5 Summary 98

7 Volume fraction estimation 99
7.1 Introduction 99
7.2 Tomographic estimation of volume fraction distribution 100
    7.2.1 Estimation of volume fraction distribution using EIT 101
    7.2.2 Conductivity models for dispersion 102
    7.2.3 The MAP estimation 103
7.3 Numerical simulations 104
    7.3.1 3D simulation 104
    7.3.2 Effect of conductivity contrast 105
7.4 Laboratory experiment 112
7.5 Summary 116

8 Volume fraction prior model 119
8.1 Introduction 119
8.2 Bulk volume fraction prior model 119
8.3 Numerical examples 120
8.4 Summary 128

9 Conclusions 133

A Proof of the equation (8.5) 135

References 137

Chapter I

Introduction

There is a growing need for the analysis of the internal characteristics of process plants in order to improve the design and operation of process equipments [185]. Roughly speaking a common factor in the process equipments is that multiphase system or flow usually occur within them. Unfortunately, the methodologies used for design and use of the process equipments are largely based on intuition or rules of thumb rather than on first principles. This is due to insufficient knowledge on theory of multiphase systems. In order to develop sophisticated models for multiphase systems reliable experimental data is extremely important. The experimental data is needed both for verification of the existing models and for developing new ones. In this case, measurements are applied to process at laboratory and pilot scales. Furthermore, another important goal is to use the experimental data for process monitoring and control, and the aim is to install measurement system in industrial scale process plants. Nature of the multiphase systems impose the requirements for an applicable measurement system.

The measurement system is required to operate in dynamic multiphase systems and to provide the required data over the entire region of interest. In other words both temporal and spatial information on the behavior of the processes is essential. In addition, the measurement system is supposed to be *non-invasive* and *non-intrusive* [202]. Non-invasivity means that the measurement sensors are located outside the process. This requirement is essential since sensor that is placed within the process might disturb the operation of the process and hence the measurements might be more or less erroneous. Non-intrusivity means that sensors do not enter into the wall of the equipment. The advantage of this is that any specific structural changes for the equipment do not have to be performed. These requirements restrict the use of the traditional sensor technologies whereas the tomographic imaging technique mainly fulfill these requirements. In principle, tomographic techniques that can be used in industry are essentially the same techniques that are used as daily clinical tools in medicine.

The basic idea of tomography is to use a number of sensors installed around the process equipment. The sensors are sequentially energized and other sensors are used to collect a projection of data. The source of the energy is then moved to another position and projected data is again measured. This procedure is repeated until a whole frame of data is acquired. The output signals of the sensors depend on the material distribution within the equipment. A computer is used to compute a tomographic image from the measured data set. The image is not necessarily the goal in the imaging system, since more relevant information can be estimated from the image as well. For example, in mixing application a mixing index with respect to different process variables can be estimated [184]. This allows one to provide information of the quality of mixing and hence the mixer efficiency can be studied. It should be emphasized here that mainly all applications in which the tomographic methods are used are inherently three-dimensional. This feature should be taken into account in the design of the tomographic measurements and in the reconstruction procedure. The tomographic image should therefore be reconstructed rather in three-dimensional space than in two-dimensional one.

All tomography techniques fall into the class of indirect measurements. This means that interesting unmeasurable process quantity is estimated based on measurable quantity measured around the process equipment under investigation. In many cases and also in the case of tomography this estimation problem is called the *inverse problem.* Inverse problems, in general, have two interesting features. They are often *non-local* and/or *non-causal* [88]. The non-locality means in the case of tomography techniques that the measured observations depend on the material changes over the entire region of interest. The non-causality means in terms of tomography that small changes in the material distribution within the equipment may not cause detectable change in the measurement, at least within the accuracy limit of the measurement. In other words, infinitely many material distribution can produce identical observation. Mentioned features imply that the solution of the inverse problem is not so straightforward and special attention therefore has to be given to the solution strategy. A careful analysis of the measurement system and quantity of interest have to be performed in order to extract all possible information that could be used in the solution of the problem.

Natural way to formulate the inverse problem is the *statistical inversion theory* which solves the problem in such a way that all possible information available is properly taken into account. Statistical inversion theory is based on Bayesian statistic which allows one to model all quantities (both observable and unobservable) as random variables. The solution of the inverse problem therefore is not a single estimate but a probability distribution that can be used to produce estimates as well as to evaluate their reliability.

A variety of tomographic methods have been developed for the purpose of the industrial applications [185, 202]. The tomography techniques can be divided roughly into two categories, *diffuse* and *non-diffuse* imaging techniques. Common medical x-ray tomography can be mentioned as an example of non-diffuse techniques. This thesis concentrates on electrical tomography techniques called *electrical impedance tomography* (EIT) that belong to the class of diffuse techniques. EIT is based on the use of relatively low frequency electromagnetic fields. The main difference between the diffusion and non-diffusion based techniques is in the the spatial resolution and the imaging rate of the techniques

Electrical tomography techniques like all the other techniques can be used to estimate *qualitative* or *quantitative* information on the current state of the process. The estimation methods of the qualitative and quantitative imaging methods are different. Usually the qualitative methods are tolerant of the modeling errors but the methods give rather vague qualitative than strictly absolute information. When absolute information of the process quantity is necessary the quantitative method have to be used. In this case special attention has to be given to the modeling of the whole measurement situation. All essential features of the measurement system, process equipment and process quantity have to be taken into account in the estimation. This thesis is concentrated on these issues.

THE AIMS AND CONTENTS OF THE THESIS

The aim of this thesis is to develop EIT estimation methods for industrial applications. More precisely, there are four main aims in this thesis. The first aim is to develop a method for contact impedance estimation. The contact impedance exist between a metal electrode and liquid. Poor knowledge of it may cause considerable errors in the estimation of the conductivity distribution. The second aim is to study the effects of the internal structures within the vessel to the estimation of the conductivity distribution as well as to propose a method to avoid these effects. Also, the feasibility of the use of these structures as internal electrodes is studied. The third aim is to develop a method for the estimation of air volume fraction distribution using EIT. The fourth aim is related to the air volume fraction estimation and the aim is certain type of prior model in which the bulk air volume fraction is taken into account. A common factor in these aims is that all proposed methods can be presented in the Bayesian framework.

Some of the results of this thesis have already been published in the articles [69, 70, 71, 73, 72]. This thesis not only summarizes the results of the published works but also gives a more precise theoretical background of the proposed methods based on the statistical inversion theory. There are also some unpublished studies in this thesis.

This thesis is divided into 9 chapters. In Chapter 2, principles of tomography are presented. Also, a short review on the tomographic techniques used in process industry is given. The main emphasis is on the electrical tomography methods. The process applications and quantities that are studied using electrical methods are also reviewed. After that, estimation methods for tomography techniques are discussed. The estimation methods are presented from the Bayesian point of view. This chapter forms a solid methodological ground for thesis.

In Chapter 3, electrical impedance tomography (EIT) method is presented. The chapter begins with an introduction of the method. The forward and inverse problems are outlined next, followed by the introduction of typical prior models of EIT. Furthermore, the finite element solution of the forward problem is discussed and some forward problem simulations are shown. In this thesis absolute reconstruction methods are mainly considered in which the forward problem is solved using finite element method. Traditional and popular qualitative methods are therefore omitted.

A method for the estimation of the electrode contact impedance is presented in Chapter 4. The basic principles of the method are introduced and it is tested with laboratory experiments. Two experiments are studied. In the first one, the performance of the method for a tank filled with homogeneous liquid is studied. In this case, a single parameter for the contact impedances is used. In the second one, the method is tested with a single target within the tank. In this case, the contact impedances on all the electrodes are estimated.

In Chapter 5, the effects of internal conductive structures on the reconstructed images in two-dimensional cases are considered and possible improvements in the reconstructions by taking into account the locations and resistivities of these structures are studied. Studies are performed with the aid of numerical simulations. The case of two internal structures are considered.

In Chapter 6, the modeling of certain types of internal structures and using them as internal electrodes in two-dimensional case are considered. The proposed method is applied to two different internal electrode configurations. These methods are tested with numerical simulations and laboratory experiments. The results are compared qualitatively and quantitatively with traditional EIT, which is based on boundary measurements only.

In Chapter 7, air volume fraction estimation using EIT is presented. The estimated quantity in EIT is electrical conductivity distribution, hence the model between local conductivity and the volume fraction have to be used. The proposed method is tested with two- and three-dimensional numerical simulations. In the simulations, the performance of the method and the effect of the internal electrode to the accuracy of the reconstructed quantity are studied. Finally, at the end of chapter, difference reconstruction based method is tested with a laboratory experiment. In the experiment, the behavior of the three-dimensional gas-liquid mixture is studied.

In Chapter 8, bulk volume fraction prior model is presented. The prior model can be utilized in the method presented in Chapter 7. An idea behind this prior is that the bulk volume fraction within some equipment is a priori known and this knowledge is included in the estimation. Two-dimensional numerical examples are used to demonstrate the proposed method. Finally, in Chapter 9 overall discussion and conclusions of the thesis are given.

CHAPTER II

Modelling for process tomography

2.1 Introduction

The word tomography comes from the Greek words *tomos* meaning “slice” and *graph* meaning “image” [185]. In other words, tomography is an imaging technique in which the objective is to get an image on the cross section slice of an object. The image can involve information either on spatial or temporal features of the object. One image is adequate in the first case whereas in the second case a sequence of images with respect to time is necessity. Nowadays, it is usual that the image is three-dimensional rather than a two-dimensional slice.

Basic principle of tomography is following. Some form of energy is transmitted to the object on predetermined positions. The projection of the energy around the object is measured. The collected projection depends on the properties of the interior of the object. In other words, if the material within the object interacts with the energy that is used, the variation in the projection can be detected. Unfortunately, one projection does not carry enough information to obtain a tomographic image. Additional projections therefore have to be collected by rotating either the object or the measurement system/position. After sufficient amount of projections, reliable information can be produced based on a set of projections, knowledge of the position of the energy sources/detectors and the intensity of the sources.

The necessary components of any tomography system are shown in Figure 2.1. The system consist of hardware and software parts. The hardware part of the system is responsible for the data acquisition including sensors and the control of the sources and measurement units. The image reconstruction, displaying and interpretation of the results are performed in the software part of the system. In some systems software can also produce a control signal to the hardware part or to the object itself. In the first case, the measurement system is tuned adaptively based on the previous measurements. In the second case, which is a relevant situation in industrial applications, the objective is to use tomography system as a control system of process equipments.

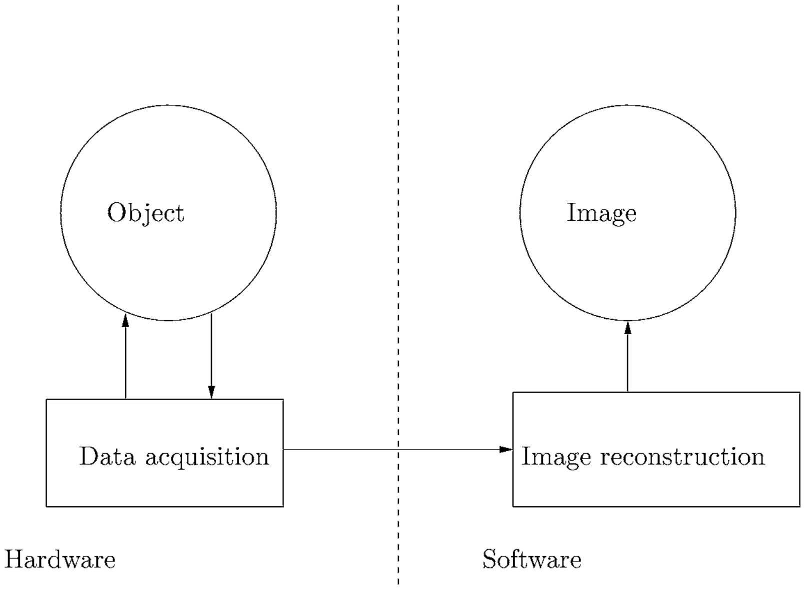

Figure 2.1: Basic components in tomography system.

The roots of the tomography goes back to the 19th century. A Norwegian physicist Niels Henrik Abel proposed an idea of tomography for an object with axi-symmetrical geometry in 1826 [107]. The Abel's work was purely mathematical and it was further developed for objects with arbitrary geometry by an Austrian mathematician Johann Radon in 1917 [93]. He introduced a mathematical method called *Radon transform* which formed theoretical ground for almost all tomography techniques. Godfrey Hounsfield and Allen Cormack developed a computer assisted tomography (CAT) for medical purposes in the early-1970s and they were awarded the Nobel prize in 1979 for this pioneering work [93].

The aim of the early works was to develop the imaging tool for medical purposes. However, it was realized quite soon that the concept of tomography is not restricted only to the medical field. Tomography techniques have therefore been developed for numerous industrial applications. The requirements in industrial applications differ from those of medical applications. For example, high speed imaging is usually required in industrial applications and safety constraints are not so restrictive. The industrial applications are discussed in more detail later in this chapter. Active process tomography research started in UK in the mid-1980s. This research led to the workshop series in early-1990s which were held in Manchester, UK [2], Karlshure, Germany [3], Oporto, Portugal [4] and Bergen, Norway [5]. After these meetings two conferences were held in USA [6] and in Netherlands [7]. The series of the World Congress on Industrial Process Tomography (WCIPT) was started in 1999 when the first meeting was held in Buxton, UK [8]. This was followed by meetings in Hannover, Germany [9] and Banff, Canada [10]. The next

Table 2.1: The ranges of the material properties of the electrical tomography techniques [202].

Modality	Conductivity σ (S/m)	Permittivity ϵ_r	Permeability μ_r
EIT/ERT	10^{-1} – 10^{7}	10^{0} – 10^{2}	–
ECT	$<$ 10^{-1}	10^{0} – 10^{2}	–
EMT	10^{2} – 10^{7}	–	10^{0} – 10^{4}

meeting of this series will be held in Aizu, Japan in September 2005. In addition a meeting concentrated on process imaging for automatic control was held in Boston in 2000 [127].

As discussed in Introduction, tomography techniques can be divided in two categories: *non-diffuse* and *diffuse* tomography techniques. Usually the techniques that belong to the first class are called *hard-field* techniques and the techniques that belong to the second class are called *soft-field* techniques. The main difference between these techniques is that in the soft-field techniques the "energy lines" are bended at the interfaces of different materials whereas in the hard-field techniques this does not happen. From the reconstruction point of view this means that the reconstruction in the soft-field techniques is nonlinear problem. In this thesis a soft-field technique called electrical impedance tomography is studied and hence the hard-field techniques are omitted. Information on the hard-field techniques can be found for example in [185, 59, 35, 183].

2.2 Electrical tomography techniques

Electrical tomography techniques provide information on the electrical characteristics of the object. The techniques can be divided in three categories based on electrical quantities of the imaged object, see Table 2.1. These quantities are the *magnetic permeability* μ, *electric permittivity* ϵ and *electric conductivity* σ. The relationships of these quantities are based on the Maxwell's equations [113].

In EIT the quantity to be imaged is actually the *impedivity* which is the inverse of the *admittivity*, including both the electric conductivity and permittivity. EIT is discussed later in Chapter 3. In some situations the real part of the impedivity may dominate in which case the sensing technique is called *electrical resistance tomography* (ERT) [44].

When the imaginary part of the admittivity dominates the technique is called *electrical capacitance tomography* (ECT) which is based on the measurements of the mutual capacitance [191]. The basic idea of the ECT measurement system is to produce an electric field within the object by setting the potentials of the electrodes. The mutual capacitance measurements are performed by changing the potentials of some or all the electrodes and measuring the induced charges [136]. The permittivity distribution within the object can be reconstructed on the basis of the charge measurements. The measurement and reconstruction methods of ECT are widely studied in the past two decades, see for example [82, 194, 193, 21, 196, 191, 83, 95, 96, 192, 199, 136, 201, 198, 197, 200, 81, 62].

In the case in which the magnetic permeability is the dominant quantity the preferred method is *electromagnetic inductance tomography* (EMT) which is based on the measurement of complex mutual inductance [140]. The basic idea of EMT system is as follows. The object is excited by a number of sinusoidal magnetic fields using excitation coil(s) and the field components for each excitation patterns are measured using the sensing coils. After the measurements the magnetic permeability within the object can be reconstructed on the basis of the measured real and imaginary parts of both radial and tangential vector field components [186]. More information on EMT can be found for example in [151, 186, 64, 161].

2.2.1 Process applications of electrical tomography

The electrical tomography process applications studied so far can be divided in three categories: *mixing*, *separation*, and *flow and transportation*. Normally information on the distribution of different materials, the flow regime or the time- or space-averaged value of some process variable is of interest [185].

MIXING

In order to improve the design and operation of stirrer tanks it is important to know the mixing behavior inside these tanks as exactly as possible. The mixing of solids, liquids and gases within the liquid filled tanks has therefore been widely studied in literature, see Table 2.2. Since the background medium is usually conductive liquid, EIT is a suitable modality for such cases. The studies are concentrated on quantifying the mixer behavior for different process variables (e.g. stirrer speed, impeller type, particle type/size or solid concentration) of a gas-liquid and miscible liquid mixture. Also, transient behavior and mixing kinetics are studied with EIT. Tomography measurements have also been used for the developing of mixing models. The mixing applications in which electrical tomography techniques have been used are shown in Table 2.2.

SEPARATION

Different types of separators are widely used in industry e.g. the hydrocyclones, dense medium separators (DMS) and flotation cells that are used in mineral processing industry. The separators are usually used for solid-solid, solid-liquid and liquid-liquid mixtures and hence the selection of an appropriate tomography modality is governed by the nature of the background medium. For the separation studies both EIT and ECT have therefore been used. The efficiency of the separators is an important factor in practice. The efficiency can be improved by studying the operation of the separators using tomography techniques. The dynamic behavior of the air core within the separators for different flow rates have therefore been studied. The separation studies are also shown in Table 2.2.

FLOW AND TRANSPORTATION

Perhaps the most important application of the electrical tomography techniques is the monitoring of multi-phase flows in process equipments. There are numerous applications in industry in which the multi-phase flows have significant role. Although the theory of multi-phase flows is widely studied [74, 110] the need of accurate flowmeters still exist. For example, the component fractions of different phases, the mixture's volumetric flow rate or the mass flow rate are of interest [144]. For the flow measurements all electrical tomography techniques have been used. One of the interesting quantities is the velocity distribution which is traditionally estimated using the cross correlation technique [22, 45]. Recently a technique for the velocity field estimation based on state estimation approach has been developed [154].

Another interesting application of the electrical tomography techniques is the monitoring of the flow regimes during hydraulic and pneumatic transport [162]. The hydraulic and pneumatic transportation lines are usually used for the transportation of the solid-liquid and solid-gas mixtures. Also in these cases the concentration and velocity distributions are of interest. The total mass transfer can be estimated on the basis of these distributions. The applications of flow and transport measurements are shown in Table 2.2. There are also other applications in the table that do not fall into the above mentioned categories.

2.3 Estimation methods for process tomography

In this section, the mathematical basis of tomography techniques is presented. Basically, all tomography techniques can be considered as an estimation problem. In this thesis, the estimation is presented from the Bayesian point of view which is based on the probability theory. The basic definitions of the probability theory used in this thesis are not included here, instead a general reference is given [138]. The methodology presented in this section is appropriate for all type of tomography techniques and therefore general notations are used.

Let us assume that the interesting process quantity $f(\boldsymbol{x})$ is parametrized and it can be described using a finite set of parameters. Thus, within the domain $\Omega \in \mathbb{R}^3$ an unknown quantity is identified by a vector-valued random variable $\boldsymbol{f} = (f_1, f_2, \dots, f_m)^T \in \mathbb{R}^m$. The quantity can be represented in the form

$$f(\boldsymbol{x}) = \sum_{i=1}^{m} f_i \varphi_i(\boldsymbol{x}), \tag{2.1}$$

where $\varphi_i(\boldsymbol{x})$ are some known basis functions, not specified at this stage. The corresponding space $\mathbb{R}^m$ is called *a parameter space* and it is denote here by $\mathcal{M}$. The space is equipped with the probability measure, that is, with the function $P : \mathcal{M} \rightarrow [0\ 1]$. Note that every single parameter $f_i, i = 1, \dots, m$ has continuous probability density function although the original quantity $\boldsymbol{f}$ is discretized. Since the parameters f_i characterize the quantity completely (in some sense) they are of the primary interest. Unfortunately, in practice, those parameters cannot be

Table 2.2: A summary of industrial applications of the electrical process tomography techniques.

	Application	**Modality**	**References**
Mixing	Slurry mixing	ERT	[189]
	Gas-liquid mixing	ERT	[179]
	Stirred mixing	ERT	[120, 121, 143]
	Stirred macro-mixing	ERT	[75]
	Miscible liquid mixing	ERT	[46, 122]
	Mixing models	ERT	[123]
Flow & transport	Two-phase flow	ERT/ECT	[117, 196] [194, 193, 191, 192]
	Slurry conveying	ERT	[54]
	Gas-liquid flow	ERT	[85, 86]
	Gas-oil flow	ECT	[195]
	Migration of particles	ERT	[33]
	Gas-solid flow	ECT	[48]
	Fluidized bed	ECT	[118, 119, 180] [49, 50]
	Oil pipeline	ECT	[201]
	Molten steel flow	EMT	[25]
	Angular velocity	ERT	[52]
	Radial flow fixed reactor	ERT	[26]
	Solids conveying	ERT/ECT	[115]
Separation	Deoiling hydrocyclone	ERT	[24]
	Hydrocyclone	ERT	[187, 67]
		ECT	[188]
Others	Combustion	ECT	[181]
	Foam density	ERT	[178]
	Filtration	ERT	[42]
	Imaging of foams	ECT	[23]

directly measured. To obtain information on the parameters f_i some tomographic measurements therefore have to be performed. These measurements are denoted by a vector $\boldsymbol{g} = (g_1, g_2, \ldots, g_n)^T \in \mathbb{R}^n$ and it is called *a data vector* or *data* for short. Also this vector is assumed to be a random variable. The randomness of this vector is thought to be due to the measurement noise $\boldsymbol{v}$. The space of the measurements is called *a data space* and it is denote here by $\mathcal{D}$. The parameter and data vectors have a joint density $\pi(\boldsymbol{f}, \boldsymbol{g})$ in the joint space $\mathcal{M} \times \mathcal{D}$. The data vector, the model parameters and the measurement noise are tied together through a model

$$\boldsymbol{g} = K(\boldsymbol{f}, \boldsymbol{v}), \tag{2.2}$$

where $K : \mathcal{M} \times \mathbb{R}^n \to \mathcal{D}$ is a known deterministic function modeling the measurements. The K is the so called *observation operator.* Moreover, $\boldsymbol{v} \in \mathbb{R}^n$ is the noise vector with the measurement noise covariance matrix Γ_v. The equation (2.2) is called *the observation model.* Most often the noise is assumed to be additive and mutually independent of the unknown parameters. Hence the model (2.2) can be written in the form

$$\boldsymbol{g} = K(\boldsymbol{f}) + \boldsymbol{v}, \tag{2.3}$$

which is called *additive observation model.* The additive noise model is not always an adequate one, and more complicated noise models have also been therefore studied, see e.g. [88].

From the statistical point of view, the objective in every tomography technique is to make a statistical inference about the model parameters $\boldsymbol{f}$ based on the noisy measurement $\boldsymbol{g}$ made on the boundary of the object. The inference is also based on the mathematical model (2.3) and on prior information on the parameters. This inference is called the *inverse problem.* The prior information can be either temporal and/or spatial information. The solution strategies can be divided into two categories depending on the time dependence of the parameters.

In the case in which the parameters are non-stationary the evolution of the parameters has to be taken into account. This can be done using the state-space representation of the estimation problem [14]. Traditional solution technique for the non-stationary problems is *Kalman filter* technique which is out of scope of this thesis. The technique is widely used in both medical [169, 92, 172, 173] and industrial applications [157, 153, 155, 156, 154, 152, 99, 100] of tomography. From now on the focus of discussion is on the stationary estimation problem.

STATIONARY ESTIMATION PROBLEM

In some cases the parameters are truly stationary or stationarity with respect to measurement time can be assumed. In this case a key assumption is that $\boldsymbol{f}_t = \boldsymbol{f}_{t-1}$, $\forall\ t$. The time evolution of the parameters can therefore be omitted and the problem can be modeled by the equation (2.3).

In the stationary case the inference is based on measured noisy data $\boldsymbol{g}$, on mathematical model (2.3) and on spatial prior information on the sought parameter. More precisely it is based on the *Bayes law* [128]

$$\pi(\boldsymbol{f} \mid \boldsymbol{g}) = \frac{\pi(\boldsymbol{g} \mid \boldsymbol{f})\pi(\boldsymbol{f})}{\pi(\boldsymbol{g})}, \tag{2.4}$$

where $\pi(\boldsymbol{f} \mid \boldsymbol{g})$ is the *posterior density*, that is, the conditional probability density of the parameter $\boldsymbol{f}$ given the data $\boldsymbol{g}$. The density $\pi(\boldsymbol{g} \mid \boldsymbol{f})$ is the *likelihood density.* The density $\pi(\boldsymbol{f})$ is the *prior density.* This density contains all possible information on the parameters *before* the measurements. The density $\pi(\boldsymbol{g})$ is the *normalization constant* and sometimes it is called *evidence* [158]. This density is of the form

$$\pi(\boldsymbol{g}) = \int_{\mathcal{M}} \pi(\boldsymbol{g} \mid \boldsymbol{f})\pi(\boldsymbol{f})\mathrm{d}\boldsymbol{f}. \tag{2.5}$$

In most cases the density $\pi(\boldsymbol{g})$ is difficult to determine, but fortunately the posterior density can often be considered in the non-normalized form

$$\pi(\boldsymbol{f} \mid \boldsymbol{g}) \propto \pi(\boldsymbol{g} \mid \boldsymbol{f})\pi(\boldsymbol{f}). \tag{2.6}$$

In the following sections, the likelihood and prior densities are discussed in more detail.

LIKELIHOOD DENSITY

The likelihood density $\pi(\boldsymbol{g} \mid \boldsymbol{f})$ in the equation (2.6) is a conditional probability density of the measurement $\boldsymbol{g}$ given the parameters $\boldsymbol{f}$. The density is based on the observation model (2.3). It can be shown that the likelihood density can be written in the form [128, 104]

$$\pi(\boldsymbol{g} \mid \boldsymbol{f}) = \pi_v(\boldsymbol{g} - K(\boldsymbol{f})), \tag{2.7}$$

where $\pi_v(\cdot)$ is the probability density function of the measurement noise $\boldsymbol{v}$. It is assumed here that the parameters $\boldsymbol{f}$ and noise $\boldsymbol{v}$ are independent. Usual assumption in practice is that the noise probability density is Gaussian, that is,

$$\pi_v(\boldsymbol{v}) = \frac{(\det \Gamma_v)^{-1/2}}{(2\pi)^{n/2}} \exp\Big(-\frac{1}{2}(\boldsymbol{v} - \boldsymbol{v}^*)^T \Gamma_v^{-1}(\boldsymbol{v} - \boldsymbol{v}^*)\Big), \tag{2.8}$$

where $\det \Gamma_v$ denotes the determinant of the measurement noise covariance matrix Γ_v. Moreover, $\boldsymbol{v}^*$ is the expectation of the noise. According to equation (2.7) likelihood density function can be written in the form

$$\pi(\boldsymbol{g} \mid \boldsymbol{f}) = \frac{(\det \Gamma_v)^{-1/2}}{(2\pi)^{n/2}} \exp\Big(-\frac{1}{2}(\boldsymbol{g} - K(\boldsymbol{f}) - \boldsymbol{v}^*)^T \Gamma_v^{-1}(\boldsymbol{g} - K(\boldsymbol{f}) - \boldsymbol{v}^*)\Big). \tag{2.9}$$

In practice, if there are no systematic errors in the measurements, it can be assumed that the expectation of the noise $\boldsymbol{v}^*$ is zero, in other words $\boldsymbol{v} \sim N(0, \Gamma_v)$. This assumption is also done in this thesis.

Note that in the radiation based tomography techniques with low count measurements, the measurements are Poisson distributed. In these cases, the probability density of the measurement noise should therefore be Poisson density rather than the Gaussian one, see for example [88]. It should also be noted that the modeling errors of the observation model (2.3) can be included in the likelihood density [163, 88]. In this case the covariance matrix Γ_v can be written in the form $\Gamma_v = \Gamma_{\text{noise}} + \Gamma_{\text{error}}$, where Γ_{noise} and Γ_{error} are the covariance matrices of the measurement noise and modeling error, respectively.

PRIOR DENSITY

The key question in the solution of the estimation problem is how to choose the prior information. As discussed above, the prior information on the sought parameters is included in the prior density $\pi(\boldsymbol{f})$. The prior probability density used in this thesis can be written in the form

$$\pi(\boldsymbol{f}) = C \exp(-\alpha W(\boldsymbol{f})), \tag{2.10}$$

where $\alpha \in \mathbb{R}_+$ is the *regularization parameter*, $W(f)$ is the regularizing functional and C is a normalization constant. A challenging problem, related to the prior, is how to translate qualitative information into the form of the probability density. In principle, typical parameters should have high probability while atypical ones should have low probability. Typical statistical prior information is the variance of the parameters and correlation between the parameters. Nature of the prior density depends on the choice of the regularizing functional $W(\boldsymbol{f})$. In the case in which the prior density is identically constant, the prior density is said to be *uninformative*. This means that all parameters have the same probability and hence there is no any information on the parameters before the measurements. The prior density might also be *partially uninformative*, which means that the prior density is uninformative in "certain direction" in the parameter space $\mathcal{M}$.

A common choice for the regularizing functional is a functional

$$W(\boldsymbol{f}) = \|L(\boldsymbol{f} - \boldsymbol{f}^*)\|_q^p, \tag{2.11}$$

where L is a *regularization matrix* and $\boldsymbol{f}^*$ is a prior estimate for $\boldsymbol{f}$. Moreover, $p = 1, 2$ and $q = 1, 2, \infty$. If $p = q = 2$, the functional is a quadratic functional and the equation (2.10) can be written in the form

$$\begin{aligned} \pi(\boldsymbol{f}) &= \tilde{C} \exp\Big(-\alpha \|L(\boldsymbol{f} - \boldsymbol{f}^*)\|_2^2\Big) && (2.12) \\ &= \tilde{C} \exp\Big(-\frac{1}{2}(\boldsymbol{f} - \boldsymbol{f}^*)^T \Gamma_{\mathrm{pr}}^{-1} (\boldsymbol{f} - \boldsymbol{f}^*)\Big), && (2.13) \end{aligned}$$

where $\Gamma_{\mathrm{pr}}^{-1} = 2\alpha L^T L$ and $\tilde{C} = ((2\pi)^m \det(\Gamma_{\mathrm{pr}}))^{-1/2}$. It can be seen that this is Gaussian probability density with the mean $\boldsymbol{f}^*$ and covariance Γ_{pr}. In other words, the choice of the quadratic regularization functional leads to the Gaussian prior model. Different kind of Gaussian priors can be obtained by choosing the mean $\boldsymbol{f}^*$ and/or the covariance matrix Γ_{pr} depending on application. Typical prior models in the case of electrical impedance tomography are discussed in Section 3.3.2. New prior models for tomography are also developed in this thesis and are presented in Chapters 5 and 8.

POSTERIOR DENSITY

According to the non-normalized form of the Bayes law (2.6), the posterior probability density in the parameter space $\mathcal{M}$ can be written in the form

$$\pi(\boldsymbol{f} \mid \boldsymbol{g}) \propto \exp\Big(-\frac{1}{2}\Big((\boldsymbol{g} - K(\boldsymbol{f}))^T \Gamma_v^{-1} (\boldsymbol{g} - K(\boldsymbol{f})) + (\boldsymbol{f} - \boldsymbol{f}^*)^T \Gamma_{\mathrm{pr}}^{-1} (\boldsymbol{f} - \boldsymbol{f}^*)\Big)\Big). \tag{2.14}$$

Formally, the posterior density is the statistical solution of the stationary estimation problem. Although, the posterior density fully characterizes the solution of the estimation problem, in high dimensional problems it is inconvenient in practice. Usually some point estimates from the posterior density are calculated which are then visualized in some mesh and that is considered as a "tomographic image".

POINT AND INTERVAL ESTIMATES

The most often used point estimates are the *Maximum likelihood* (ML), *Maximum a Posterior* (MAP) and *Conditional Mean* (CM). A typical spread estimate is the *conditional covariance* and a typical interval estimate is the *credibility interval.*

Let us start discussion on the point estimates from the ML-estimate, which satisfy the following criterion [128]

$$\pi(\boldsymbol{g} \mid \boldsymbol{f}_{\mathrm{ML}}) \geq \pi(\boldsymbol{g} \mid \boldsymbol{f}), \quad \forall \quad \boldsymbol{f}. \tag{2.15}$$

In other words, $\boldsymbol{f}_{\mathrm{ML}}$ maximizes the likelihood density (2.9) for a given data $\boldsymbol{g}$. Maximization of the likelihood function

$$\pi(\boldsymbol{g} \mid \boldsymbol{f}) \propto \exp\left(-\frac{1}{2}(\boldsymbol{g} - K(\boldsymbol{f}))^T \Gamma_v^{-1} (\boldsymbol{g} - K(\boldsymbol{f}))\right) \tag{2.16}$$

can be seen as the minimization of the exponent. Therefore the following minimization problem has to be solved

$$\min_{\boldsymbol{f}} \{(\boldsymbol{g} - K(\boldsymbol{f}))^T \Gamma_v^{-1} (\boldsymbol{g} - K(\boldsymbol{f}))\}. \tag{2.17}$$

Note that any prior information is not used. If the observation model (2.3) is linear, that is,

$$\boldsymbol{g} = K\boldsymbol{f}, \text{ where } K \in \mathbb{R}^{n \times m}, \tag{2.18}$$

it can be shown that the solution is [163, 128]

$$\boldsymbol{f}_{\mathrm{ML}} = [K^T \Gamma_v^{-1} K]^{-1} [K^T \Gamma_v^{-1} \boldsymbol{g}]. \tag{2.19}$$

The ML-estimate can also be understood so that one actually maximizes the posterior density with uninformative prior density and therefore the likelihood density corresponds to the posterior density i.e. $\pi(\boldsymbol{g} \mid \boldsymbol{f}) \equiv \pi(\boldsymbol{f} \mid \boldsymbol{g})$. The posterior probability density can therefore be written in Gaussian form [163, 128]

$$\pi(\boldsymbol{f} \mid \boldsymbol{g}) \propto \exp\left(-\frac{1}{2}(\boldsymbol{f} - \boldsymbol{f}_{\mathrm{ML}})^T \tilde{\Gamma}^{-1} (\boldsymbol{f} - \boldsymbol{f}_{\mathrm{ML}})\right), \tag{2.20}$$

where the posterior covariance matrix is

$$\tilde{\Gamma} = [K^T \Gamma_v^{-1} K]^{-1}. \tag{2.21}$$

If the noise of the measurements is assumed to be independent and identically distributed, that is, the measurement noise covariance matrix is diagonal and of the form $\sigma_v^2 I \in \mathbb{R}^{m \times m}$, the maximum likelihood estimate can be written in the form

$$\boldsymbol{f}_{\mathrm{ML}} = [K^T K]^{-1} K^T \boldsymbol{g} := \boldsymbol{f}_{\mathrm{LS}} \tag{2.22}$$

which is a traditional *least square* (LS) estimate. In this case, the posterior covariance is of the form

$$\tilde{\Gamma} = [K^T K]^{-1}. \tag{2.23}$$

Sometimes the ML-estimate (2.19) is called generalized least square (GLS) estimate. Usefulness of the ML-estimate depends on the properties of the forward operator K. In the case of ill-posed inverse problem the ML-estimate is useless. This is because it corresponds to solving the inverse problem without regularization. If the forward model (2.3) is nonlinear, to obtain the maximum of the likelihood density, optimization methods have to be used. The optimization methods are discussed later in the case of MAP-estimate.

The MAP-estimate is the maximum of the posterior density, that is,

$$\boldsymbol{f}_{\text{MAP}} = \arg\max_{\boldsymbol{f}} \pi(\boldsymbol{f} \mid \boldsymbol{g}). \tag{2.24}$$

Also in this case, the maximization can be seen as the minimization of the exponent of the posterior density (2.14) and therefore the following minimization problem has to be solved

$$\min_{\boldsymbol{f}} S(\boldsymbol{f}), \tag{2.25}$$

where the functional $S(\boldsymbol{f})$ with the linear forward model is of the form

$$S(\boldsymbol{f}) = \Big((\boldsymbol{g} - K\boldsymbol{f})^T \Gamma_v^{-1} (\boldsymbol{g} - K\boldsymbol{f}) + (\boldsymbol{f} - \boldsymbol{f}^*)^T \Gamma_{\text{pr}}^{-1} (\boldsymbol{f} - \boldsymbol{f}^*)\Big). \tag{2.26}$$

The solution of the minimization problem can be written in the form [88]

$$\boldsymbol{f}_{\text{MAP}} = [K^T \Gamma_v^{-1} K + \Gamma_{\text{pr}}^{-1}]^{-1} [K^T \Gamma_v^{-1} \boldsymbol{g} + \Gamma_{\text{pr}}^{-1} \boldsymbol{f}^*]. \tag{2.27}$$

Also in this case the posterior density is Gaussian probability density (2.20) with the mean $\boldsymbol{f}_{\text{MAP}}$ and the covariance $\tilde{\Gamma}$

$$\tilde{\Gamma} = [K^T \Gamma_v^{-1} K + \Gamma_{\text{pr}}^{-1}]^{-1}. \tag{2.28}$$

By choosing $\Gamma_v = \sigma_v^2 I$, $\Gamma_{\text{pr}} = \sigma_{\text{pr}}^2 I$ and $\boldsymbol{f}^* = 0$, the equation (2.27) can be written in the form

$$\boldsymbol{f}_{\text{MAP}} = [K^T K + \alpha I]^{-1} K^T \boldsymbol{g} := \boldsymbol{f}_{\text{TIKH}}, \tag{2.29}$$

where $\alpha = \sigma_v^2 / \sigma_{\text{pr}}^2$. This is so called *standard Tikhonov regularization* [166]. The prior assumption of the parameters is now that they are independent and identically distributed. Tikhonov regularization is a widely used method in inverse problems. This kind of prior information is called *Gaussian white noise prior* [88].

If the forward model is nonlinear the minimization problem (2.25) with the functional

$$S(\boldsymbol{f}) = \Big((\boldsymbol{g} - K(\boldsymbol{f}))^T \Gamma_v^{-1} (\boldsymbol{g} - K(\boldsymbol{f})) + (\boldsymbol{f} - \boldsymbol{f}^*)^T \Gamma_{\text{pr}}^{-1} (\boldsymbol{f} - \boldsymbol{f}^*)\Big) \tag{2.30}$$

has to be solved. A natural choice for solving this nonlinear minimization problem is to use gradient-based optimization methods [133]. In the Newton type method the minimum point is find iteratively by using first order Taylor expansion of $K(\boldsymbol{f})$ around the point $\boldsymbol{f}_0$, that is,

$$K(\boldsymbol{f}) \approx K(\boldsymbol{f}_0) + \left(\frac{\partial K(\boldsymbol{f}_0)}{\partial \boldsymbol{f}}\right)(\boldsymbol{f} - \boldsymbol{f}_0), \tag{2.31}$$

where $\partial K(\boldsymbol{f}_0)/\partial \boldsymbol{f} = J$ is the Jacobian of the forward model with respect to $\boldsymbol{f}$ at the point $\boldsymbol{f}_0$. Inserting the expansion into the equation (2.30) and solving the resulting linear LS-problem, the iteration can be written in the form [128]

$$\boldsymbol{f}_{i+1} = \boldsymbol{f}_i + \kappa_i \left[J_i^T \Gamma_v^{-1} J_i + \Gamma_{\mathrm{pr}}^{-1}\right]^{-1} \left[J_i^T \Gamma_v^{-1}(\boldsymbol{g} - K(\boldsymbol{f}_i)) - \Gamma_{\mathrm{pr}}^{-1}(\boldsymbol{f}_i - \boldsymbol{f}^*)\right], \tag{2.32}$$

where κ_i is a step length parameter which controls the convergence of the iteration. The step length parameter can be obtained using a line search method. The nonlinear ML-estimate can be obtained from this equation by formally setting $\Gamma_{\mathrm{pr}}^{-1} \to \mathbf{0}$.

The estimates that are introduced so far can be solved using optimization methods. The calculation of the conditional mean (CM–estimate)

$$\boldsymbol{f}_{\mathrm{CM}} = E\{\boldsymbol{f} \mid \boldsymbol{g}\} = \int_{\mathcal{M}} \boldsymbol{f} \pi(\boldsymbol{f} \mid \boldsymbol{g}) \mathrm{d}\boldsymbol{f}, \tag{2.33}$$

is an integration problem. The number of parameters is usually large, thus the integral over a large dimensional space has to be computed. In that case common quadrature methods are not applicable. Consequently, the integration requires the use of alternative methods. One possible class of methods is sampling based methods and in that class specially the Markov chain Monte Carlo techniques (MCMC). The MCMC method is briefly introduced at the end of this chapter.

The commonly used spread estimator is *the Conditional covariance matrix* $\Gamma_{\boldsymbol{f}|\boldsymbol{g}} \in \mathbb{R}^{m \times m}$, that is

$$\begin{aligned}\Gamma_{\boldsymbol{f}|\boldsymbol{g}} &= E\{(\boldsymbol{f} - \boldsymbol{f}_{\mathrm{CM}})(\boldsymbol{f} - \boldsymbol{f}_{\mathrm{CM}})^T \mid \boldsymbol{g}\} \\ &= \int_{\mathcal{M}} (\boldsymbol{f} - \boldsymbol{f}_{\mathrm{CM}})(\boldsymbol{f} - \boldsymbol{f}_{\mathrm{CM}})^T \pi(\boldsymbol{f} \mid \boldsymbol{g}) \mathrm{d}\boldsymbol{f}. \end{aligned}\tag{2.34}$$

Computation of the conditional covariance is also an integration problem and also in this case the MCMC methods can be used. A corresponding *posterior correlation matrix* is a useful tool for analyzing the correlation between the parameters. This can be obtained from the conditional covariance matrix as follows

$$R_{\boldsymbol{f}|\boldsymbol{g}} = D^{-1} \Gamma_{\boldsymbol{f}|\boldsymbol{g}} D^{-1}, \tag{2.35}$$

where $D = (\mathrm{diag}(\Gamma_{\boldsymbol{f}|\boldsymbol{g}}))^{1/2}$ [108]. The posterior correlation matrix has the property $|R_{\boldsymbol{f}|\boldsymbol{g}}(i,j)| \le 1, \ \forall \ i,j$. This means that if there is no linear relationship between the i^{th} and j^{th} parameters the correlation $R_{\boldsymbol{f}|\boldsymbol{g}}(i,j)$ is zero. When the strength of the linear relationship between the parameters increases, so does the correlation. Moreover, when the linear relationship is perfect the correlation coefficient is 1.0. The positive correlation means that when one parameter has a high/low value, so does the other. The negative correlation means that when one parameter has a high/low value, the other has a low/high value.

For each parameter *a credibility interval* can also be computed, that is,

$$\int_{\alpha_k}^{\beta_k} \pi_k(f_k)\mathrm{d}f_k = \tau, \text{ such that } F(\alpha_k) = 1 - F(\beta_k), \tag{2.36}$$

where $0 < \tau < 1$ and $F(x)$ is a cumulative distribution function

$$F(\boldsymbol{f}) = \int_{-\infty}^{\boldsymbol{f}} \pi_k(f_k)\mathrm{d}f_k, \tag{2.37}$$

where π_k is the *marginal posterior density*

$$\pi_k(f_k) = \int_{\mathbb{R}^{n-1}} \pi(\boldsymbol{f} \mid \boldsymbol{g})\mathrm{d}f_1\mathrm{d}f_2 \dots \mathrm{d}f_{k-1}\mathrm{d}f_{k+1} \dots \mathrm{d}f_n. \tag{2.38}$$

To complete the discussion about the stationary estimation methods it should be emphasized here that all information on the parameters $\boldsymbol{f}$ is contained in the posterior density. This information can be characterized using the point and interval estimates. Moreover, the marginal posterior densities contain all possible information on each individual parameter. Interpretation of the results on the basis of the marginal posterior density only might give too optimistic result. The conditional covariance or correlation matrix therefore has to be computed and analyzed. For example, too strong correlation between two parameters means that the parameters can not be resolved independently [163]. This feature is obviously related to the resolution of the tomography method in question. This issue is studied in more detail in Chapter 5.

Markov chain Monte Carlo (MCMC) methods

In this section, the main ideas of the Markov chain Monte Carlo methods for evaluating integrals in high dimensional space are presented. Also an algorithm called the *Metropolis-Hastings algorithm* is introduced in quite informal level rather than strictly mathematically.

Typically, in estimation problems, the objective is to evaluate integral of the type

$$E\{f(\boldsymbol{x})\} = \int f(\boldsymbol{x})\pi(\boldsymbol{x})\mathrm{d}\boldsymbol{x}, \tag{2.39}$$

which is the mean of the function $f(\boldsymbol{x})$ provided that the integral exists. As discussed above traditional evaluation is usually impossible. However, if the samples $\{\boldsymbol{x}_1, \boldsymbol{x}_2, \dots, \boldsymbol{x}_N\} \sim \pi(\boldsymbol{x})$ can be drawn from the density $\pi(\boldsymbol{x})$, the integral can be estimated as follows

$$\int f(\boldsymbol{x})\pi(\boldsymbol{x})\mathrm{d}\boldsymbol{x} \approx \frac{1}{N}\sum_{\ell=1}^{N} f(x_\ell), \tag{2.40}$$

which is called *the ergodic mean.* This fact form the basis for the Monte Carlo integration procedures. Now the question is, if the shape of the density $\pi(\boldsymbol{x})$ is complicated, how sampling should be performed? According to the law of large numbers, the sample mean of the independent samples converge toward theoretical expectation as the number of the samples goes to infinity [138]. Sampling from the density $\pi(\boldsymbol{x})$ can be done using a *Markov chain.* It can be shown that if the Markov chain has *stationary distribution* $\pi(\boldsymbol{x})$ and it is *aperiodic* and *irreducible*, the equation (2.40) holds when $N \to \infty$ [88]. In Markov chain Monte Carlo methods the objective therefore is to construct a Markov chain whose stationary distribution is $\pi(\boldsymbol{x})$. This can be done for example by using the *Metropolis-Hastings algorithm* [132, 68]. Another widely used algorithm is the *Gibbs sampler* [56, 55]. These methods are relatively simple algorithms to generate samples for Monte Carlo integration. More detailed description and analysis of the Monte Carlo methods and above mentioned algorithms are presented in [88]. In the following, the Metropolis-Hastings algorithm is presented in algorithmic form

```
Choose initial value $x_1$, Set $x = x_1$
for $k = 2$ to $K$ do
  Draw $w \sim N(0, \sigma^2 I)$, set $y = x + w$
  Calculate acceptance ratio $\alpha(x, y) = \min(1, \pi(y)/\pi(x))$
  Draw u $\sim U([0, 1])$
  if $u < \alpha(x, y)$ then
    Accept: set $x = y, x_k = x$,
  else
    Reject: set $x_k = x$,
  end if
end for
```

There are two practical difficulties in MCMC simulations: after how many iterations the samples can be treated as samples obtained from the density $\pi(\boldsymbol{x})$ and what is the total length of the chain? First question is related to the choice of the starting point. Usually, first N_b iterations are neglected to ensure that the samples are from the density $\pi(\boldsymbol{x})$. The equation (2.40) therefore should be written in the form

$$\int f(\boldsymbol{x})\pi(\boldsymbol{x})\mathrm{d}\boldsymbol{x} \approx \frac{1}{N - N_b} \sum_{\ell=N_b+1}^{N} f(x_\ell). \tag{2.41}$$

The beginning of the chain is called *the burn-in period.* Second question is an important but a difficult issue. The number of the samples has to be sufficiently large to ensure that the samples cover the whole support of the density $\pi(\boldsymbol{x})$. In other words, it ensures that the equation (2.40) holds. Commonly these questions are related to the convergence of the MCMC method. An inportant issue is the correlation between different samples. If the correlation lenght of the chain is long the samples are not mutually indepedent which has a big influence on both burn-in period of the chain and the efficiency of the method. The independence of the consecutive samples can be studied using autocorrelation function of the chain. More details of the convergence issues can be found in [60].

CHAPTER III

Electrical impedance tomography (EIT)

3.1 Introduction

Let us consider first a simplified EIT experiment shown in Figure 3.1(a). The conductivity distribution within the domain $\Omega \in \mathbb{R}^2$ is denoted by $\sigma(\boldsymbol{x})$, where $\boldsymbol{x}$ is a point in $\mathbb{R}^2$. The objective in EIT is to estimate the conductivity distribution. This can be obtained with the aid of electrical measurements. In this case, the alternating current I is injected into the domain through the opposite pair of electrodes. The current causes scalar potential distribution $u(\boldsymbol{x}) \in \Omega$ which depends on the conductivity distribution $\sigma(\boldsymbol{x})$. The corresponding voltage differences between the adjacent pairs of electrodes are measured which are shown in Figure 3.1(b). The measured voltages are denote by $+$, connected together using solid line. A single set of measured voltages based on a single current injection does not carry enough information to solve the conductivity distribution. In order to estimate the conductivity distribution several independent sets of measurements are needed. The basic measurement strategy for EIT therefore is as follows. A current injection is applied to the domain through the electrodes and the corresponding voltages on the same electrodes are measured. Another independent current injection is applied, the voltages are again measured and the process is repeated until a complete set has been collected.

Estimation of the conductivity distribution is a nonlinear ill-posed inverse problem. In the Hadamard sense the ill-posedness means that: 1) the solution of the estimation problem is not necessarily unique and/or 2) the small errors in the data can lead to large changes in the estimated conductivity distribution [65]. Mathematicians have proven that the problem has unique solution in the case of continuous data, see e.g. [34, 101, 134]. In these studies different assumptions on the conductivity distribution and domain have been made. In the real life the continuous data can not be collected and also the conductivity distribution has to be considered as a discrete variable. In this case uniqueness depends on the number of the data and on the unknown parameters. In other words if the number of measured voltages is smaller than the number of the unknowns the solution is

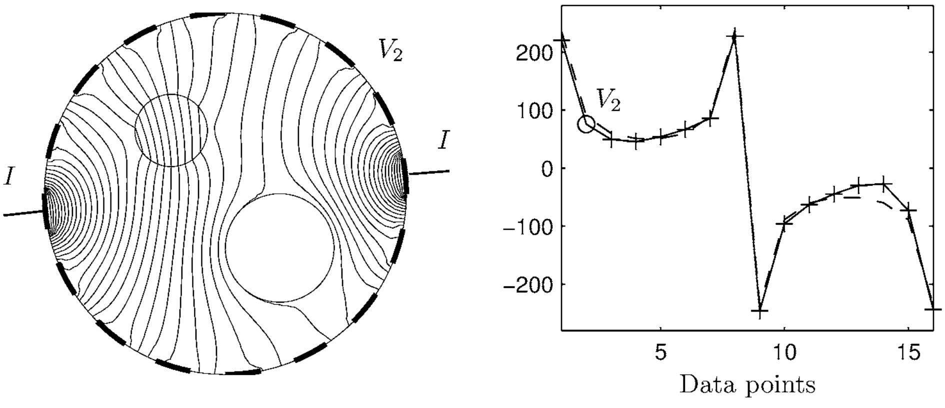

(a) EIT experiment (b) Measured voltages

Figure 3.1: A schematic presentation of an EIT experiment. (a) The conductivities of the bigger and smaller objects are 100 times bigger and 10 smaller than the background, respectively. The potential distribution is presented as contour lines. (b) The measured voltages corresponding to this current injection. The dashed line denotes the measured voltages from the tank without the objects. The voltage measurement V_2 between second and third electrodes is denoted by a circle. The unit of the voltage is arbitrary.

not unique. The second point can be seen from the Figure 3.1(b). By comparing the measurements collected from the tank with and without the objects, it can be calculated that the conductivity change of this case cause percentual changes in the measured voltages, which are between 4 % and 54 %, averagely about 14 %. In other words change in the data due to the big conductivity change is relatively small. Therefore even small errors in the data may cause large errors in the estimated conductivity distribution. As a summary it can be stated that in the case of EIT the Hadamard's second point is always valid and the validation of the first point depends on the formulation of the problem.

Several methods for the reconstruction problem of EIT have been developed. Popular qualitative methods are *backprojection algorithm* [20, 148, 131] and *sensitivity coefficient method* [106, 177] which is based on the theorem of Geselowitz [58]. These methods are out of scope of this thesis. In this section EIT is presented in the light of the framework introduced in Section 2.3.

In the beginning the forward and inverse problems of EIT are stated. Forward problem in EIT is as: *determine the voltages on the electrodes when the conductivity distribution of the target and the injected currents are known.* This means that the forward operator $K(\cdot)$ in equation (2.3) has to be derived. Statistical inverse problem in the case of EIT is as: *what information can be inferred on the* *value of the electrical conductivity based on the injected currents and corresponding measured voltages ?* For the solution of the inverse problem following models are needed: 1) the above mentioned forward model, 2) the prior model for the conductivity distribution and 3) the observation noise model. This chapter is dedicated to the introduction of these issues.

3.2 Forward modelling of EIT

Consider first the basic notations used in this section. Estimated quantity is conductivity distribution $\sigma(\boldsymbol{x})$ within the domain $\Omega \in \mathbb{R}^n$, $n = 2, 3$. This is discretized and it is approximated as

$$\sigma(\boldsymbol{x}) = \sum_{i=1}^{m} \sigma_i B_i(\boldsymbol{x}), \tag{3.1}$$

where $B_i(\boldsymbol{x})$ are either the basis functions of the finite element mesh or the characteristic functions of some subdomain Ω_i. Requirement for the subdomains is that $\cup_i \overline{\Omega}_i = \overline{\Omega}$, where $\overline{\Omega}$ is the closure of Ω. The conductivity distribution therefore is identified by a vector-valued random variable $\boldsymbol{\sigma} = (\sigma_1, \sigma_2, \ldots, \sigma_m)^T \in \mathcal{M}$. It is also assumed that the parameters belongs to the admissible set $\mathcal{A}(\Omega) = \{\sigma_i \mid 0 < c \leq \sigma_i \leq C \leq \infty, \sigma|_{\Omega_i} \in C(\overline{\Omega}_i)\}$, where c and C are some constants [87]. The measurements are the measured voltages on the electrodes with respect to some reference point. The data vector is also a vector-valued random variable $\boldsymbol{V} = (V_1, V_2, \ldots, V_n)^T \in \mathcal{D}$. The parameters and data vector have the joint density $\pi(\boldsymbol{\sigma}, \boldsymbol{V})$ in the joint space $\mathcal{M} \times \mathcal{D}$. The electric current injected through the electrode e_ℓ is denoted by I_ℓ and the vector $\boldsymbol{I} = (I_1, I_2, \ldots, I_L)^T \in \mathbb{R}^L$ is called *a current pattern.* The current pattern has to fulfill the condition $\sum_\ell I_\ell = 0$. In a traditional problem, the measurements consist of k experiments involving current patterns $\boldsymbol{I}_1, \boldsymbol{I}_2, \ldots, \boldsymbol{I}_k$ and the corresponding voltage measurements $\boldsymbol{V}_1, \boldsymbol{V}_2, \ldots, \boldsymbol{V}_k$. The total number of data points is therefore $L \times k$. This data set is called *a frame.*

3.2.1 Observation model

In the case of EIT the observation operator in equation (2.3) is a theoretical model between the conductivity distribution $\boldsymbol{\sigma}$ within the domain Ω, the injected currents and the voltages on the boundary electrodes. Formally this can be written in the form

$$\boldsymbol{U}(\boldsymbol{\sigma}) = U(\boldsymbol{\sigma}; I) = \mathcal{R}(\boldsymbol{\sigma})I, \tag{3.2}$$

where $U : \boldsymbol{\sigma} \mapsto \boldsymbol{U}$ is the nonlinear mapping between conductivity $\boldsymbol{\sigma} \in \mathcal{A}$ and the calculated voltages $\boldsymbol{U}$. Furthermore, the $\mathcal{R}(\cdot)$ is a so called *resistivity matrix.* These are discussed in more detail later in this section. Let us now discuss the behavior of the electromagnetic fields within the domain.

Electromagnetic fields within the bounded domain $\Omega \subset \mathbb{R}^3$ with a smooth boundary $\partial\Omega$ is governed by the macroscopic Maxwell equations [113]

$$
\begin{aligned}
\nabla \times \boldsymbol{E}(\boldsymbol{x},t) &= -\frac{\partial \boldsymbol{B}(\boldsymbol{x},t)}{\partial t} && (3.3)\\
\nabla \times \boldsymbol{H}(\boldsymbol{x},t) &= \boldsymbol{J}(\boldsymbol{x},t) + \frac{\partial \boldsymbol{D}(\boldsymbol{x},t)}{\partial t} && (3.4)\\
\nabla \cdot \boldsymbol{D}(\boldsymbol{x},t) &= \rho_c(\boldsymbol{x},t) && (3.5)\\
\nabla \cdot \boldsymbol{B}(\boldsymbol{x},t) &= 0, && (3.6)
\end{aligned}
$$

where $\boldsymbol{E}$ is the *electric field*, $\boldsymbol{D}$ is the *electric displacement*, $\boldsymbol{B}$ is the *magnetic induction*, $\boldsymbol{H}$ is the *magnetic field*, ρ_c is the *free charge density* and $\boldsymbol{J}$ is the *current density*. Moreover, $\boldsymbol{x}$ is a position vector in $\mathbb{R}^3$ and $t \in \mathbb{R}_+$ is time. Since the injected currents are usually time-harmonic, it is natural to represent the fields $\boldsymbol{E}$, $\boldsymbol{H}$, $\boldsymbol{J}$, $\boldsymbol{D}$ and $\boldsymbol{B}$ also as time-harmonic

$$
\begin{aligned}
\boldsymbol{E} &= \boldsymbol{E}(\boldsymbol{x})\exp(\mathtt{i}\omega t), \quad \boldsymbol{H} = \boldsymbol{H}(\boldsymbol{x})\exp(\mathtt{i}\omega t)\\
\boldsymbol{J} &= \boldsymbol{J}(\boldsymbol{x})\exp(\mathtt{i}\omega t), \quad \boldsymbol{D} = \boldsymbol{D}(\boldsymbol{x})\exp(\mathtt{i}\omega t),\\
\boldsymbol{B} &= \boldsymbol{B}(\boldsymbol{x})\exp(\mathtt{i}\omega t), && (3.7)
\end{aligned}
$$

where $\mathtt{i}$ is imaginary unit, ω is angular frequency. Further, assumption of linear isotropic medium leads to relations

$$
\begin{aligned}
\boldsymbol{D}(\boldsymbol{x}) &= \epsilon \boldsymbol{E}(\boldsymbol{x}) && (3.8)\\
\boldsymbol{B}(\boldsymbol{x}) &= \mu \boldsymbol{H}(\boldsymbol{x}) && (3.9)\\
\boldsymbol{J}(\boldsymbol{x}) &= \sigma \boldsymbol{E}(\boldsymbol{x}), && (3.10)
\end{aligned}
$$

where $\epsilon = \epsilon(\boldsymbol{x},\omega)$ is the *electric permittivity*, $\mu = \mu(\boldsymbol{x},\omega)$ is the *magnetic permeability* and $\sigma = \sigma(\boldsymbol{x},\omega)$ is the *electric conductivity*. In anisotropic media these quantities have to be replaced with the corresponding tensors. The anisotropic EIT problem is studied e.g. in [109, 160, 29, 63]. Using the relations (3.8 – 3.10), the equations (3.3) and (3.4) can be written in time-harmonic form

$$
\begin{aligned}
\nabla \times \boldsymbol{E}(\boldsymbol{x}) &= -\mathtt{i}\omega\mu \boldsymbol{H}(\boldsymbol{x}) && (3.11)\\
\nabla \times \boldsymbol{H}(\boldsymbol{x}) &= \boldsymbol{J}(\boldsymbol{x}) + \mathtt{i}\omega\epsilon \boldsymbol{E}(\boldsymbol{x}). && (3.12)
\end{aligned}
$$

The current density $\boldsymbol{J}(\boldsymbol{x})$ can be written in the form $\boldsymbol{J}(\boldsymbol{x}) = \boldsymbol{J}_{\mathrm{ohm}}(\boldsymbol{x}) + \boldsymbol{J}_{\mathrm{s}}(\boldsymbol{x})$, where $\boldsymbol{J}_{\mathrm{ohm}}(\boldsymbol{x}) = \sigma \boldsymbol{E}(\boldsymbol{x})$ is the *ohmic current* and $\boldsymbol{J}_{\mathrm{s}}(\boldsymbol{x})$ is the *current source*. Taking this into account, the equations (3.11 – 3.12) can be written in the form

$$
\begin{aligned}
\nabla \times \boldsymbol{E}(\boldsymbol{x}) &= -\mathtt{i}\omega\mu \boldsymbol{H}(\boldsymbol{x}) && (3.13)\\
\nabla \times \boldsymbol{H}(\boldsymbol{x}) &= (\sigma + \mathtt{i}\omega\epsilon)\boldsymbol{E}(\boldsymbol{x}) + \boldsymbol{J}_{\mathrm{s}}(\boldsymbol{x}). && (3.14)
\end{aligned}
$$

These two equations are *time-harmonic Maxwell equations*. Note that in this case the frequency ω is fixed. In the frequency range used in EIT the term $\omega\mu$ is small and therefore the term $-\mathtt{i}\omega\mu \boldsymbol{H}(\boldsymbol{x})$ is negligible. Because of this assumption, the equation (3.13) can be approximated as

$$\nabla \times \boldsymbol{E}(\boldsymbol{x}) = 0. \tag{3.15}$$

It can be shown that when the curl of the vector $\boldsymbol{E}(\boldsymbol{x})$ is zero, there exists a gradient of the scalar potential ∇u [12], such that

$$\boldsymbol{E}(\boldsymbol{x}) = -\nabla u(\boldsymbol{x}), \tag{3.16}$$

where $u(\boldsymbol{x})$ is called *electric scalar potential.* Taking the divergence on both sides of equation (3.14) and inserting (3.16) into (3.14) the following equation inside the domain Ω is obtained

$$\nabla \cdot \gamma \nabla u(\boldsymbol{x}) = 0, \tag{3.17}$$

where $\gamma = (\sigma + \mathrm{i}\omega\epsilon)$ is the *admittivity* of the medium. This approximation of the field equation is known as the *quasi-static approximation.* In previous derivations the facts that $\nabla \cdot \nabla \times \boldsymbol{H}(\boldsymbol{x}) = 0$ [12] and $\boldsymbol{J}_\mathrm{s}(\boldsymbol{x}) = 0$ were used, since there are no current sources within the domain Ω. In Chapter 4 a situation in which there is current sources within the domain will be discussed. Time-harmonic EIT was studied in [137] in which quasi-static approximation was not assumed. It is also possible to write the equation (3.17) with the inverse of the admittivity, which is called *impedivity* ζ, that is,

$$\frac{1}{\gamma} = \zeta = \frac{\sigma}{\sigma^2 + (\omega\epsilon)^2} - \mathrm{i}\frac{\omega\epsilon}{\sigma^2 + (\omega\epsilon)^2}. \tag{3.18}$$

In this case, the equation (3.17) is of the form

$$\nabla \cdot \zeta^{-1} \nabla u(\boldsymbol{x}) = 0. \tag{3.19}$$

If the capacitance effects are also negligible ($\epsilon \approx 0$), the admittivity and the impedivity can be approximated by the real-valued quantities σ and $1/\sigma = \rho$, where ρ is the *resistivity.* In these cases, the equations (3.17) and (3.19) can be written in the form

$$\begin{aligned} \nabla \cdot \sigma \nabla u(\boldsymbol{x}) &= 0 && (3.20)\\ \nabla \cdot \rho^{-1} \nabla u(\boldsymbol{x}) &= 0. && (3.21) \end{aligned}$$

In this thesis, either the equation (3.20) or (3.21) is used. The EIT with the admittivity distribution, see [51, 170].

In order to obtain a forward model for EIT, the boundary conditions have to be determined. The boundary conditions arise from the current injection and voltage measurements through the boundary electrodes. Several different boundary conditions for EIT have been developed. Commonly these boundary conditions are called *electrode models.* In this thesis, the so called *complete electrode model* (CEM) is used [39, 159]. Other possible models are *continuum*, *gap* and *shunt models.* The details of these other models can be found e.g. in [39, 159, 37].

BOUNDARY CONDITIONS

In general, the normal component of the current density on the boundary $\partial\Omega$ is

$$\sigma \frac{\partial u(\boldsymbol{x})}{\partial \nu} = j_\nu(\boldsymbol{x}), \quad \boldsymbol{x} \in \partial\Omega, \tag{3.22}$$

where ν is the outward unit normal. Mathematically, this is a Neumann boundary condition. Let $e_\ell, \ell = 1, \dots, L$ be a surface of the boundary $\partial\Omega$ under the electrode ℓ, where L is the number of the electrodes. In the real case, the current density under the electrodes is not known. Instead of that, the total amount of injected current I_ℓ on each electrode is known. Therefore, the boundary condition for the current injection electrodes can be written in the form

$$\int_{e_\ell} \sigma \frac{\partial u(\boldsymbol{x})}{\partial \nu} \mathrm{d}S = I_\ell, \quad 1 \le \ell \le L. \tag{3.23}$$

In other words, the total amount of current I_ℓ flowing to or from the electrode e_ℓ is the integral of the normal component of the boundary current density over the electrode surface. The value of the current I_ℓ is a root-mean-square (RMS) value of the injected sinusoidal current. Mathematically this boundary condition is the global boundary condition instead of the Neumann condition. The boundary $\partial\Omega \setminus \cup e_\ell$ between the electrodes is insulating and therefore the current density through this boundary is zero, and thus

$$\sigma \frac{\partial u(\boldsymbol{x})}{\partial \nu} = 0, \quad \boldsymbol{x} \in \partial\Omega \setminus \cup_{\ell=1}^{L} e_\ell. \tag{3.24}$$

The value of the measured voltages U_ℓ on the ℓ'th electrode is the sum of the electric potential $u(\boldsymbol{x})$ on the boundary under the electrode and the potential drop due to the contact impedance layer between the electrode and the medium,

$$u(\boldsymbol{x}) + z_\ell \sigma \frac{\partial u(\boldsymbol{x})}{\partial \nu} = U_\ell, \quad 1 \le \ell \le L, \tag{3.25}$$

where z_ℓ is the effective contact impedance. Note that here it is required that U_ℓ is constant on the electrode. The requirement is the consequence of shunting effect of the high conductive metal electrodes on the boundary $\partial\Omega$.

In addition, the following two conditions for the injected currents and measured voltages are needed to ensure the existence and uniqueness of the solution

$$\sum_{\ell=1}^{L} I_\ell = 0 \tag{3.26}$$

$$\sum_{\ell=1}^{L} U_\ell = 0\,. \tag{3.27}$$

Solution of the complete electrode model is the electric potential distribution within the domain Ω and the voltages U_ℓ on the electrodes. Due to the complicated boundary condition, analytical solution of the CEM is possible only for simple cases such as in circular geometry with homogeneous conductivity distribution. However, in real situations the geometry of the object is more complicated and the conductivity distribution is not homogeneous and therefore numerical methods have to be used.

FINITE ELEMENT SOLUTION OF THE COMPLETE ELECTRODE MODEL

The weak formulation of the complete electrode model was originally suggested in [159] and was recently reviewed in [171]. In these references it is shown that $(u, U) \in H^1(\Omega) \otimes \mathbb{R}^L = H$ is the weak solution of the complete electrode model such that

$$\mathcal{B}((u,U),(v,V)) = \sum_{\ell=1}^{L} I_\ell V_\ell, \quad \forall \ \ (v,V) \in H, \tag{3.28}$$

where $\mathcal{B}$ is the bilinear form $\mathcal{B} : H \times H \to \mathbb{R}$

$$\mathcal{B}((u,U),(v,V)) = \int_\Omega \sigma \nabla u \cdot \nabla v \mathrm{d}x + \sum_{\ell=1}^{L} \frac{1}{z_\ell} \int_\ell (u - U_\ell)(v - V_\ell) \mathrm{d}S. \tag{3.29}$$

The variational form (3.28) is infinite dimensional which is not appropriate in that form for numerical calculations. Therefore finite element method (FEM) is used to turn the variational equation into a finite dimensional approximation. First step in the FEM formulation is to discretize the domain Ω into a mesh of small elements. These elements could be for example either squares or triangles in 2D or either cubics or tetrahedra in 3D. In this thesis, triangular elements in 2D and tetrahedral elements in 3D are used.

The potential distribution $u(\boldsymbol{x})$ is approximated within the domain Ω by the finite sum

$$u^h(\boldsymbol{x}) = \sum_{i=1}^{N} \alpha_i \varphi_i(\boldsymbol{x}), \tag{3.30}$$

where the functions $\varphi_i(x)$ are nodal basis functions of the finite element mesh and N is the number of the nodes in the finite element mesh. Normally these functions are either the 1^{st} or 2^{nd} order polynomial functions. In this thesis, mainly 1^{st} order polynomial, i.e., piece-wise linear basis functions are used. The approximation u^h belongs to the finite dimensional subspace H^h of $H^1(\Omega)$. The subspace is $H^h = \mathrm{span}\{\varphi_i | 1 \leq i \leq N\}$. Correspondingly, the voltages U on the electrodes are approximated as

$$U^h = \sum_{j=1}^{L-1} \beta_j n_j, \tag{3.31}$$

where the basis functions $n_j \in \mathbb{R}^L$ are chosen as $n_1 = [1, -1, 0, \ldots, 0]^T, n_2 = [1, 0, -1, \ldots, 0]^T, \ldots, n_{L-1} = [1, 0, \ldots, -1]^T$.

Using the theory of finite elements [31], a substitution of the approximating functions (3.30) and (3.31) into the variational equation (3.28) and choose $v = \varphi_j, V = n_k$ leads to a matrix equation

$$A\boldsymbol{\theta} = \boldsymbol{f}, \tag{3.32}$$

where $\boldsymbol{\theta} = [\boldsymbol{\alpha}, \boldsymbol{\beta}]^T \in \mathbb{R}^{N+L-1}$ is the solution vector and $\boldsymbol{f}$ is the data vector, that is,

$$\boldsymbol{f} = \left[\begin{array}{c} \mathbf{0} \\ \sum_{\ell=1}^{L} I_\ell (n_j)_\ell \end{array} \right] = \left[\begin{array}{c} \mathbf{0} \\ \mathcal{C}^T I \end{array} \right]. \tag{3.33}$$

Moreover, the matrix $A \in \mathbb{R}^{(N+L-1)\times(N+L-1)}$ is the sparse block matrix given by

$$\begin{aligned} A(\boldsymbol{\sigma}, \boldsymbol{z}) &= \left[\begin{array}{cc} \mathcal{B}((\varphi_i, 0), (\varphi_k, 0)) & \mathcal{B}((0, n_i), (\varphi_k, 0)) \\ \mathcal{B}((\varphi_i, 0), (0, n_k)) & \mathcal{B}((0, n_i), (0, n_k)) \end{array} \right] \\ &= \left[\begin{array}{cc} B(\boldsymbol{\sigma}) + C(\boldsymbol{z}) & D(\boldsymbol{z})\mathcal{C} \\ (D(\boldsymbol{z})\mathcal{C})^T & \mathcal{C}^T E(\boldsymbol{z})\mathcal{C} \end{array} \right], \end{aligned} \tag{3.34}$$

where the blocks are as

$$B_{i,j}(\boldsymbol{\sigma}) = \int_\Omega \sigma \nabla\varphi_i \cdot \nabla\varphi_j \,\mathrm{d}x\,\mathrm{d}y \quad 1 \le i, j \le N \tag{3.35}$$

$$C_{i,j}(\boldsymbol{z}) = \sum_{\ell=1}^{L} \frac{1}{z_\ell} \int_{e_\ell} \varphi_i \varphi_j \,\mathrm{d}S \quad 1 \le i, j \le N \tag{3.36}$$

$$D_{i,j}(\boldsymbol{z}) = -\frac{1}{z_j} \int_{e_j} \varphi_i \,\mathrm{d}S \quad 1 \le i \le N, \;\; 1 \le j \le L \tag{3.37}$$

$$\begin{aligned} E_{i,j}(\boldsymbol{z}) &= \sum_{\ell=1}^{L} \frac{1}{z_\ell} \int_{e_\ell} (n_i)_\ell (n_j)_\ell \,\mathrm{d}S \\ &= \left\{ \begin{array}{ll} 0\,, & i \ne j \\ \frac{|e_j|}{z_j} & i = j \end{array} \right. \quad 1 \le i, j \le L \end{aligned} \tag{3.38}$$

where $|e_j|$ is the measure (area) of the electrode j. The matrix $\mathcal{C} \in \mathbb{R}^{L\times(L-1)}$ in the equations (3.33) and (3.34) is a sparse matrix having n_j's as columns such that

$$\mathcal{C} = \left[\begin{array}{cccc} 1 & 1 & \cdots & 1 \\ -1 & 0 & \cdots & 0 \\ 0 & -1 & & 0 \\ \vdots & & \ddots & \vdots \\ 0 & 0 & \cdots & -1 \end{array} \right]. \tag{3.39}$$

The potentials $U_\ell^h, \ell = 1, \ldots, L$ on the electrodes are obtained according to equation (3.31) as

$$\begin{aligned} U_1^h &= \sum_{\ell=1}^{L-1} \beta_\ell \\ U_2^h &= -\beta_1 \\ U_3^h &= -\beta_2 \\ &\vdots \\ U_L^h &= -\beta_{L-1}, \end{aligned} \tag{3.40}$$

which can be written in the matrix form as

$$U^h = \mathcal{C}\beta, \tag{3.41}$$

where $U^h = [U_1^h, U_2^h, \ldots, U_L^h]^T$ and $\beta = [\beta_1, \beta_2, \ldots, \beta_{L-1}]^T$. Now, the relation between the injected currents and the computed voltages on the electrodes can be written in the form

$$U^h = \mathcal{C}\beta = \mathcal{C}\widetilde{\mathcal{R}}^h(\sigma, z)\mathcal{C}^T I = \mathcal{R}^h(\sigma, z)I, \tag{3.42}$$

where $\widetilde{\mathcal{R}}^h(\sigma, z) \in \mathbb{R}^{(L-1)\times(L-1)}$ is a block matrix $(A^{-1})_{i,j}, N+1 \le i, j \le N+L-1$ of the inverse of the matrix A. The matrix $\mathcal{R}^h(\sigma, z)$ is called the *resistivity matrix*. The equation (3.42) can be seen as a *generalized Ohm's law*; the relation between the voltages on the electrodes and the injected currents is linear. It can also be seen that the relation between the conductivity distribution, contact impedances and the voltages is nonlinear. This implies that the estimation of the conductivity distribution and contact impedances, when the injected currents and the voltages on the electrodes are given, is a nonlinear estimation problem.

In the real case, the actual measurements are performed with respect to some reference electrode. The actual measurements therefore are obtained by multiplying U^h from the left with a measurement matrix $M \in \mathbb{R}^{Q\times L}$, where Q is the number of the actual measurements of the single current pattern. Thus, the actual measurements are obtained by

$$U^h_{\text{actual}} = MU^h = M\tilde{\mathcal{C}}\theta = \tilde{M}\theta, \tag{3.43}$$

where $\tilde{\mathcal{C}} = (\mathbf{0}, \mathcal{C})^T$ and $\tilde{M} = M\tilde{\mathcal{C}}$.

FORWARD PROBLEM SIMULATIONS

In this section some forward problem simulations are presented. All simulations are performed in three-dimensional domain. Forward problem simulations have been presented earlier e.g. in [146, 28]. In [146] three-dimensional potential distributions in different domains were shown. In [28] boundary potential distributions and boundary current densities in two-dimensional case were studied. Here three-dimensional potential distribution, boundary potential distribution and boundary current density in the case of a cylindrical tank are studied. A special attention is paid to the effect of the electrode contact impedance z_ℓ. The effects to the boundary current density and to the boundary potential are studied.

80 electrodes on five different layers were attached on the boundary of the tank. Two of these electrode layers are shown in Figure 3.2(a). The number of the nodes and elements in the finite element mesh were 1358 and 6240, respectively. The tetrahedral elements were used. The conductivity and potential distributions were represented in piecewise linear basis. The homogeneous conductivity distribution was used the conductivity value being one (arbitrary unit). The current was injected between an opposite pair of electrodes on the first and fifth electrode layers. For details on the current injections, see Section 3.4.

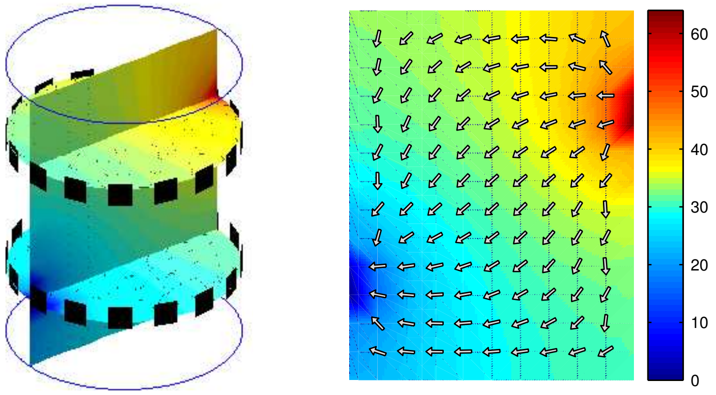

(a) (b)

Figure 3.2: Three-dimensional potential distribution u^h for modified opposite current injection. (a) Three slices of potential distribution. Two electrode layers and upper and lower edges of the tank are also shown. (b) vertical slice from (a) and current density projected to this plane. The lengths of the vectors are scaled the same. (a) and (b) are in the same color scale.

Let us consider first the potential distribution $u^h(\boldsymbol{x})$. The potential distribution is shown in Figure 3.2(a). One vertical and two horizontal layers are shown. The value of the potential is represented by color. It can be seen that the highest and lowest values of the potential distribution are near the current carrying electrodes as it should be. The current density projected to the vertical plane in Figure 3.2(a) is shown in Figure 3.2(b). The current density is calculated from the potential distribution as $\boldsymbol{j}|_{y=0} = \sigma \nabla u|_{y=0}$. The lengths of the current density vectors are scaled the same, hence qualitative inspection is only possible. Current seems to flow from the upper electrode to the lower electrode as it intuitively should do. The presence of the passive electrodes can be seen in both vertical edges of the plane as the varying variation of the direction of the current density vectors. The presentations do not show the details of the potential distribution and current density specially near the electrodes. Hence, to get a more closer view on the behavior of the potential distribution and the current density, these quantities are computed in the proximity of the electrodes.

Let us consider one of the active electrodes. The potential distributions under the active electrode with different value of contact impedance are shown in Figure 3.3. Values of the contact impedance were 1, 0.1, 0.01 and 0.001. The effect of the electrodes to the potential distribution can be clearly seen. If the contact impedance is large, the potential distribution under the electrode is smooth whereas if the contact impedance is small, it is nearly constant. The boundary

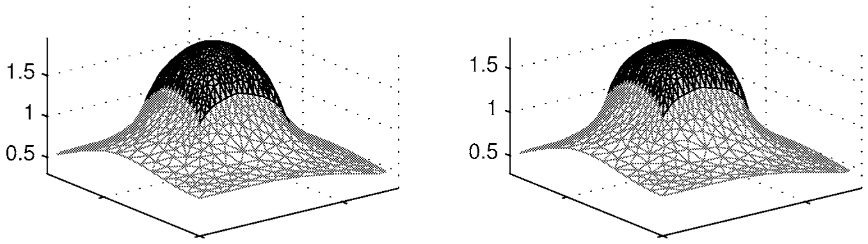

(a) $z = 1$ (b) $z = 0.1$

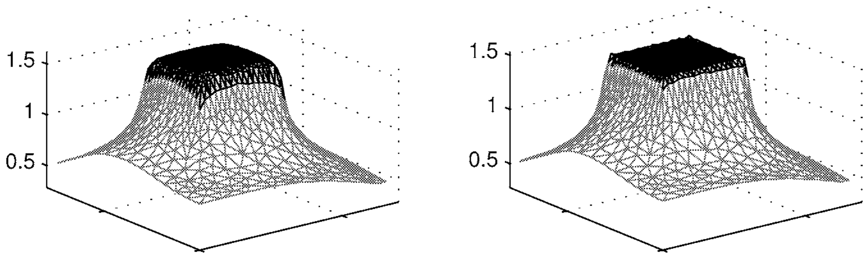

(c) $z = 0.01$ (d) $z = 0.001$

Figure 3.3: Electrical potential distribution u under active electrode with different electrode contact impedance z. The dark area denote the place of the electrode.

current densities for the same cases are shown in Figure 3.4. The boundary current density $j = \sigma \partial u / \partial \nu$ can be computed from the equation (3.25) and it is of the form $j_\ell(\boldsymbol{x})|_{\boldsymbol{x} \in \partial\Omega} = (U_\ell - u(\boldsymbol{x}))/z_\ell$. Moreover, according to equation (3.24) it is zero between the electrodes. When the contact impedance is large, the boundary current density is nearly uniform under the electrode. Moreover, the value is around 10 (arbitrary unit), see Figure 3.4(a). When the contact impedance becomes smaller, the value of the current density becomes larger specially near the corners of the electrode. Finally, in the case of smallest contact impedance the current density is around 150 on the corners of the electrode, see Figure 3.4(d). This means that the local current density in these areas is high. It has been shown earlier that near the edge of the electrode the current density has a singular behavior [141]. According to equation (3.23), the integral of the current density over the electrode is constant and it has a value I_ℓ, which was 1 in this case. This means that the current flows to the domain through this electrode whereas the current flows out

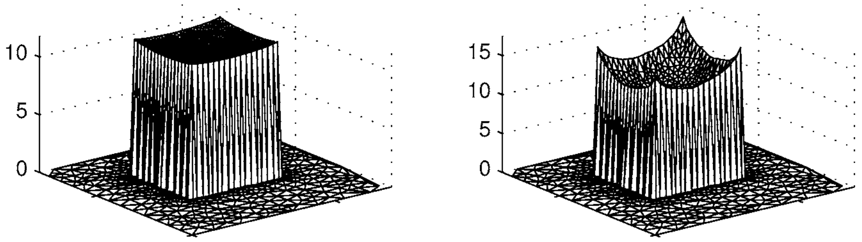

(a) $z = 1$

(b) $z = 0.1$

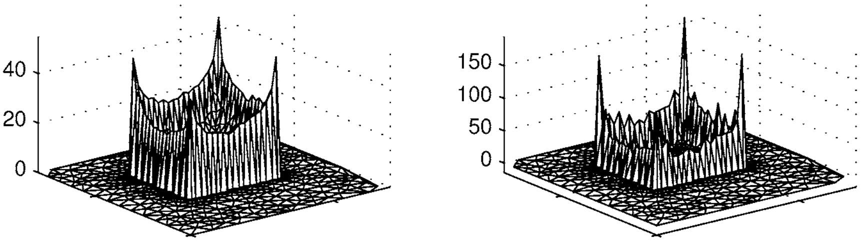

(c) $z = 0.01$

(d) $z = 0.001$

Figure 3.4: The boundary current density j under active electrode with different electrode contact impedance z.

from the domain when the value is -1.

The potential distributions under the passive electrode with varying contact impedance are shown in Figure 3.5. The contact impedance values were the same as in the active electrode case. When the contact impedance is large, the effect of the electrode to the potential distribution is not remarkable, see Figure 3.5(a) When contact impedance becomes smaller, the presence of the electrode starts to affect the potential distribution. In the case of the smallest contact impedance, the potential distribution is nearly constant under the electrode. The result is intuitively clear, if the low resistive layer is between the domain and the electrode the current that flows inside the domain can flow to the electrode and after that return back to the domain easily. This current is called *a shunting current* and this effect is called *a shunting effect* which is seen more clearly in the case of the current density. The potential distribution on the areas surrounding the electrode is slanted because it is not constant on the boundary of the domain as can be seen

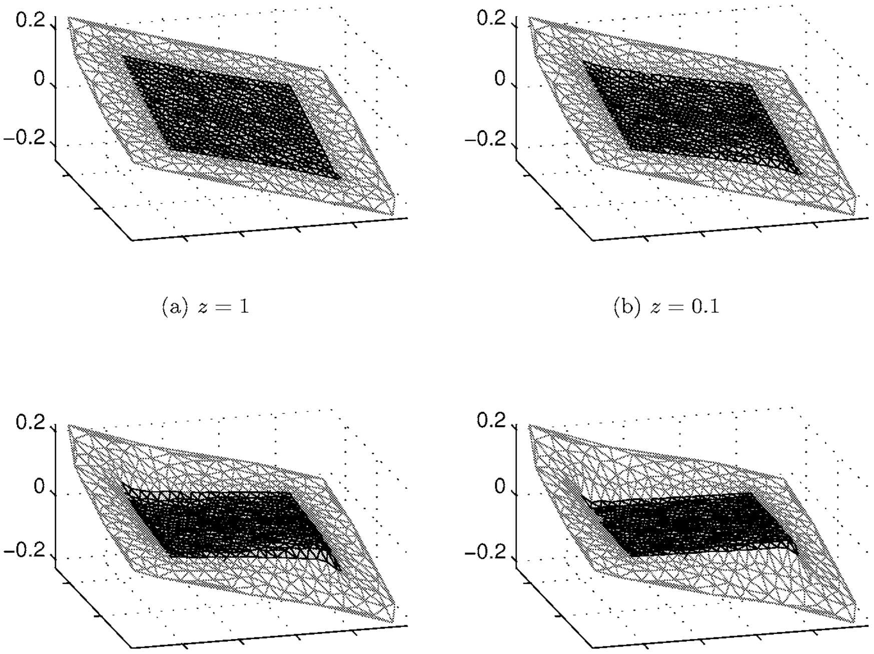

(a) $z = 1$ (b) $z = 0.1$

(c) $z = 0.01$ (d) $z = 0.001$

Figure 3.5: Electrical potential distribution u under passive electrode with different electrode contact impedance z. The dark area denote the place of the electrode.

from Figure 3.2. The current densities for the passive electrode are shown Figure 3.6. It can be seen that current is entering the electrode in one corner and leaving it in another corner and hence the net flux is zero. In other words, the integral of the current density over the electrode is zero. Also in this case the local current density is bigger with the small contact impedance and it is concentrated to the corners of the electrode.

There is also an interesting issue related to the contact impedance. If the test functions in the variational form (3.28) are chosen as $v = u$ and $V = U$, the variational form can be written in the form

$$\underbrace{\sum_{\ell=1}^{L} I_\ell U_\ell}_{P_{\mathrm{Total}}} = \underbrace{\int_\Omega \sigma |\nabla u|^2 \mathrm{d}x}_{P_{\mathrm{Domain}}} + \underbrace{\sum_{\ell=1}^{L} \int_{e_\ell} z_\ell \left(\sigma \frac{\partial u}{\partial \nu} \right)^2 \mathrm{d}S}_{P_z} . \tag{3.44}$$

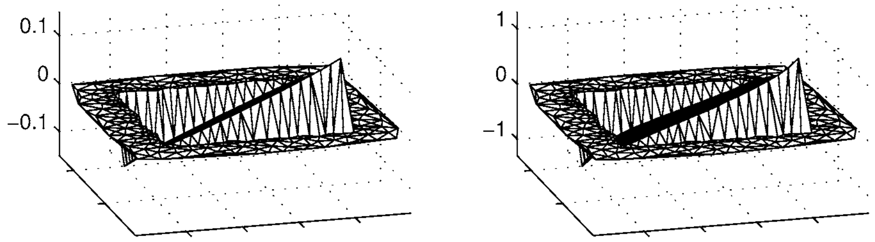

(a) $z = 1$ (b) $z = 0.1$

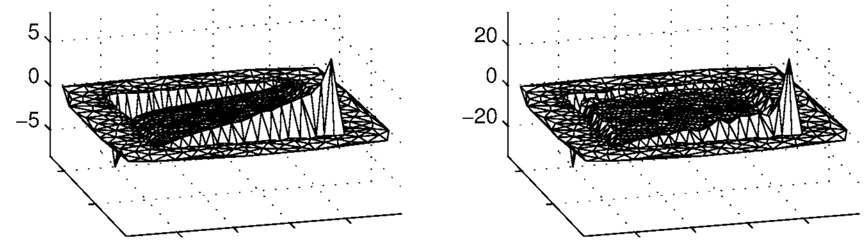

(c) $z = 0.01$ (d) $z = 0.001$

Figure 3.6: Boundary current density j_ν under passive electrode with varying electrode contact impedance z.

This has a clear physical interpretation. The power input P_{Total} is dissipated either in the domain Ω or in the contact impedance layer under the electrodes [145, 146, 111]. The dissipated powers in impedance layer under all the electrodes with different contact impedance are calculated and tabulated in Table 3.1. It can be seen that there is a huge difference in the percentage fractions of power that is dissipated in the contact impedance with different value of the contact impedance. The knowledge of the value of the contact impedance is therefore important. The estimation of the contact impedances is presented in Chapter 4.

3.3 Stastistical inversion in EIT

3.3.1 Likelihood density

Likelihood density is based on the observation model (2.3) and it is of the form

$$\boldsymbol{V} = \boldsymbol{U}(\boldsymbol{\sigma}) + \boldsymbol{v}, \tag{3.45}$$

Table 3.1: Dissipated power in contact impedance layer under the electrodes. P_{tot} is the total input power. $P_{z,\text{all}}$ is the dissipated power in impedance layer under all the electrodes. P_z is the percentage dissipated power in impedance layer.

z (Ωm^2)	P_{tot} (W)	$P_{z,\text{all}}$ (W)	P_z (%)
1	$2.5585 \cdot 10^{-5}$	$2.4637 \cdot 10^{-5}$	96.29
0.1	$5.5260 \cdot 10^{-6}$	$2.6558 \cdot 10^{-6}$	48.06
0.01	$3.3632 \cdot 10^{-6}$	$4.8373 \cdot 10^{-7}$	14.38
0.001	$3.0348 \cdot 10^{-6}$	$1.9351 \cdot 10^{-7}$	6.38

where $\boldsymbol{V}$ is the measured voltages, $\boldsymbol{U}(\boldsymbol{\sigma})$ is the computed voltages using the model (3.2) and $\boldsymbol{v}$ is the measurement noise with the covariance matrix Γ_v. Assuming that the noise is distributed as $\boldsymbol{v} \sim N(0, \Gamma_v)$ and using equation (2.9), the likelihood density can be written in the form

$$\pi(\boldsymbol{V} \mid \boldsymbol{\sigma}) = \frac{(\det \Gamma_v)^{-1/2}}{(2\pi)^{n/2}} \exp\Big(-\frac{1}{2}(\boldsymbol{V} - \boldsymbol{U}(\boldsymbol{\sigma}))^T \Gamma_v^{-1} (\boldsymbol{V} - \boldsymbol{U}(\boldsymbol{\sigma}))\Big). \tag{3.46}$$

The Gaussian assumption of the noise in real application will be confirmed in practice in Section 7.4.

3.3.2 Priors for EIT

As discussed in Chapter 2, the prior information is the probability density of the parameters in the model space $\mathcal{M}$ before the measurement. A fundamental piece of prior information in EIT is a positivity constraint of the conductivity distribution. This requirement is included in definition of set $\mathcal{A}$[‡]. Formally this can be defined as

$$\pi_+(\boldsymbol{\sigma}) = \prod_{i=1}^{m} \theta(\sigma_i), \tag{3.47}$$

where θ is the Heaviside function. Note that the density $\pi_+(\boldsymbol{\sigma})$ is not a probability density function since its integral is infinite. In practice, the positivity constraint is taken into account in another way. Possible deterministic methods are *an interior point method* [104] and *a projection method* [176].

As presented in Section 2.3, the Gaussian prior density is of the form

$$\pi(\boldsymbol{\sigma}) \propto \exp\left(-\frac{1}{2}(\boldsymbol{\sigma} - \boldsymbol{\sigma}^*)^T \Gamma_{\text{pr}}^{-1} (\boldsymbol{\sigma} - \boldsymbol{\sigma}^*)\right). \tag{3.48}$$

By changing the covariance matrix Γ_{pr}, different prior models are obtained. Simplest choice is identity matrix, i.e., $\Gamma_{\text{pr}} = I$. The choice $\boldsymbol{\sigma}^* = 0$ leads to

---

[‡] The definition of set $\mathcal{A}$, see page 33.

the standard Tikhonov regularization which has earlier been applied in EIT, see [30, 78, 139]. It is also possible to use scaled diagonal matrix, i.e. $\Gamma_{\text{pr}} = \text{diag}(\sigma_1^2, \sigma_2^2, \ldots, \sigma_m^2)$, where σ_i^2 are the a priori known variances of the parameters, see e.g. [38]. A common feature of these prior models is that there is no correlation between the parameters.

The most commonly used prior model in EIT is smoothness prior [77, 78, 11, 142]. In this case the covariance matrix is of the form $\Gamma_{\text{pr}} = L^T L$, where L can be thought of as a discrete approximation of some differential operator. In some cases the smoothness of the conductivity distribution might be different in different directions. For example, it can be assumed that the conductivity distribution in the stirrer tank is rotationally symmetric, being smooth with respect to the angular variable and non-smooth with respect to the radial variable. This assumption leads to the class of *anisotropic smoothness priors* [89]. Also non-Gaussian priors have been applied in EIT. Examples of the non-Gaussian prior are total-variation and L^1-priors. These prior models are out of the scope of this thesis, see details in [47, 87, 124, 203].

Discuss next the formulation of the anisotropic smoothness prior for the piecewise linear approximation of the conductivity distribution in three dimensional domain. Approach is closely related to the approach proposed in [89]. The conductivity distribution is parametrized as follows

$$\boldsymbol{\sigma}(\boldsymbol{x}) = \sum_{i=1}^{N} \sigma_i \varphi_i(\boldsymbol{x}), \tag{3.49}$$

where $\boldsymbol{x} = (x, y, z) \in \mathbb{R}^3$ and $\varphi_i(\boldsymbol{x})$ is a linear basis function of the i^{th} node. Consider the regularizing functional

$$W(\boldsymbol{\sigma}) = \int_\Omega \|A(\boldsymbol{x})\nabla(\boldsymbol{\sigma}(\boldsymbol{x}) - \boldsymbol{\sigma}^*(\boldsymbol{x}))\|^2 \mathrm{d}\boldsymbol{x}, \tag{3.50}$$

where $A(\boldsymbol{x})$ is matrix-valued mapping on Ω. The functional W measures the square integral norm of the directional gradient of $\boldsymbol{\sigma} - \boldsymbol{\sigma}^*$ in the direction determined by the matrix-valued field $A(\boldsymbol{x})$.

By the eigenvalue decomposition of $A(\boldsymbol{x})$ the functional (3.50) can be written in the form [1]

$$\begin{aligned} W(\boldsymbol{\sigma}) &= \sum_{j=1}^{3} \int_\Omega \left|\lambda_j(\boldsymbol{x}_k) v_j^T(\boldsymbol{x}_k) \nabla(\boldsymbol{\sigma}(\boldsymbol{x}) - \boldsymbol{\sigma}^*(\boldsymbol{x}))\right|^2 \mathrm{d}\boldsymbol{x} \\ &= \sum_{j=1}^{3} \sum_{k=1}^{M} |\Omega_k| \left|\lambda_j(\boldsymbol{x}_k) v_j^T(\boldsymbol{x}_k) \nabla(\boldsymbol{\sigma}(\boldsymbol{x}_k) - \boldsymbol{\sigma}^*(\boldsymbol{x}_k))\right|^2, \end{aligned} \tag{3.51}$$

where M is the number of the elements and $|\Omega_k|$ is the volume of the k^{th} element. Now the question is how to choose the eigenvectors $v_j(\boldsymbol{x})$ and their weights $\lambda_j(\boldsymbol{x})$,

---

[1] See the details of the derivation in [89, 104]

i.e. the matrix-valued mapping $A(\boldsymbol{x})$? In [89] the matrix-valued field is chosen to represent the known structural information within the domain. The structural information can, for example, be extracted from some other imaging modality. In this thesis the eigenvectors are chosen to be the directional vectors in cylindrical coordinates. In other words, the smoothness with respect to radius, angle and height can be assumed to be different. Note also that this approach allows one to assume nonhomogeneous anisotropic smoothness.

The gradient $\nabla\boldsymbol{\sigma}(\boldsymbol{x_k})$ can be computed as follows. Derivation follows the reference [104]. Let $[\sigma_1^k, \sigma_2^k, \sigma_3^k, \sigma_4^k] = \boldsymbol{\sigma}(\mathcal{I}_k)$ be the conductivity values in the nodes of the k^{th} element. Furthermore, the $\mathcal{I}_k$ is the index set for the nodes of the k^{th} element. The differences between the first node and remaining ones can be obtained by

$$\begin{aligned}
\sigma_4^k - \sigma_1^k &= \nabla\boldsymbol{\sigma} \cdot (\boldsymbol{g}(\mathcal{I}^k(4))^T - \boldsymbol{g}(\mathcal{I}^k(1))^T) \\
\sigma_3^k - \sigma_1^k &= \nabla\boldsymbol{\sigma} \cdot (\boldsymbol{g}(\mathcal{I}^k(3))^T - \boldsymbol{g}(\mathcal{I}^k(1))^T) \\
\sigma_2^k - \sigma_1^k &= \nabla\boldsymbol{\sigma} \cdot (\boldsymbol{g}(\mathcal{I}^k(2))^T - \boldsymbol{g}(\mathcal{I}^k(1))^T),
\end{aligned}$$

which can be written in matrix form

$$\begin{bmatrix} \sigma_4^k - \sigma_1^k \\ \sigma_3^k - \sigma_1^k \\ \sigma_2^k - \sigma_1^k \end{bmatrix} = \underbrace{\begin{bmatrix} x_4 - x_1 & y_4 - y_1 & z_4 - z_1 \\ x_3 - x_1 & y_3 - y_1 & z_3 - z_1 \\ x_3 - x_1 & y_2 - y_1 & z_2 - z_1 \end{bmatrix}}_{X_k} \begin{bmatrix} \frac{\partial\boldsymbol{\sigma}^k}{\partial x} \\ \frac{\partial\boldsymbol{\sigma}^k}{\partial y} \\ \frac{\partial\boldsymbol{\sigma}^k}{\partial z} \end{bmatrix}, \tag{3.52}$$

from which the gradient can be solved as

$$\begin{aligned}
\begin{bmatrix} \frac{\partial\boldsymbol{\sigma}^k}{\partial x} \\ \frac{\partial\boldsymbol{\sigma}^k}{\partial y} \\ \frac{\partial\boldsymbol{\sigma}^k}{\partial z} \end{bmatrix} &= \underbrace{X_k^{-1} \begin{bmatrix} -1 & 0 & 0 & 1 \\ -1 & 0 & 1 & 0 \\ -1 & 1 & 0 & 0 \end{bmatrix}}_{\mathcal{Q}_k \in \mathbb{R}^{3\times 4}} \begin{bmatrix} \sigma_1^k \\ \sigma_2^k \\ \sigma_3^k \\ \sigma_4^k \end{bmatrix} && (3.53) \\
&= \mathcal{Q}_k \boldsymbol{\sigma}(\mathcal{I}_k). && (3.54)
\end{aligned}$$

Furthermore

$$\begin{aligned}
v_j^T(\boldsymbol{x}_k)\nabla(\boldsymbol{\sigma}(\boldsymbol{x_k}) - \boldsymbol{\sigma}^*(\boldsymbol{x_k})) &= (v_{j1}(\boldsymbol{x}_k), v_{j2}(\boldsymbol{x}_k), v_{j3}(\boldsymbol{x}_k))\, \mathcal{Q}_k(\boldsymbol{\sigma}(\mathcal{I}_k) - \boldsymbol{\sigma}^*(\mathcal{I}_k)) \\
&= \widehat{\mathcal{Q}}(\boldsymbol{\sigma}(\mathcal{I}_k) - \boldsymbol{\sigma}^*(\mathcal{I}_k)), \quad \widehat{\mathcal{Q}} \in \mathbb{R}^{1\times 4} \\
&= L_{j,k}(\mathcal{I}_k)(\boldsymbol{\sigma} - \boldsymbol{\sigma}^*), && (3.55)
\end{aligned}$$

where $L_{j,k}(\mathcal{I}_k)$ is a zero row vector of length N such that the values of the vector $\widehat{\mathcal{Q}}$ is located to the locations $\mathcal{I}_k$. Now the functional (3.51) can be written in the form

$$\begin{aligned}
W(\boldsymbol{\sigma}) &= \sum_{j=1}^{3}\sum_{k=1}^{M} |\Omega||\lambda_j(\boldsymbol{x}_k) L_{j,k}(\boldsymbol{\sigma} - \boldsymbol{\sigma}^*)|^2 \\
&= \sum_{j=1}^{3} \|\widehat{\lambda}_j L_j(\boldsymbol{\sigma} - \boldsymbol{\sigma}^*)\|, && (3.56)
\end{aligned}$$

where the matrices L_j are the following matrices corresponding to the chosen directions r, θ and z

$$L_r = \begin{bmatrix} L_{r,1} \\ \vdots \\ L_{r,M} \end{bmatrix}, L_\theta = \begin{bmatrix} L_{\theta,1} \\ \vdots \\ L_{\theta,M} \end{bmatrix} \text{ and } L_z = \begin{bmatrix} L_{z,1} \\ \vdots \\ L_{z,M} \end{bmatrix} \tag{3.57}$$

and $\widehat{\lambda}_j = \mathrm{diag}(\sqrt{|\Omega_k|}\lambda_j(\boldsymbol{x}_k)), k = 1, \ldots, M, j = r, \theta$ or z. The $\widehat{\lambda}_j$ are considered as the regularization parameters with respect to the radius, angle and height. The final regularization functional can be written in the form

$$W(\boldsymbol{\sigma}) = \left\| \begin{bmatrix} \widehat{\lambda}_r L_r(\boldsymbol{\sigma} - \boldsymbol{\sigma}^*) \\ \widehat{\lambda}_\theta L_\theta(\boldsymbol{\sigma} - \boldsymbol{\sigma}^*) \\ \widehat{\lambda}_z L_z(\boldsymbol{\sigma} - \boldsymbol{\sigma}^*) \end{bmatrix} \right\|^2 . \tag{3.58}$$

From the statistical point of view $\widehat{\lambda}_j$'s are the weights of the matrices $L_j^T L_j$ which are the covariance matrices corresponding to the directions along the radius, angle and height. In other words, they change the variances and covariances of the each individual parameters. Obviously, homogeneous smoothness prior can be obtained by choosing the same values for $\lambda_j(\boldsymbol{x}_k)$ for all k. In this case the $\widehat{\lambda}_j$'s can be simply replaced with scalars.

If the conductivity is approximated in the piecewise constant basis the construction of the anisotropic smoothness prior is different. The conductivity distribution is discretized as follows

$$\sigma(\boldsymbol{x}) = \sum_{i=1}^{m} \sigma_i \chi_i(\boldsymbol{x}), \tag{3.59}$$

where χ_i are the characteristic functions of the finite elements. On the basis of this choice, the difference matrix $L \in \mathbb{R}^{m \times m}$ can be obtained, for example, as follows. The i^{th} row of L is

$$L_{i,\cdot} = (0, \ldots, 0, -1, \ldots, -1, 0, \ldots, 0, 3, \ldots, 0, -1, \ldots, 0), \tag{3.60}$$

where 3 is placed in the i^{th} column and -1 are placed in the columns corresponding to the elements having common edge with the i^{th} element. If the element i is on the boundary having one edge as a part of the surface, then there will be only two adjacent elements and the value 3 is replaced by 2 in $L_{i,\cdot}$, see Figure 3.7.

In the case of 2D anisotropic prior, two different parts of the row $L_{i,\cdot}$, namely $L_{i,r} = (w_1^r, \ldots, w_t^r)$ and $L_{i,\theta} = (w_1^\theta, \ldots, w_u^\theta)$ are defined. The vectors correspond to radial and angular regularization, respectively. The t and u are the numbers of the adjacent elements in radial and angular directions, respectively. For example if it is assumed that the conductivity distribution is smoother in angular direction than in radial direction the adjacent elements in angular direction have bigger weight than the elements in radial direction. More presicely the weight vectors might be as follows $L_{i,r} = (-2, -2)$ and $L_{i,\theta} = (-0.5)$. Also the number 3 has to be replaced with the absolute value of the componentwise sum of the vectors, i.e. in this case 4.5.

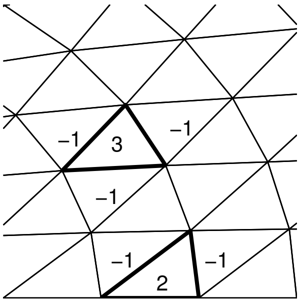

Figure 3.7: The construction of the standard smoothness prior.

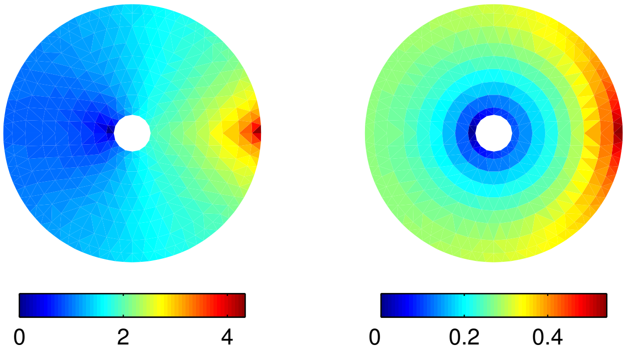

(a) (b)

Figure 3.8: Conditional prior covariances of the elements corresponding to the anisotropic priors. The value of the fixed parameter is set to zero. (a) $w_m^\theta = 1$, for all m, $w_m^r = 1$, for all m. (b) $w_m^\theta = 30$ for all m and $w_m^r = 1$ for all m.

PROPER SMOOTHNESS PRIOR MODEL

Smoothness type of prior models, presented above, are improper. This is due to the fact that the difference operators have non-trivial null space [‡]. A Gaussian smoothness prior model that is proper can be constructed as follows [88].

The parameter vector is reordered such that $\boldsymbol{\sigma} = [\boldsymbol{\sigma}_{\mathcal{I}_1}\ \boldsymbol{\sigma}_{\mathcal{I}_2}]^T$, where the $\boldsymbol{\sigma}_{\mathcal{I}_1}$ are free parameters and the $\boldsymbol{\sigma}_{\mathcal{I}_2}$ fixed parameters. The difference operator is also partitioned as follows

$$L^T L = \begin{bmatrix} B_{11} & B_{12} \\ B_{21} & B_{22} \end{bmatrix} \tag{3.61}$$

[‡] $N(D) = \{x \mid Dx = 0,\ x \neq 0\}$.

The fixed parameters are assumed to be Gaussian distributed, that is $\boldsymbol{\sigma}_{\mathcal{I}_2} \sim N(\boldsymbol{\sigma}^*_{\mathcal{I}_2}, \Gamma_2)$, where the mean and the covariance matrix are a priori known. It can be shown that the proper Gaussian smoothness prior can be written in the form [88]

$$\begin{aligned}\pi(\boldsymbol{\sigma}) &= \pi(\boldsymbol{\sigma}_{\mathcal{I}_1} \mid \boldsymbol{\sigma}_{\mathcal{I}_2})\pi(\boldsymbol{\sigma}_{\mathcal{I}_2}) \\ &\propto \exp\Big(-\alpha(\boldsymbol{\sigma}_{\mathcal{I}_1} + B_{11}^{-1}B_{12}\boldsymbol{\sigma}_{\mathcal{I}_2})^T B_{11}(\boldsymbol{\sigma}_{\mathcal{I}_1} + B_{11}^{-1}B_{12}\boldsymbol{\sigma}_{\mathcal{I}_2}) \\ &\qquad -\frac{1}{2}(\boldsymbol{\sigma}_{\mathcal{I}_2} - \boldsymbol{\sigma}^*_{\mathcal{I}_2})^T\Gamma_2^{-1}(\boldsymbol{\sigma}_{\mathcal{I}_2} - \boldsymbol{\sigma}^*_{\mathcal{I}_2})\Big) \\ &= \exp\Big(-\frac{1}{2}(\boldsymbol{\sigma} - \boldsymbol{\sigma}^*)^T\Gamma^{-1}(\boldsymbol{\sigma} - \boldsymbol{\sigma}^*)\Big) \qquad (3.62)\end{aligned}$$

where the mean and covariance matrix are

$$\boldsymbol{\sigma}^* = \begin{bmatrix} -B_{11}^{-1}B_{12}\boldsymbol{\sigma}^*_{\mathcal{I}_2} \\ \boldsymbol{\sigma}^*_{\mathcal{I}_2} \end{bmatrix} \qquad (3.63)$$

$$\Gamma = \begin{bmatrix} 2\alpha B_{11} & 2\alpha B_{12} \\ 2\alpha B_{21} & 2\alpha B_{21}B_{11}^{-1}B_{12} + \Gamma_2^{-1} \end{bmatrix}. \qquad (3.64)$$

It can be seen from the equation (3.63), that the mean of the fixed parameters is $\boldsymbol{\sigma}^*_{\mathcal{I}_2}$, as it should be and the mean of the free parameters depends on $\boldsymbol{\sigma}^*_{\mathcal{I}_2}$, on the variances and covariances of the free parameters through the block matrix B_{11} and on the correlations between the fixed and free parameters through the block matrix B_{12}. Furthermore, it can be seen from the equation (3.64), that the covariances of the free parameters depend only on the block matrix B_{11}. In other words, the correlation between the free parameters depends on the original smoothness prior model but not on the correlations of the fixed parameters. Strength of the correlation can be tuned by using a parameter α. The final covariances of the fixed parameters depend on the given covariances of the fixed parameters Γ_2, on the correlation between free parameters and on the correlation between the free and fixed parameters. This prior model is used in 3D laboratory test in Section 7.4.

Note that the conditional density $\pi(\boldsymbol{\sigma}_{\mathcal{I}_1} \mid \boldsymbol{\sigma}_{\mathcal{I}_2})$ can be used for visualization of the improper prior density. This can be done by fixing some parameters and viewing the prior density of the remaining ones conditioned on the fixed ones. Visualization of the anisotropic smoothness prior derived earlier is shown in Figure 3.8. Two conditional prior covariances have been computed with different prior assumptions (different weights w_m^r and w_m^θ). The effect of the weight can be well seen in the case when there is the smoothness assumption in the angular direction, see Figure 3.8(b). Large weights w_m^θ tend to give high correlation in the angular direction and the correlation drops down very quickly in the radial direction (small w_m^r).

3.3.3 Posterior density and solution strategies

According to Section 2.3, the solution of the EIT inverse problem is the posterior probability density function, that is,

$$\begin{aligned} \pi(\boldsymbol{\sigma} \mid \boldsymbol{V}) &= \frac{\pi(\boldsymbol{V} \mid \boldsymbol{\sigma})\pi(\boldsymbol{\sigma})}{\pi(\boldsymbol{V})} \\ &\propto \pi(\boldsymbol{V} \mid \boldsymbol{\sigma})\pi(\boldsymbol{\sigma}). \end{aligned} \tag{3.65}$$

In this thesis mainly the MAP-estimate is computed. Also the MAP-estimate of the linearized problem is used. Both of these are introduced here. Since in both methods the Jacobian of the forward mapping is needed, the computation of the Jacobian is introduced first.

COMPUTATION OF JACOBIAN

The Jacobian matrix is defined as

$$J = \frac{\partial U(\boldsymbol{\sigma}, \boldsymbol{z})}{\partial \boldsymbol{\sigma}} = \begin{bmatrix} \frac{\partial U^{(1)}}{\partial \sigma_1} & \cdots & \frac{\partial U^{(1)}}{\partial \sigma_M} \\ \vdots & \ddots & \vdots \\ \frac{\partial U^{(K)}}{\partial \sigma_1} & \cdots & \frac{\partial U^{(K)}}{\partial \sigma_M} \end{bmatrix}, \tag{3.66}$$

where $U^{(k)}$ is the vector $U^{(k)} = \mathcal{R}(\boldsymbol{\sigma}, \boldsymbol{z})I^{(k)}$. The Jacobian matrix can be computed using either the *adjoint differentiation* [13, 87] or the *standard method* [168]. Here the adjoint differentiation method is introduced. In this section, differentiation with respect to the conductivity is presented. The Jacobian with respect to the contact impedances is introduced in Section 4.2.1.

The computed voltages according to equation (3.43) are

$$U^h_{\text{actual}} = \tilde{M}\boldsymbol{\theta}. \tag{3.67}$$

The derivation of the voltages with respect to conductivity $\sigma_k, k = 1, \ldots, m$ can be obtained by

$$\frac{\partial U^h_{\text{actual}}}{\partial \sigma_k} = \tilde{M}\frac{\partial \boldsymbol{\theta}}{\partial \sigma_k}. \tag{3.68}$$

The term $\partial\boldsymbol{\theta}/\partial\sigma_k$ can be obtained from the equation (3.32) as follows

$$\frac{\partial \boldsymbol{\theta}}{\partial \sigma_k} = -A^{-1}\frac{\partial A}{\partial \sigma_k}A^{-1}\boldsymbol{f}. \tag{3.69}$$

Now, the derivatives with respect to the actual measurements are

$$\tilde{M}\frac{\partial \boldsymbol{\theta}}{\partial \sigma_k} = -\tilde{M}A^{-1}\frac{\partial A}{\partial \sigma_k}A^{-1}\boldsymbol{f} \tag{3.70}$$

$$= -[(A^{-1})^T\tilde{M}^T]^T\frac{\partial A}{\partial \sigma_k}A^{-1}\boldsymbol{f} \tag{3.71}$$

$$= -[\underbrace{A^{-1}\tilde{M}^T}_{\text{adjoint field}}]^T\frac{\partial A}{\partial \sigma_k}\underbrace{A^{-1}\boldsymbol{f}}_{\text{actual field}}, \tag{3.72}$$

where $A^{-1}\boldsymbol{f} \in \mathbb{R}^{(N+L-1)\times K}$ is the actual field (electrical potential u within the domain) and $A^{-1}\tilde{M}^T \in \mathbb{R}^{N\times Q}$ is the so-called *adjoint field.* That is the hypothetical electrical potential $\tilde{u}$ within the domain such that the current pattern is replaced with the measurement pattern $\tilde{M}^T$. The method is named according to this feature.

The term $\partial A/\partial\sigma_k$ in equation (3.72) can be computed from the equation (3.34) as

$$\frac{\partial A}{\partial \sigma_k} = \begin{bmatrix} \frac{\partial B}{\partial \sigma_k} & 0 \\ 0 & 0 \end{bmatrix}, \tag{3.73}$$

where

$$\frac{\partial B_{i,j}}{\partial \sigma_k} = \int_{\Omega_k} \nabla\varphi_i \cdot \nabla\varphi_j \mathrm{d}x\mathrm{d}y, \quad 1 \leq i,j \leq N. \tag{3.74}$$

It is assumed here that the piecewise constant basis function for the conductivity distribution is used. Computation of the Jacobian with respect to resistivity distribution differ only by term (3.74), which is of the form

$$\frac{\partial B_{i,j}}{\partial \rho_k} = -\frac{1}{\rho_k^2}\int_{\Omega_k} \nabla\varphi_i \cdot \nabla\varphi_j \mathrm{d}x\mathrm{d}y, \quad 1 \leq i,j \leq N. \tag{3.75}$$

If the conductivity is presented in piecewise linear basis the term (3.74) is of the form

$$\begin{aligned} \frac{\partial B_{i,j}}{\partial \sigma_k} &= \frac{\partial}{\partial \sigma_k}\int_{\Omega} \sum_{p=1}^{N} \sigma_p\varphi_p \nabla\varphi_i \cdot \nabla\varphi_j \mathrm{d}x\mathrm{d}y && (3.76) \\ &= \int_{\mathrm{supp}(\varphi_k)} \varphi_k \nabla\varphi_i \cdot \nabla\varphi_j \mathrm{d}x\mathrm{d}y, \quad 1 \leq i,j \leq N, && (3.77) \end{aligned}$$

where $\mathrm{supp}(\varphi_k)$ is the support of the basis functions corresponding to the k^{th} node.

Finally, inserting (3.73) into (3.72) is obtained

$$\tilde{M}\frac{\partial \theta}{\partial \sigma_k} = -[A^{-1}\tilde{M}^T]^T \frac{\partial B}{\partial \sigma_k}\tilde{\alpha}, \tag{3.78}$$

where $\tilde{\alpha} \in \mathbb{R}^{N\times K}$. The obtained matrix is $\mathbb{R}^{Q\times K}$, where Q is the number of the actual measurements for the single current pattern and K the number of current patterns. After reshaping the ℓ^{th} column of the Jacobian is obtained. The same procedure is carried out for each parameter to obtain the other columns of the Jacobian.

MAXIMUM A POSTERIOR SOLUTION

The MAP-estimate in the nonlinear case can be computed using the iterative formula (2.32) which is now of the form

$$\boldsymbol{\sigma}_{i+1} = \boldsymbol{\sigma}_i + \kappa_i \left[J_i^T \Gamma_v^{-1} J_i + \Gamma_{\mathrm{pr}}^{-1} \right]^{-1} \left[J_i^T \Gamma_v^{-1} (\boldsymbol{V} - U(\boldsymbol{\sigma}_i)) - \Gamma_{\mathrm{pr}}^{-1} (\boldsymbol{\sigma_i} - \boldsymbol{\sigma}^*) \right] \tag{3.79}$$

In the beginning of the iteration initial conductivity distribution has to be known. Usually a homogeneous distribution is chosen. A method for the computatation of the best homogeneous distribution is presented e.g. in [171].

The optimal step length κ_i can be obtained by minimizing the following one-dimensional function

$$F(\kappa_i) = \|\boldsymbol{V} - U(\sigma_i + \kappa_i \delta\sigma_i)\|^2, \tag{3.80}$$

where s_i is the current state of the conductivity distribution and δs_i is the change of the distribution to the direction of the negative gradient. In the literature this method is called the line–search procedure [135]. Here a simple method [104] is used in which the search is first made adaptively for three points $\{\kappa_1, \kappa_2, \kappa_3\}$ such that $0 < \kappa_1 < \kappa_2 < \kappa_3$ and $F(\kappa_2) \leq \min\{F(\kappa_1), F(\kappa_3)\}$. After that a second order polynomial fitting is made to these points and the minimum of the fitted polynomial is used as an approximation for the optimal step length.

Difference reconstruction

Difference reconstruction method is based on linearization (2.31). In this case the model (3.45) can be written in the form

$$\boldsymbol{V} = U(\boldsymbol{\sigma}_0) + J_0(\boldsymbol{\sigma} - \boldsymbol{\sigma}_0), \tag{3.81}$$

where the vector $U(\boldsymbol{\sigma}_0)$ can be measured with a reference conductivity distribution $\boldsymbol{\sigma}_0$. The Jacobian J_0 is computed at the conductivity distribution $\boldsymbol{\sigma}_0$. Furthermore

$$\underbrace{\boldsymbol{V} - U(\boldsymbol{\sigma}_0)}_{\delta \boldsymbol{v}} = J_0 \underbrace{(\boldsymbol{\sigma} - \boldsymbol{\sigma}_0)}_{\delta \boldsymbol{\sigma}}, \tag{3.82}$$

where $\delta\boldsymbol{v}$ is the difference between the actual measurements and the reference measurements. In this case, the reconstructed quantity is the conductivity difference $\delta\boldsymbol{\sigma}$. In other words, the objective is to find the changes in conductivity distribution based on the difference data set $\delta\boldsymbol{v}$. The equation (3.82) is linear and it has the same form as the equation (2.18). In principle, ML-estimate can be calculated. Unfortunately, the Jacobian is ill-conditioned and thus in order to obtain satisfactory estimate prior information has to be used. This means that the MAP-estimate has to be found. According to the equation (2.27), for the linear case, the MAP-estimate can be written in the form

$$\delta\boldsymbol{\sigma}_{\mathrm{MAP}} = [J_0^T \Gamma_{\delta v}^{-1} J_0 + \Gamma_{\mathrm{pr}}^{-1}]^{-1} [J_0^T \Gamma_{\delta v}^{-1} \delta\boldsymbol{v} + \Gamma_{\mathrm{pr}}^{-1} \delta\boldsymbol{\sigma}^*], \tag{3.83}$$

where the mean $\delta\boldsymbol{\sigma}^*$ is zero and thus

$$\begin{aligned} \delta\boldsymbol{\sigma}_{\mathrm{MAP}} &= \underbrace{[J_0^T \Gamma_{\delta v}^{-1} J_0 + \Gamma_{\mathrm{pr}}^{-1}]^{-1} J_0^T \Gamma_{\delta v}^{-1}}_{K} \delta\boldsymbol{v} \\ &= K \delta\boldsymbol{v}. \end{aligned} \tag{3.84}$$

The MAP-estimate is the mean of the following Gaussian density

$$\pi(\delta\boldsymbol{\sigma} \mid \delta\boldsymbol{v}) = \exp\left(-\frac{1}{2}(\delta\boldsymbol{\sigma} - \delta\boldsymbol{\sigma}_{\mathrm{MAP}})^T \tilde{\Gamma}^{-1}(\delta\boldsymbol{\sigma} - \delta\boldsymbol{\sigma}_{\mathrm{MAP}}), \right), \tag{3.85}$$

where the covariance matrix is

$$\tilde{\Gamma}^{-1} = [J_0^T \Gamma_{\delta v}^{-1} J_0 + \Gamma_{\mathrm{pr}}^{-1}]^{-1}. \tag{3.86}$$

Usually the reference conductivity distribution $\boldsymbol{\sigma}_0$ has to be estimated for the computation of the Jacobian and thus the equation (3.84) can be written in the form

$$\boldsymbol{\sigma} = \boldsymbol{\sigma}_0 + K\delta\boldsymbol{v}, \tag{3.87}$$

which is called here *semi-absolute reconstruction.* Note that the matrix K can be pre-calculated and therefore this approach requires only a matrix-vector multiplication. This allows a fast image reconstruction procedure. Accuracy of the method depends on the nonlinearity of the mapping $U(\boldsymbol{\sigma})$ and therefore the basic assumption is that the conductivity distribution does not differ much from the reference distribution $\boldsymbol{\sigma}_0$. It should also be noted that the difference reconstruction method is tolerant for modeling errors. This method is used in practical measurements in Chapter 7.

3.4 Measurement strategies

Important issue in EIT measurement system is that the voltage measurements are as accurate as possible. Also almost as important issue is that the measurements have to contain as much information on the conductivity distribution as possible. Measurement strategy therefore is one of the most crucial parts of the EIT measurement system.

There are two different measurement strategies in the data acquisition. These are *two-* and *four-electrode methods.* In the two-electrode method the voltages are measured from the same electrodes through which the current is injected, whereas in the four-electrode method the voltages are not measured from the current carrying electrodes. The four-electrode method is less sensitive to the uncertainty in the values of the contact impedances. This is due to the high input impedance of the voltage measurement unit.

3.4.1 Current injection

Many different strategies for the current injection have been developed [19, 131, 15, 16, 84, 112, 91]. These methods are developed mainly for 2D cases. The current injection strategies can be divided into two classes which are *pair* and *multiple drive methods.* The sensitivity of EIT depends on the current density within the object. In other words in the areas where the current density is low the conductivity changes[†] may not cause detectable changes on the measured voltages at least within the accuracy limit of the voltage measurement unit. The current density should therefore be as uniform as possible.

[†] It does not matter how big the change is.

PAIR INJECTION

In pair drive methods the current is injected to the object through a pair of electrodes. The most widely used pair drive methods are *adjacent drive* and *opposite drive* methods. In the adjacent drive method the current is injected to the object through two adjacent electrodes and the voltages are measured from all the other pairs of passive electrodes. This procedure is repeated for all the electrodes. The number of the voltage measurements is $L(L-3)$. Half of these are independent which is due to the reciprocity theorem and therefore usually only $L(L-3)/2$ measurements are used. The reciprocity theorem states that reversing the voltage and current injection electrodes would give an identical value of the conductivity [182]. The current density within the object produced by adjacent method is nonuniform since most of the current flows near the boundary of the object.

In the opposite drive method the current is injected to the object through diametrically opposite pairs of electrodes. This method is also called *polar drive method.* The voltages are measured from all the passive electrodes with respect to one passive reference electrode adjacent to the current electrode. This method produces more uniform current density within the object and thus the sensitivity of the method is better than with the adjacent drive method. Moreover, the problem with the opposite method is not so ill-posed as with the adjacent method [16]. In other words, the condition of the matrix that is to be inverted is better when the sensitivity is uniform over the entire region of interest [76]. Furthermore, the signal to noise ratio (SNR) of the measured data is worse in the adjacent method [16].

In pair drive methods only one current source is used. In this case switches that choose the electrodes that are used to current injection are required. If one can use multiple current sources, the magnitude of each source can be controlled individually and any desired current pattern is possible. This arrangement leads to the concept of the multiple current drive methods which are considered next.

MULTIPLE INJECTION

In multiple drive methods current is applied to all the electrodes simultaneously and the voltages are measured from the same electrodes with respect to some reference electrode. Usually in multiple drive methods current injection is optimized in some sense. Most widely used optimization criterion is to maximize the distinguishability of two conductivity distributions $\boldsymbol{\sigma}_1$ and $\boldsymbol{\sigma}_2$ with respect to current I [84], that is,

$$\max_{\|I\|=1} \frac{\|\mathcal{R}(\boldsymbol{\sigma}_1, \boldsymbol{z})I - \mathcal{R}(\boldsymbol{\sigma}_2, \boldsymbol{z})I\|}{\|I\|} = \max_{\|I\|=1} \frac{\|DI\|}{\|I\|}, \tag{3.88}$$

where $D = \mathcal{R}(\boldsymbol{\sigma}_1, \boldsymbol{z}) - \mathcal{R}(\boldsymbol{\sigma}_2, \boldsymbol{z})$. The norm used in the original definition is two-norm, i.e. $\|\cdot\| \doteq \|\cdot\|_2$. It has been shown that the optimal current pattern that maximize (3.88) is the eigenvector of the operator D^2 that has the largest eigenvalue [84]. The second best current pattern is the eigenvector corresponding to the second largest eigenvalue and so on. All eigenvectors v_k of D^2 for which $|\lambda_k| > \epsilon$ are the best current patterns to apply in order to distinguish $\boldsymbol{\sigma}_1$ from $\boldsymbol{\sigma}_2$

with measurement precision ϵ. There are several modifications of this approach [36, 102, 112]. The approach in which the power consumption is normalized is presented in [36]. This is essential feature specially in medical application of EIT. In the papers [102, 112] different constraints for the current pattern have been applied.

Based on the definition (3.88) it has been shown in [84] that the optimal current patterns to distinguish a centered rotation invariant disc from otherwise homogeneous disc are of the form

$$I_\ell^k = \begin{cases} I_k \cos(k\theta_\ell) & 1 \le \ell \le L, \quad 1 \le k \le L/2, \\ I_k \sin((k - L/2)\theta_\ell) & 1 \le \ell \le L, \quad L/2 < k \le L-1, \end{cases} \tag{3.89}$$

where $\theta_\ell = 2\pi\ell/L$ is the angular location of the midpoint of the electrode e_ℓ, k is the spatial frequency, and I_k is the amplitude of the applied current. These current patterns are called *trigonometric current patterns.*

It should be emphasized here that the optimal current patterns depend on the unknown conductivity distribution which is not necessarily rotationally invariant. In these cases the optimal current patterns can be estimated adaptively based on the measured data and the current estimate of the conductivity distribution [61]. These current patterns are called *adaptive current patterns.*

The current patterns can also be optimized based on the statistical inversion theory. A method in which the selection of the current pattern is viewed as a Bayesian optimal experimental design problem is presented in [91]. In this framework the aim is to find measurements that minimize the uncertainty of the parameters to be estimated. In that paper the trace of the posterior covariance matrix is minimized with respect to current patterns. In other words the minimum of the sum of the individual parameter variances has to be found. It was also shown in this paper that in some cases only a few current patterns are needed in order to extract most of the information available in EIT measurements. This method is applicable for both 2D and 3D cases and it is also further developed for nonstationary estimation problem in [90].

It has been shown that the optimal current injection methods produce the most uniform current density [40]. However, these methods need as many current generators for current injection as there are electrodes. This makes measurement system more complicated than the system with one current generator. Also, all individual current generators have to be identical which makes manufacturing of the generators more challenging. Also the calibration of the current injection part of the system has to be performed carefully. Normally, in multiple drive methods, the voltages are measured from the current carrying electrodes which causes problem with contact impedance. This problem can be avoided either by using compound electrodes [80] or by estimating the values of the contact impedances as will be presented in Chapter 4.

The number of the independent current injections increase radically in 3D. The current injection methods for 3D are not so widely studied in literature. One study has been presented in [131, 130]. In this study four different current injection methods have been examined. Two of these were studied only with numerical simulations which was due to the practical limitations of the data collection system. Currently this is a very common restriction for wider use of efficient 3D current injection protocols.

3.4.2 Voltage measurement

The voltages on the electrodes are measured with respect to some reference electrode. There are two possibilities to choose the reference electrode. In traditional data collection scheme the voltages are measured differentially between the adjacent pairs of electrodes. In other words the reference electrode is changed for each measurement. Another possible way is to use one fixed reference electrode for all the measurements.

CHAPTER IV

Estimation of contact impedance

4.1 Introduction

In process applications electrodes usually have electrical contact with process liquid within the domain. From the physical point of view metal and liquid have different kind of Fermi level of their electron bands. Since Fermi levels cannot have discontinuity, the Fermi level is bent over the contact area. This bending is observed as voltage drop across the contact area, which is considered as a *contact impedance* [66]. In other words, the voltage drop appears when ohmic current in wire is changed to ionic current in liquid. In medical applications of EIT there are also other factors that are usually added to the contact impedance. These factors are for example skin impedance and electrode gel impedance [126]. In principle the contact impedance can be modelled as resistors in series with the fluid resistance. The unit of the contact impedance is therefore Ω.

The contact impedance is inversely proportional to the area of the electrode [79]. Therefore by increasing the size of the electrodes the value of the contact impedance can be decreased. Moreover, the wide electrodes yield better distinguishability [84] and the current density is more uniform within the domain [79]. The drawback of the wide electrodes is that the shunting effect is more remarkable[‡]. Usually *the effective contact impedance* is used instead of contact impedance. The effective contact impedance is the product of the contact impedance and the area of the electrode. The unit of the effective contact impedance is therefore $\Omega\mathrm{cm}^2$ [39]. In the complete electrode model (3.25) the effective contact impedance is used. Note also that the contact impedance might also be a complex-valued quantity. The presence of the imaginary part of the contact impedance causes phase shift between the injected current and measured voltage.

It has been shown that inaccurate knowledge of the contact impedance cause image distortion [79]. There are also several other studies in which this is verified, see e.g. [27, 105]. It was also shown in Chapter 3 that the estimation of the contact impedance is important issue in the modeling of the measurement. This

---

[‡] The details of the shunting effect, see page 42

is specially the case in the situations in which absolute value of the conductivity distribution is of interest.

The effect of the contact impedance can be minimized by removing the voltage measurements made on current-carrying electrodes (four-electrode measurement) but it has been shown that in this case the noise level of the reconstructed image is higher [40]. In that study it is concluded that the voltage should be measured from all available electrodes. This is due to the fact that the measurements made on current-carrying electrodes are most sensitive to changes in conductivity distribution. This requirement necessitates accurate knowledge of the contact impedance.

A method of measuring the skin impedance in medical applications of EIT is presented in [190]. In principle this method is applicable for industrial settings as well. The contact impedance can also be estimated using a cylindrical test cell filled with material of interest having the electrodes at the both ends of the cell [175]. In this chapter the estimation method based on framework presented in Chapter 2 and complete electrode model is introduced, see also [175, 69].

4.2 Estimation procedure

The observation model is of the form

$$\boldsymbol{V} = U(\boldsymbol{\sigma}, \boldsymbol{z}) + \boldsymbol{v}, \tag{4.1}$$

where $\boldsymbol{V}$ are measured voltages, $U(\boldsymbol{\sigma}, \boldsymbol{z})$ are computed voltages by using the forward model (3.2) and $\boldsymbol{v}$ is zero–mean Gaussian noise with covariance matrix Γ_v. It is also assumed here that $z_\ell \in \mathbb{R} \; \forall \; \ell$. The likelihood density $\pi(\boldsymbol{V} \mid \boldsymbol{\sigma}, \boldsymbol{z})$ is now of the form

$$\pi(\boldsymbol{V} \mid \boldsymbol{\sigma}, \boldsymbol{z}) \propto \exp\left\{-\frac{1}{2}(\boldsymbol{V} - U(\boldsymbol{\sigma}, \boldsymbol{z}))^T \Gamma_v^{-1} (\boldsymbol{V} - U(\boldsymbol{\sigma}, \boldsymbol{z}))\right\}. \tag{4.2}$$

It is assumed that the parameters can be stacked to a vector as $\boldsymbol{\theta} = [\boldsymbol{\sigma} \; \boldsymbol{z}]^T$ and that the $\boldsymbol{\sigma}$ and the $\boldsymbol{z}$ are independent, i.e. $\pi(\boldsymbol{\sigma}, \boldsymbol{z}) = \pi(\boldsymbol{\sigma})\pi(\boldsymbol{z})$. The Gaussian prior density for $\boldsymbol{\theta}$ can be written in the form

$$\begin{aligned} \pi(\boldsymbol{\theta}) &\propto \exp\left(-\frac{1}{2}(\boldsymbol{\theta} - \boldsymbol{\theta}^*)^T \Gamma_\theta^{-1} (\boldsymbol{\theta} - \boldsymbol{\theta}^*)\right) & (4.3) \\ &= \exp\left(-\frac{1}{2} \underbrace{\begin{bmatrix} \boldsymbol{\sigma} - \boldsymbol{\sigma}^* \\ \boldsymbol{z} - \boldsymbol{z}^* \end{bmatrix}^T}_{(\boldsymbol{\theta} - \boldsymbol{\theta}^*)^T} \underbrace{\begin{bmatrix} \Gamma_\sigma^{-1} & \mathbf{0} \\ \mathbf{0} & \Gamma_z^{-1} \end{bmatrix}}_{\Gamma_\theta^{-1}} \underbrace{\begin{bmatrix} \boldsymbol{\sigma} - \boldsymbol{\sigma}^* \\ \boldsymbol{z} - \boldsymbol{z}^* \end{bmatrix}}_{(\boldsymbol{\theta} - \boldsymbol{\theta}^*)}\right). & (4.4) \end{aligned}$$

The $\boldsymbol{\sigma}^*$ and $\boldsymbol{z}^*$ are the mean of conductivity distribution and of the contact impedances, respectively (see Chapter 2). According to equation (2.6), the posterior density can be written in the non-normalized form

$$\pi(\boldsymbol{\theta} \mid \boldsymbol{V}) \propto \pi(\boldsymbol{V} \mid \boldsymbol{\theta})\pi(\boldsymbol{\theta}). \tag{4.5}$$

Now the posterior density (4.5) can be written in the form

$$\pi(\boldsymbol{\theta} \mid \boldsymbol{V}) \propto \exp\Bigg(-\frac{1}{2}\Big((\boldsymbol{V}-U(\boldsymbol{\theta}))^T\Gamma_v^{-1}(\boldsymbol{V}-U(\boldsymbol{\theta}))+(\boldsymbol{\theta}-\boldsymbol{\theta}^*)^T\Gamma_\theta^{-1}(\boldsymbol{\theta}-\boldsymbol{\theta}^*)\Big)\Bigg). \quad (4.6)$$

The prior density can be for example of the form

$$\Gamma_\theta = \begin{bmatrix} \alpha L^T L & \mathbf{0} \\ \mathbf{0} & \beta I \end{bmatrix}, \quad (4.7)$$

where L is the difference matrix and $\alpha, \beta > 0$ are the regularization parameters, see Section 3.3.2

As discussed in Chapter 2, the MAP estimate is found by minimizing the functional

$$\boldsymbol{\theta}_{\mathrm{MAP}} = \arg\min_{\theta}\Bigg\{\Big((\boldsymbol{V}-U(\boldsymbol{\theta}))^T\Gamma_v^{-1}(\boldsymbol{V}-U(\boldsymbol{\theta}))+(\boldsymbol{\theta}-\boldsymbol{\theta}^*)^T\Gamma_\theta^{-1}(\boldsymbol{\theta}-\boldsymbol{\theta}^*)\Big)\Bigg\}. \quad (4.8)$$

In this case the Gauss-Newton iteration is of the form

$$\boldsymbol{\theta}_{i+1} = \boldsymbol{\theta}_i + \kappa_i \delta\boldsymbol{\theta}_i, \quad (4.9)$$

where κ_i is a step length parameter. Furthermore, $\delta\boldsymbol{\theta}_i$ is given by the following formula

$$\delta\boldsymbol{\theta}_i = \Big[J_i^T\Gamma_v^{-1}J_i + \Gamma_\theta^{-1}\Big]^{-1}\Big[J_i^T\Gamma_v^{-1}(\boldsymbol{V}-U(\boldsymbol{\theta}_i)) - \Gamma_\theta^{-1}(\boldsymbol{\theta}_i-\boldsymbol{\theta}^*)\Big], \quad (4.10)$$

where $J_i = [J_i^\sigma \; J_i^z] \in \mathbb{R}^{N(L-1)\times M}$ is the Jacobian matrix of the forward mapping. The block matrices are of the form

$$J_i^\sigma = \frac{\partial U(\boldsymbol{\sigma},\boldsymbol{z})}{\partial \boldsymbol{\sigma}} \in \mathbb{R}^{N(L-1)\times P}, \quad (4.11)$$

$$J_i^z = \frac{\partial U(\boldsymbol{\sigma},\boldsymbol{z})}{\partial \boldsymbol{z}} \in \mathbb{R}^{N(L-1)\times L}, \quad (4.12)$$

$M = P+L$ is the number of parameters, where P is the number of the conductivity parameters and N is the number of the measurements. The computation of the part J_i^σ of the Jacobian was presented in Section 3.3.3 and the part J_i^z will be presented in Section 4.2.1.

If it is assumed that $\boldsymbol{\sigma}$ is homogeneous and the contact impedances $\boldsymbol{z}$ are equal on all the electrodes, there are only two parameters to be estimated, namely σ and z. In this case no prior for the parameters is needed since the problem is no longer ill–posed and the ML estimation can be used. It can be seen that the ML estimate can be found by minimizing

$$\boldsymbol{\theta}_{\mathrm{ML}} = \arg\min_{\theta}\Big\{(\boldsymbol{V}-U(\boldsymbol{\theta}))^T\Gamma_v^{-1}(\boldsymbol{V}-U(\boldsymbol{\theta}))\Big\}. \quad (4.13)$$

In this case $\delta\boldsymbol{\theta}_i$ in equation (4.9) is of the form

$$\delta\boldsymbol{\theta}_i = \Big[J_i^T\Gamma_v^{-1}J_i\Big]^{-1}\Big[J_i^T\Gamma_v^{-1}(\boldsymbol{V}-U(\boldsymbol{\theta}_i))\Big]. \quad (4.14)$$

The covariance for the estimates for each iteration step can be calculated as follows [147]

$$\Gamma_{\theta_{i+1}} = [J_i^T \Gamma_v^{-1} J_i]^{-1}. \tag{4.15}$$

The confidence limits are the square roots of the diagonal elements of $\Gamma_{\theta_{i+1}}$, i.e., the standard deviations of the estimated parameters.

4.2.1 Computation of the Jacobian with respect to the contact impedance

The Jacobian with respect to the contact impedance is formally as

$$J_z = \frac{\partial U(\boldsymbol{\sigma}, \boldsymbol{z})}{\partial \boldsymbol{z}} = \begin{bmatrix} \frac{\partial U^{(1)}}{\partial z_1} & \cdots & \frac{\partial U^{(1)}}{\partial z_L} \\ \vdots & \ddots & \vdots \\ \frac{\partial U^{(K)}}{\partial z_1} & \cdots & \frac{\partial U^{(K)}}{\partial z_L} \end{bmatrix}. \tag{4.16}$$

This can be written in the same form as the Jacobian with respect to conductivity (see equation (3.72))

$$\tilde{M}\frac{\partial \boldsymbol{\theta}}{\partial \sigma_i} = -[A^{-1}\tilde{M}^T]^T \frac{\partial A}{\partial z_i} A^{-1}\boldsymbol{f}. \tag{4.17}$$

The only difference compared to equation (3.72) is that here the differentiation $\partial A/\partial z_i$ is with respect to the contact impedance. This can be computed as [175]

$$\frac{\partial A}{\partial z_\ell} = \begin{bmatrix} C^\ell & D^\ell \\ D^{\ell T} & E^\ell \end{bmatrix}, \tag{4.18}$$

where the entries are given by

$$C^{\ell}_{i,j} = -\frac{1}{z_{\ell}^2}\int_{e_\ell}\phi_i\phi_j \mathrm{d}S \tag{4.19}$$
$$i,j = 1,2,\ldots,N,\ \forall\ \ell$$

$$D^{1}_{i,j} = \frac{1}{z_1^2}\int_{e_1}\phi_i \mathrm{d}S \tag{4.20}$$
$$i = 1,2,\ldots,N,\ j = 1,2,\ldots,L-1,\ \ell = 1$$

$$D^{\ell}_{i,j} = \begin{cases} -\frac{1}{z_{j+1}^2}\int_{e_{j+1}}\phi_i, & \ell = j+1 \\ 0, & \ell \neq j+1 \end{cases} \tag{4.21}$$
$$i = 1,2,\ldots,N,\ j = 1,2,\ldots,L-1,$$
$$\ell = 2,3,\ldots,L$$

$$E^{1}_{i,j} = -\frac{1}{z_1^2}\int_{e_1}(n_i)_1(n_j)_1 \mathrm{d}S = -\frac{|e_1|}{z_1^2} \tag{4.22}$$
$$i,j = 1,2,\ldots,L-1,\ \ell = 1$$

$$\begin{aligned} E^{\ell}_{i,j} &= -\frac{1}{z_\ell^2}\int_{e_\ell}(n_i)_\ell(n_j)_\ell \mathrm{d}S \\ &= \begin{cases} -\frac{|e_{j+1}|}{z_{j+1}^2}, & \ell = j+1 \\ \quad 0, & \ell \neq j+1, \end{cases} \end{aligned} \tag{4.23}$$
$$i,j = 1,2,\ldots,L-1,\ \ell = 2,3,\ldots,L.$$

4.3 Laboratory experiments

In this section, two series of laboratory experiments are presented. Both measurements were carried out in a cylindrical tank. In the first experiment the height of the tank was 100 mm and the diameter 70 mm. Equally spaced 16 stainless steel electrodes were attached to tank such that they were in the middle of the height of the tank. The height and width of the electrodes were 30 mm and 5 mm, respectively. In the second experiment the height of the tank was 70 mm and the diameter 280 mm. The FEM computations were carried out in 3D meshes having 3672 tetrahedral elements and 1108 nodes (first experiment) or 1086 tetrahedral elements and 396 nodes (second experiment). For the potential linear basis functions were used. Moreover, the conductivity was estimated in the same nodal basis. As a current injection method in the first experiment the reference protocol was used in which the electrode number 1 was chosen to be the reference electrode. In this case, the number of the current patterns was 15, and the voltages on all electrodes were measured against the same reference electrode. Hence the number of the measurements was 225. The injected current was 2 mA. The Oxford Brookes tomograph OxB ACT 4B that is a reduced version of the OxB ACT 4 system was used [43]. The measurement noise covariance matrix Γ_v was estimated based on a set of 500 repeated measurements. In the second experiment, the adjacent measurement protocol was used. In this case the number of the measurements was

256 and the injected current was 1 mA. The EIT-system developed at University of Kuopio was used [149].

4.3.1 First experiment

In the first experiment, the tank was filled with saline solution (tap water and Potassium chloride). Targets were not immersed in the tank. In the estimation it was assumed that the conductivity σ is homogeneous and contact impedances z_ℓ are equal on all the electrodes i.e. $\boldsymbol{z} = z_0(1, \ldots, 1)^T$. Therefore there were only two parameters to be estimated and the ML approach could be used. The experiment was carried out in order to study the effect of the initial guess, step size parameter and the measurement noise covariance matrix on the estimates and the convergence of the algorithm.

First, the error contour $\|\boldsymbol{V} - U(\sigma, z)\|^2$ was computed such that the conductivity σ varied from 4 $\Omega^{-1}\text{m}^{-1}$ to 11 $\Omega^{-1}\text{m}^{-1}$ and contact impedance z varied from 1×10^{-5} Ωm^2 to 1×10^{-3} Ωm^2. The error contour is shown in Figure 4.1. In order to study the performance of the method five different initial guesses were chosen. Three of these (Cases 1, 2, and 3) were used to study the effect of the initial guess. In these cases the measurement noise covariance was $\Gamma_v = I$. The Cases 4 and 5 were used to study the effect of the measurement noise covariance matrix and step size parameter, respectively. For all the cases the ML estimates were computed from equations (4.9) and (4.14). The algorithm was stopped when the error norm $\|\boldsymbol{V} - U(\sigma, z)\|^2$ reached the value of 2×10^{-5}. The results are shown in Figure 4.1 as blue (Case 1), red (Case 2), green (Case 3), yellow (Case 4), and black (Case 5) lines.

The error contour is seems to be elongated which is a typical feature of inverse problems, see Figure 4.1. This may cause problems for the convergence of the algorithm if the initial guess is chosen from the valley of the error surface. It can be seen that the algorithm converges to the same point from each of the different initial points (Cases 1, 2, and 3). These results are also summarized in Table 4.1.

When the estimated measurement noise covariance matrix is used in the estimation procedure the final result is different (Case 4). In this case the error is much smaller than in the case without the covariance matrix, see Table 4.1. This is due to implicit assumption of the noise covariance matrix (4.15). In the case in which $\Gamma_v = I$ it is implicitly assumed that variances of the measurements are equal and having the value of one. This assumption is unrealistically high which implies that the error estimates of the parameters are too large and unreliable. In the case of estimated measurement noise covariance matrix the errors of the parameters are more realistic.

The effect of the optimal step size parameter can be seen from Table 4.1. In the Cases 1, 2, and 3 in which the optimal step size parameters are used, the convergence is faster than in the case in which it is not used (Case 5, $\kappa_i = 0.5 \ \forall i$ and $\Gamma_v = I$). This is a well–known result from the literature [135]. There might also occur oscillation in the algorithm if the step size parameter is chosen too large, and this behavior is also discovered in this case. The measured (solid line) and computed voltages (dashed and dotted lines) for one current pattern is shown in

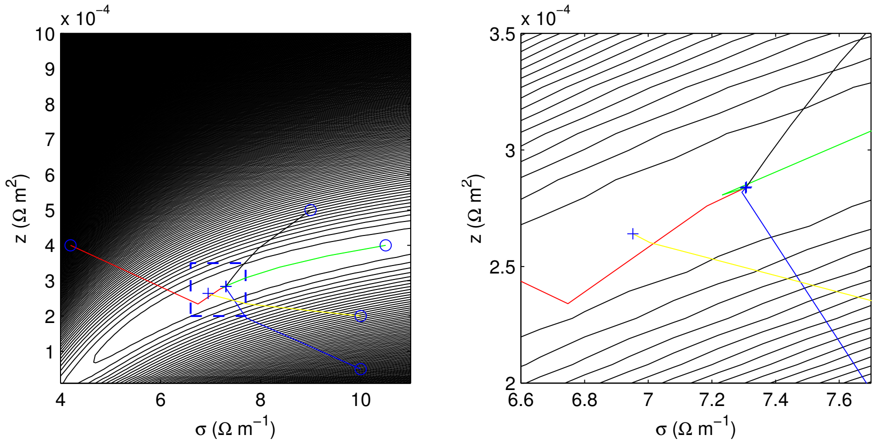

(a) Error contour

(b) Close-up view

Figure 4.1: (a) The error contour and convergence steps for 5 different cases. (b) The close-up view of rectangular area in a). The circles (o) and plus signs (+) denote the initial guesses and final estimates, respectively. The meaning of the colors are explained in the text, see Section 4.3.1.

Figure 4.2. The variation of the measured voltages might be due to environmental noise and/or the variation of the contact impedances. It can be seen that the computed voltages are smooth, due to the fact that the contact impedances in our model are modeled as a single parameter. Note that the noise level in the measurements is quite high (6 % in this case), so it is assumed that the main part of the variation is due to the measurement noise. It is also seen that the fits are almost the same with and without the noise covariance matrix as intuitively should be.

The square error norm of the measured and computed voltages $\|\boldsymbol{V} - U(\sigma, z)\|^2$ as a function of iteration number is shown in Figure 4.3. It can be seen from the figure, that the error norm of the voltage difference is almost zero after the third iteration step with each different initial point. A typical fit of the voltages is presented in Figure 4.2. Only in the case in which the optimal step size parameter is not used, convergence requires more than three iteration steps. This can be seen more clearly from Table 4.1.

4.3.2 Second experiment

In the second experiment, a tank was filled with tap water. In the tank a cylindrical plastic object, diameter of 52 mm, was located near the electrode number 1. A 20 Ω resistor was placed between the electrode number 13 and a current injection

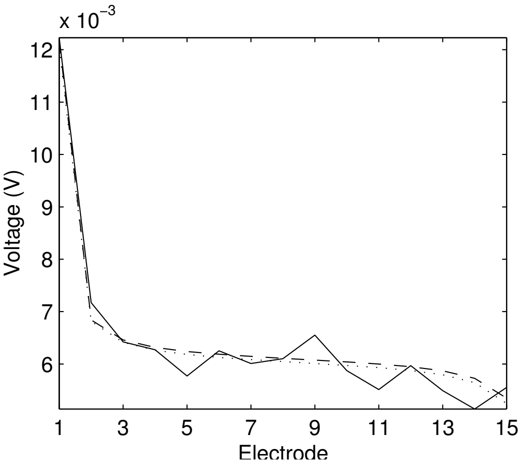

Figure 4.2: The boundary voltages for the 1st current injection. The solid line is the measured voltages, the dashed and dotted lines are the computed voltages with and without realistic noise covariance matrix, respectively.

Table 4.1: The results for cases 1–5. The units of the conductivity σ and contact impedances z_0 are $\Omega^{-1}\mathrm{m}^{-1}$ and $\Omega\mathrm{m}^2$, respectively.

	Initial point		Minimum		Errors		No. of steps
Case	σ	z_0	σ	z_0	$\Delta\sigma$	Δz_0	
1	10	0.00005	7.3	0.00028	22.5	0.01	3
2	4.2	0.0004	7.3	0.00028	22.5	0.01	3
3	10.5	0.0004	7.3	0.00028	22.5	0.01	3
4	10	0.0002	6.9	0.00026	0.2	0.002	3
5	9	0.0005	7.3	0.00028	22.5	0.01	5

unit. This resistor represents larger contact impedance on this electrode.

The reconstruction procedure consisted of two parts. First, the estimates for the homogeneous conductivity and all the contact impedances were computed by equations (4.9) and (4.14). The data for this part was collected from the tank without the plastic object. In the second part the object was placed in the tank and an estimate for the inhomogeneous 3D conductivity distribution was computed. To test the effects of the contact impedances, four different cases were reconstructed:

1. The values of the contact impedances for all the electrodes were four times the mean of the estimated contact impedances.

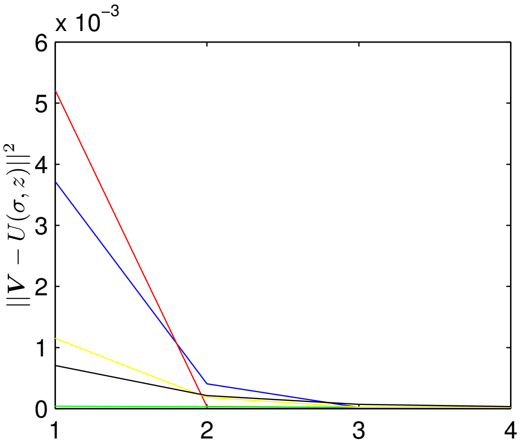

Figure 4.3: The error norm as a function of iteration number.

2. The measurements of the current carrying electrodes were removed. Hence the number of the measurements was 208 instead of 256. In this case the values of the contact impedances were the same as in the case 1.

3. In the first part the contact impedances on all the electrodes were estimated as a single parameter and was used as value of the contact impedances in the estimation of the conductivity distribution.

4. The contact impedances on all the electrodes were fixed to the value obtained in the first part of the estimation procedure.

The estimated homogeneous conductivity value was used as an initial guess of an iterative reconstruction. The reconstruction was computed by equations (4.9) and (4.10). It is assumed that σ^* is zero. In this case the equation (4.10) is of the form

$$\delta\boldsymbol{\sigma}_i = \left[J_i^T J_i + \alpha L^T L\right]^{-1} \left[J_i^T (V - U(\boldsymbol{\sigma}_i)) - \alpha L^T L \boldsymbol{\sigma}_i\right]. \tag{4.24}$$

In the reconstruction an anisotropic smoothness prior presented in Section 3.3.2 was used. In this case there are three different regularization parameters, namely parameters with respect to radius (α_r), angle (α_θ) and height (α_z). These parameters were $\alpha_r = 4.5 \cdot 10^{-4}$, $\alpha_\theta = 4.5 \cdot 10^{-4}$ and $\alpha_z = 4.5 \cdot 10^{-3}$, respectively and they were adjusted by visual examination.

The results of the reconstructions are shown in Figure 4.4. When the incorrect value for the contact impedances was used it can be seen that the presence of the object cannot be clearly identified, see Figure 4.4(a). Also high conductive ring can be seen near the boundary. This is due to the incorrect value of contact impedance. In the algorithm the effect of the incorrect value of contact impedance is compensated by changing the conductivity of the domain. It can be seen that this effect is large. Also the presence of the resistor on the electrode number 13 can be seen. Similar results were stated in [103] in which trigonometric current pattern was used in reconstruction with simulated data. Also in [79], it was stated that the conductivity distribution at the outer layer is sensitive to the estimated conductivity values. It can be seen from the Figure 4.4(b) that if the measurements from current-carrying electrodes are removed the effect of the incorrect value of the contact impedances disappears. The presence and location of the object can be clearly identified and its location is correct. This verify the claim that the four-electrode measurement removes almost entirely the effect of the contact impedance. The result of the case 3 in which only one parameter for the electrode contact impedances is used is shown in Figure 4.4(c). It can be seen that one parameter cannot explain the variation of the contact impedance from electrode to electrode. Hence a resistive area near the electrode number 13 can be seen due to the additional resistor. The presence and the location of the object however is also clearly seen. Finally, if the contact impedances on all the electrodes are estimated simultaneously the problem of the variation of the contact impedances is overcome and the reconstruction is substantially better, see Figure 4.4(d). The values of the contact impedances as a function of iteration number are shown in Figure 4.5. It can be seen that the value of the contact impedance of the electrode number 13 is bigger than the other ones, as it should be due to the additional resistor.

4.4 Summary

The applicability of contact-impedance estimation in two laboratory experiments was studied. The performance of the method was shown to be reliable and that the method can be applied for contact impedance estimation with real data in a laboratory environment.

If contact impedance is modeled as a single parameter, it was found that this approach substantially improves image reconstruction but it was considered that still further improvement can be achieved by modeling each electrode contact impedance separately. It is also found that the results of the 4-electrode data collection method without electrode contact impedance estimation and 2-electrode data collection method with electrode contact impedance estimation are essentially similar. On the other hand, for example in the case of an optimal current patterns the effect of the contact impedances is remarkable and these values have to be estimated.

It was also assumed that the liquid was purely conductive and the contact impedance was real valued. In some practical applications this assumption may not be valid and it is preferable to estimate impedivity of the object and the complex-valued contact impedances as presented in [175].

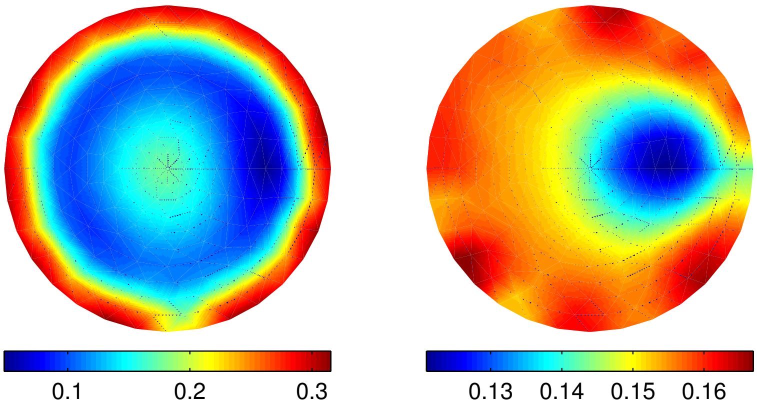

(a) case 1. (b) case 2.

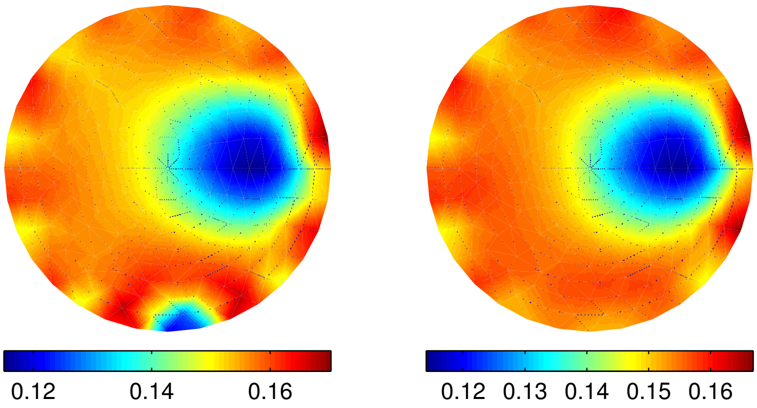

(c) case 3. (d) case 4.

Figure 4.4: The results of the second experiment. (a) The incorrect contact impedances. (b) The 4-electrode data collection method. (c) The contact impedances as a single parameter. (d) The 16 estimated contact impedances. The unit of conductivity is $(\Omega\text{m})^{-1}$. The electrode number 13 is located on the bottom of the illustration.

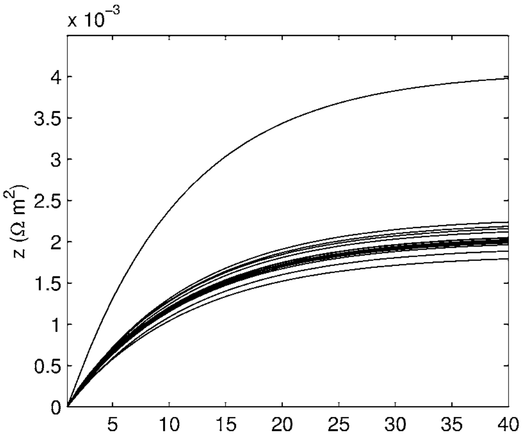

Figure 4.5: The contact impedances as a function of the iteration number.

CHAPTER V

Internal structures

5.1 Introduction

In many practical situations there are fixed structures inside the process equipments. These structures can be, for example, an impeller drive shaft or a mixing paddle [120]. Since the estimated image in EIT represents the resistivity distribution of the interior, especially the conductive internal structures may cause difficulties in the reconstruction. If the poorly-conducting region is near the conductive structure causing high contrast, the masking effect of the structure may be substantial. In article [189] it was reported that the metal impeller drive shaft causes a discontinuity in the resistivity profile which leads to underestimated resistivity values in the central area of the reconstructed image. The presence of this type of structure can be taken into account for example by a certain current excitation scheme as shown in [116].

Earlier results show that by taking into account the presence of the stirrer it will not disturb the image reconstruction. The disruption of the stirrer was removed technically by using the stirrer as an electrode [116]. This issue is discussed in more detail in the next chapter. Another approach to overcome the conductive structure problem is mathematical. If the location and possibly the resistivity of the structure are known, this information can be taken into account in the estimation. The location of the internal structure can be included in the mesh that is used in the estimation and the edges of the structure as well as the resistivity value can be considered in the regularization of the solution. In this chapter an estimation approach in which the prior information of the locations and resistivities of the internal structures are taken into account is proposed.

5.2 Prior models for known structures and resistivities

Known resistivities and locations of the internal structures can be taken into account in the estimation by constructing the prior density wisely. The prior density can be divided in two separate parts, which are

$$\pi_1(\boldsymbol{\rho}) = \exp(-\alpha\|\widetilde{L}(\boldsymbol{\rho}-\boldsymbol{\rho}^*)\|^2) \tag{5.1}$$

$$\pi_2(\boldsymbol{\rho}) = \exp(-\beta\|D(\boldsymbol{\rho}-\boldsymbol{\rho}^*)\|^2), \tag{5.2}$$

where vector $\boldsymbol{\rho}^*$ contain the known resistivity values of the structure. If the value of some element is not known, the value is set to zero. The matrices $\widetilde{L}$ and D are introduced shortly. Since the matrices $\widetilde{L}$ and D are independent and they operate to the same vector, the final prior density can be written in the form

$$\pi(\boldsymbol{\rho}) \propto \exp\left(-\frac{1}{2}(\boldsymbol{\rho}-\boldsymbol{\rho}^*)^T\Gamma_{\mathrm{pr}}^{-1}(\boldsymbol{\rho}-\boldsymbol{\rho}^*)\right), \tag{5.3}$$

where the covariance matrix is

$$\Gamma_{\mathrm{pr}}^{-1} = 2\alpha\widetilde{L}^T\widetilde{L} + 2\beta D^T D. \tag{5.4}$$

The new difference matrix $\widetilde{L}$ is obtained from L by removing the -1's that correspond to the element edges that connect the known internal structures to the surrounding. See the construction of the traditional difference matrix from the page 48. Also the number 3 is replaced by 2 in the same row in the cases where the corresponding element has one edge that connects the internal structure to the background, see Figure 5.1(b). Also the rows corresponding to the elements inside the structure are set to zero. Another part of the prior density draws the resistivity values ρ_k that correspond to the known internal structures towards the known value $\boldsymbol{\rho}^*$. This is accomplished by the matrix D which picks out the correct parameters from the parameter vector. It is constructed so that if the k^{th} resistivity value is assumed to be known, in D there will be a row of zeros having 1 at the k^{th} column. The matrix D includes as many rows as known (assumed) resistivity values exist. The value of the regularization parameter β can be large which means that the variances of the resistivity values of the internal structures are assumed to be small.

5.3 Numerical simulations

In this section, results of numerical simulations corresponding to the measurement situations in which one have *a priori* known internal structures in the object to be imaged are shown. Two different cases are studied. In the first one, a conductor is within the circular domain and the aim is to reconstruct a poorly conducting region, connected to the conductor, in the center of the domain, see Figures 5.2(a) and 5.3(a). This simulates air-core imaging of the mixing vessel with metallic paddle. In the second one connected, conductive structures is within the domain enclosing the poorly conducting region. This situation is illustrated in Figures 5.2(b) and 5.3(b). Results from forward computations to simulate the effect of the connected highly conductive structures on the potential distribution are also shown.

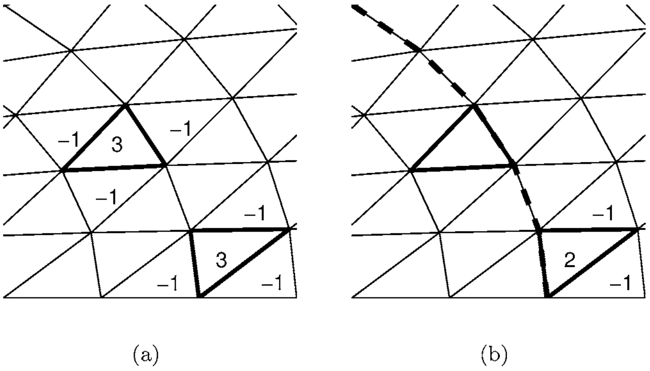

Figure 5.1: The schematic representation of the construction of the difference matrix in a) traditional case and in b) "internal structure" case . The dashed line represents the boundary of the internal structure. Compare this figure with Figure 3.7.

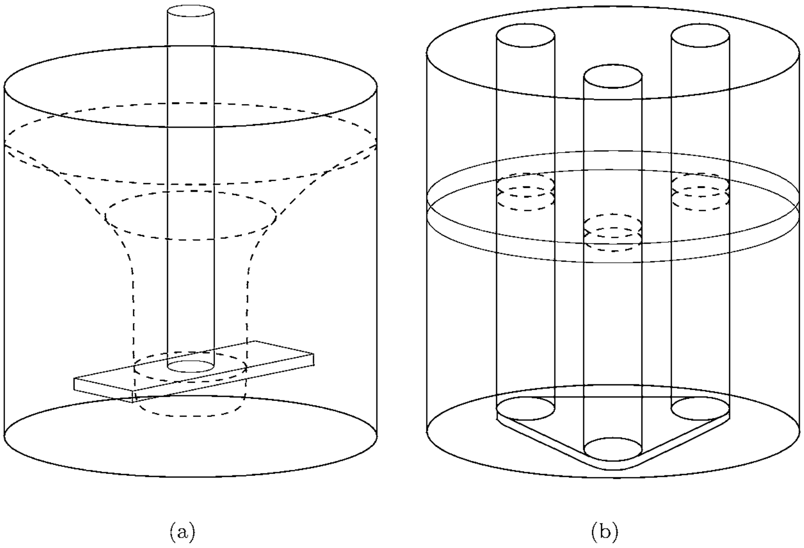

Figure 5.2: The real 3D-situations. (a) Air-core imaging and (b) three-rods inside the tank.

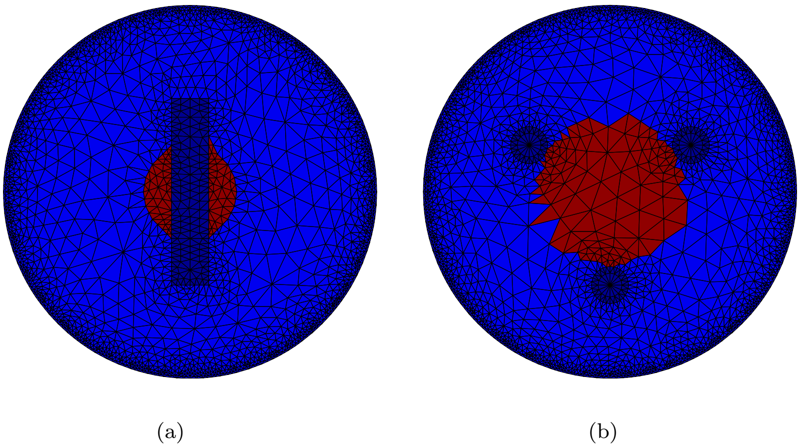

Figure 5.3: The meshes for the forward calculations. (a) For the air-core imaging and (b) for the connected conductive structures. The resistivity of the background is 400 Ωcm (blue), of the known internal structures 4 Ωcm (dark blue) and of the air 4000 Ωcm (red).

All the simulations are carried out in two-dimensions. The computational domain has the radius of 14 cm and 16 electrodes, width of 2.5 cm, are attached on the boundary. The covering ratio of the electrodes is 0.45. The meshes that were used in the forward computations are shown in Figure 5.3. The mesh in Figure 5.3(a) that was used for the first simulation includes 4208 elements and 2217 nodes and the mesh in Figure 5.3(b) for the second simulation consists of 4176 elements and 2201 nodes. The meshes were fairly dense in order to obtain accurate voltage values on the electrodes. These were dense especially near the boundary due to the large gradients in the potential distribution near the electrodes. The potential distribution u was approximated with the first-order basis functions which means that the approximation of the solution is piecewise linear. The estimates of the parameters $\{\rho_k\}$ were computed on a coarser mesh such that the piecewise constant basis $\{\chi_k\}$ was used. The estimated resistivity distribution was mapped from the coarse mesh to the dense mesh for the forward computations in each iteration. In the first case the number of parameters was 848 and in the second case it was 765. The meshes were generated with the QMG-package [1]. In the simulations the trigonometric current pattern (3.89) was used.

In all the simulated electrode voltages two different types of noise were added. One was Gaussian, zero mean random noise having the variance of 1 % of the voltage range and the other one was zero mean Gaussian noise having the variance of 0.1 % of each voltage value. The first one represents noise that is common for every electrode which can be, for example, induced from the measurement environment. The second represents the error in the voltage measurements. The contact impedances z_ℓ were assumed to be known *a priori* and in both cases $z_\ell = 0.05$ for all ℓ.

Estimated images are solved using Gauss-Newton method (3.79) with traditional smootheness prior ("general approach") and with proposed prior ("prior information approach") in which the prior information of the structures is taken into account. Gauss-Newton iteration can be written in the form

$$\boldsymbol{\rho}_{i+1} = \boldsymbol{\rho}_i + \left[J_i^T J_i + \Gamma_{\text{pr}}^{-1}\right]^{-1} \left[J_i^T(\boldsymbol{V} - U(\boldsymbol{\rho})) + \Gamma_{\text{pr}}^{-1}(\boldsymbol{\rho}_i - \boldsymbol{\rho}^*)\right], \tag{5.5}$$

where the Jacobian is computed according to equation (3.68). Note that it is assumed here that the measurement noise covariance matrix is I. The prior covariance matrix in "general approach" is

$$\Gamma_{\text{pr}}^{-1} = 2\alpha L^T L \tag{5.6}$$

and in "prior information approach" as shown in equation (5.4).

5.3.1 Air-core imaging of the mixing vessel

Consider a situation shown in Figures 5.2(a) and 5.3(a). In this case detecting a poorly conducting region, air-core, in the center of the mixing vessel when disturbing internal structure is present is of interest. The background resistivity of the domain was $4 \cdot 10^2 \Omega$cm, the resistivity of the region of interest (air-core) in the center was $4 \cdot 10^3 \Omega$cm and the resistivity of the paddle was 4 Ωcm. Ten simulated voltage data sets for the object with and without a poorly conducting region in the center were computed and random noise in the simulated voltages as explained earlier were added. In the estimation with the general and the prior information approaches the regularisation parameter $\alpha = 0.5$ and the regularisation parameter $\beta = 2$ in the prior information approach. These parameters were chosen *a posteriori* by visual examination.

General approach

An example of a reconstruction without the air-core inside the vessel is shown in Figure 5.5(a) and a reconstruction of the domain with the air-core around the mixing paddle is shown in Figure 5.5(c). The cross-sectional values (averaged over 10 simulations) along the blue line shown both in Figure 5.5(a) and Figure 5.5(c) are plotted in Figure 5.5(e). The true resistivity distribution is shown in Figure 5.3(a).

Figure 5.5(a) reveals the effect of the mixing paddle. When the presence of the paddle is not taken into account in the reconstruction, it tends to make a fairly large poorly resistive region in the center of the image. In addition, the truly homogeneous background is non-homogeneous in the reconstruction. It can be seen from Figures 5.5(c) and 5.5(e) that there is a slight increase in the estimated resistivity values that may be due to the presence of the air-core. However, the increase is very small and in addition the location is wrong due to the disturbing effect of the highly conductive paddle.

Prior information approach

The results from the same situation but the reconstruction is made by taking into account the presence of the mixing paddle are shown in Figures 5.5(b), 5.5(d) and 5.5(f). The reconstructions without and with the air-core are show in Figures Figure 5.5(b) and 5.5(d), respectively. The cross-sectional values are shown in Figure 5.5(f). Figures 5.5(b) and 5.5(f) show that when the air-core is absent the background in the image is fairly uniform due to the increased prior information in the reconstruction. When the air-core is present, it is well detected which can be seen in Figure 5.5(d) and in the cross-sectional values shown in Figure 5.5(f). The boundary of the air core can not be detected accurately. This is due to the fact that the smoothness assumption in the domain $\Omega \setminus W$ has been used. The W is the domain of the internal structure.

Posterior covariance

The posterior covariance matrix

$$\Gamma_{\mathrm{post}} = [J^T J + 2\alpha \widetilde{L}^T \widetilde{L} + 2\beta D^T D]^{-1}, \tag{5.7}$$

corresponding the last iteration was also computed for the air-core imaging case. The covariances between three chosen elements and the remaining ones (i.e. corresponding rows) are shown in Figure 5.6. Elements are chosen such that the element # 104 (5.6(a)) is connected to the structure, the element # 500 (5.6(b)) is far from the structure and the element # 788 (5.6(c)) is inside the structure, see Figure 5.4. Also, the variances of the parameters (i.e., diagonal elements of the posterior covariance matrix) are shown in Figure 5.6(d). Corresponding correlation matrix (2.35) is also computed the studying of correlations between the parameters quantitatively. The correlations for chosen elements and the elements having common edge with those elements are given in Table 5.1. The element # 104 is connected to the structures such that one neighbour element is inside the structure. Sharp edge in the covariance between the elements outside and inside the structure therefore can be seen in Figure 5.6(a). Moreover the correlations between the element # 104 and the neighbouring elements outside the structure are close to one, whereas the correlation between the element inside the structure is close to zero, see Table 5.1. The covariance between the element # 500, which is far from structure, and neighbouring elements is circular shaped. The correlations between the element # 500 and the neighbouring elements shown in Table 5.1 are close to one. This means that these parameters can not be estimated independently. On the basis of the correlation matrix, spatial resolution can be, in principle, approximated. In this case it is about 10 % of the diameter of the domain. Note that the resolution depends on the choice of the prior. The covariance between the element # 788, which is inside the structure, and neighbouring elements are essentially zero, see

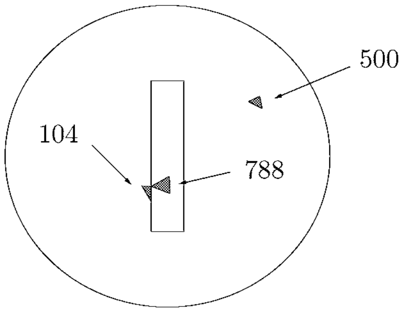

Figure 5.4: The locations of the chosen parameters in the domain.

Table 5.1: The correlations for three nearest elements for the parameters # 104, # 500 and # 788.

# 104	# 500	# 788
0.963	0.887	$-0.750 \cdot 10^{-5}$
0.973	0.903	$-0.640 \cdot 10^{-5}$
-0.002	0.902	$-0.350 \cdot 10^{-5}$

Figure 5.6(c). This can also be seen from the Table 5.1. This is due to the fact that correlation is not assumed between the elements inside the structure in the construction of the matrix $\widetilde{L}$, see Figure 5.1(b). It can be seen from Figure 5.6(d), that the variance of the parameters is bigger close to the structure. This feature of the EIT is known from literature, see e.g. [41]

5.3.2 Connected conductive structures

Here three different cases were studied using the geometry shown in Figures 5.2(b) and 5.3(b). These are:

1. Separate rods, high conductivity (conductors)
2. Connected rods, high conductivity (conductors)
3. Separate rods, low conductivity (insulators)

In all the cases detecting a poorly conducting region in the center of the domain is of interest. The background resistivity of the domain was $4 \cdot 10^2\Omega$cm, the resistivity of the region of interest in the center was $4 \cdot 10^3\Omega$cm and the resistivity of the rods was either 4 Ωcm (Cases 1 and 2) or $4 \cdot 10^5\Omega$cm (Case 3). In the general approach reconstructions, the regularization parameter was $\alpha = 0.05$ and in the prior information approach the regularization parameters were $\alpha = 0.1$ and $\beta = 2$. These parameters were chosen *a posteriori* by visual examination.

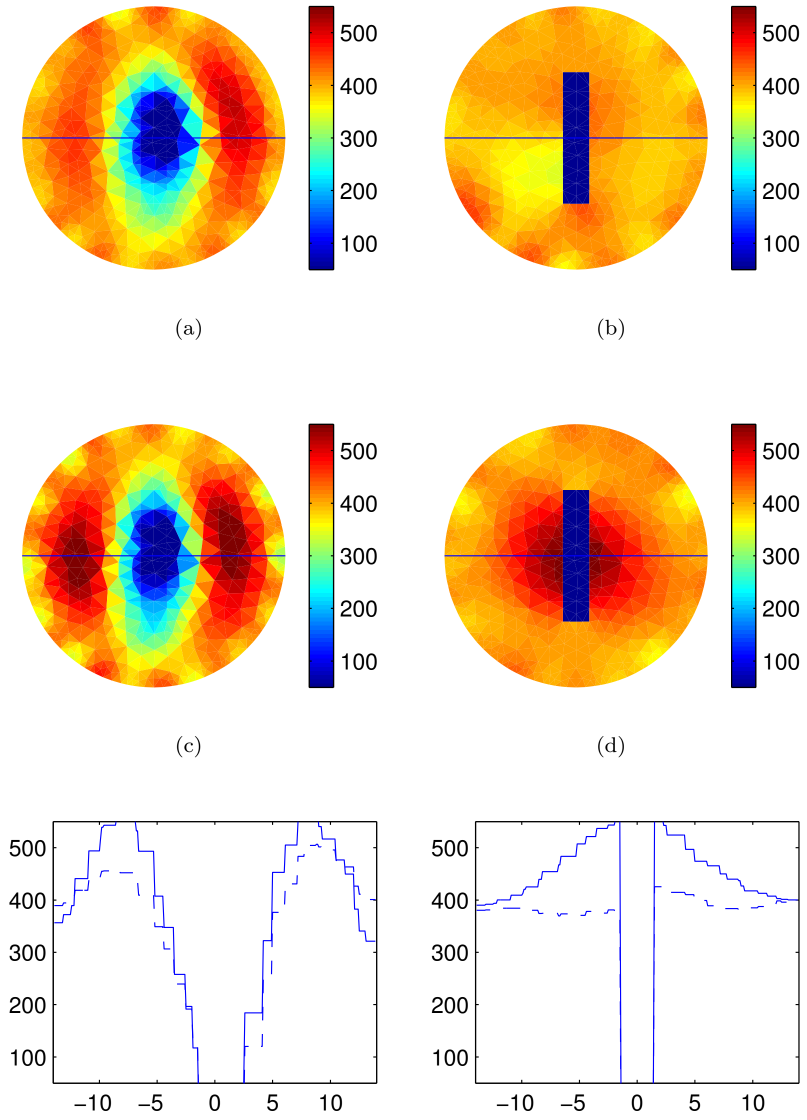

(a) (b)

(c) (d)

(e) (f)

Figure 5.5: The air-core imaging simulations. Images (a), (c) and (e) were reconstructed with the general approach and (b), (d) and (f) with the prior information approach. In (a) and (b) there is only the conductive paddle in the domain and in (c) and (d) the air-core is present. The cross-sectional values averaged over 10 simulations (blue lines in the reconstructed images) are plotted in (e) and (f). The dashed lines are for the “empty domain” cases (no air-core, (a) and (b)) and the solid lines for the air-core cases ((c) and (d)).

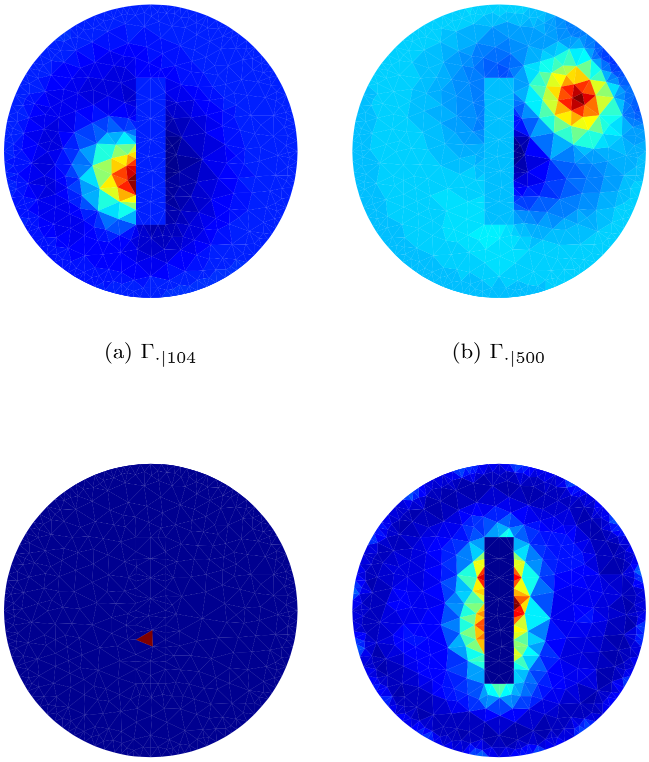

(a) $\Gamma_{\cdot|104}$ (b) $\Gamma_{\cdot|500}$

(c) $\Gamma_{\cdot|788}$ (d) σ_{ρ}^{2}

Figure 5.6: The posterior covariance for three chosen elements (a), (b) and (c). (d) The diagonal elements of covariance matrix, i.e. the variances of the parameters.

The simulations of the potential distribution for the cases of conductive internal structures (Cases 1 and 2) are shown. Simulated potential distributions of the trigonometric current pattern I_1^{tri} are shown in Figure 5.7 as equipotential contour plots. The potential distributions for the Cases 1 and 2 are shown in Figures 5.7(a) and 5.7(b), respectively.

Forward problem simulations

Since all computations are carried out in 2D, computational problem arise in case 2. The rods shown in the Figure 5.2(b) are conductors having very high conductivity and since they are electrically connected on the bottom of the tank, they will be in the same electric potential. From the computation point of view this means that they are connected together outside the two-dimensional computational domain. In 2D finite element computations this type of situation can be simulated by forcing the potential to be the same in the nodes that correspond to the rods inside the object. This can be accomplished by making the following modification for the previous FEM equations presented in Chapter 3.

Let $W \subset \Omega$ be a subdomain including all the highly conductive structures that are connected together. Define

$$\alpha = G\gamma, \tag{5.8}$$

where $G \in \mathbb{R}^{N\times(N-p+1)}$ and $\gamma = (\gamma_1, \ldots, \gamma_{N-p}, \gamma_W)^T \in \mathbb{R}^{(N-p+1)\times 1}$, where p is the number of nodes in the subdomain $W \subset \Omega$ and γ_W is the value of the potential in W. The matrix G is a sparse matrix that includes ones in the specific locations such that it maps the potential value γ_W to the correct node locations in α. After substituting the formula (5.8) to the matrix equation (3.34), the following matrix equation is obtained

$$\widetilde{A}\widetilde{\theta} = \widetilde{f}, \tag{5.9}$$

where

$$\widetilde{A} = \begin{bmatrix} G^T(B(\sigma) + C(z))G & G^T D(z)\mathcal{C} \\ \mathcal{C}^T D(z)^T G & \mathcal{C}^T E(z)\mathcal{C} \end{bmatrix}, \tag{5.10}$$

and

$$\widetilde{\theta} = \begin{bmatrix} \gamma \\ \beta \end{bmatrix}, \quad \widetilde{f} = \begin{bmatrix} G^T\mathbf{0} \\ \mathcal{C}^T I \end{bmatrix}. \tag{5.11}$$

The parameter $\widetilde{\theta}$ can be solved as

$$\widetilde{\theta} = \widetilde{A}^{-1}\widetilde{f}. \tag{5.12}$$

Three distinct features can be seen in the potential distributions. First, the potential is constant in the subdomain occupied by the conductors. Second, due to the complete electrode model the potential is almost constant under the electrodes. This shunting effect was also studied in Chapter 3. The third feature is that when the rods are connected and are in the same potential, only a small amount of current will flow in the center of the domain (large gap between the equipotential lines). This makes it very difficult to reconstruct centrally located objects in the domain due to the decreased sensitivity in the center.

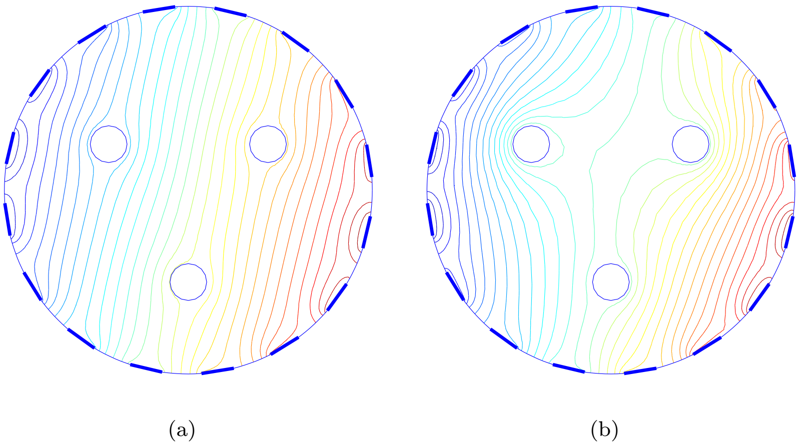

Figure 5.7: The potential distributions of the first trigonometric current pattern I_1^{tri} for (a) separate and (b) connected rods.

CASE 1: SEPARATE RODS, HIGH CONDUCTIVITY

General approach

Ten simulated voltage data sets for the object with and without a poorly conducting region in the center were computed and random noise in the simulated voltages as explained earlier was added. The reconstructions were first computed using the general approach without taking into account the presence of the rods.

A result from one of the reconstructions without a poorly conducting region at the center and with the poorly conducting region are shown in Figures 5.8(a) and 5.8(c), respectively. The rods are faintly seen in Figure 5.8(a) which is partly because the images in Figures 5.8(a) – 5.8(d) are in the same color scale. The poorly conducting region is seen to be easily detected. The cross-sectional values (averaged over 10 simulations) along the blue line shown in Figure 5.8(a) and 5.8(c) are plotted in Figure 5.8(e). It can be seen that the poorly conducting region is well detected (solid line) but in the “empty domain” case (only the rods are in the domain) the average resistivity value is slightly too small (dashed line). The explanation for this is that the highly conductive rods tend to draw the solution towards smaller resistivity. If the rods were larger, the error would be bigger.

Prior information approach

The results of the same situation but reconstructed by taking into account the presence and resistivity of the rods are shown in Figure 5.8. It can be seen that in the “empty domain” case the background resistivity is slightly more homogeneous and the poorly conducting rods do not affect the resistivity estimate (dashed line in Figure 5.8(f)) as much as in the general approach. The poorly conducting region is slightly better detected (higher resistivity) than by using the traditional approach. The rods are seen in the correct places in both cases since they were taken into account in the reconstruction.

Case 2: Connected rods, high conductivity

If the highly conductive rods are electrically connected together, reconstruction of the poorly conducting region in the center of the object becomes impossible. This can be seen in Figure 5.9. The explanation for this is that due to the high conductivity, only a small amount of current flows to the center of the object which makes the sensitivity very low in that region (see also the simulated potential distributions in Figure 5.7). Even if the presence of the rods is taken into account, the poorly conducting region cannot be detected, see Figure 5.9(f).

The difficulty of detecting an inhomogeneity in the center of the domain can be understood if the differences in the measured voltages between the “empty domain” U_E (only the rods inside) and U_F, the voltages with the poorly conducting region in the center are computed, that is

$$\text{Difference} = \frac{\|U_E - U_F\|}{\|U_E\|} \cdot 100\% \ . \tag{5.13}$$

In the case 1 (separate rods) the difference is 20.2 % and in the case 2 it is 0.0064 %. It is very difficult to reconstruct the poorly conducting region if the voltage difference is this small.

Case 3: Separate rods, low conductivity

If there are structures such as large metallic paddles in the pipe or vessel, they may disturb the reconstruction severely as was shown in Case 2. One possible solution for this type of a case could be to make the internal structures non-conducting. The Case 1 was recomputed with rods that have high resistivity $\rho = 4 \cdot 10^3 \Omega\text{cm}$. The results are shown in Figure 5.10.

General approach

If the rods are not taken into account in the estimation they can be seen in the reconstructed image in the “empty domain” case Figure 5.10(a). However, since the rods have high resistivity they tend to increase the estimated resistivity of the background, especially in the center. This is seen in the cross sectional line plot in Figure 5.10(e) (dashed line). The poorly conducting region in the center is well detected, similarly as in the Case 1.

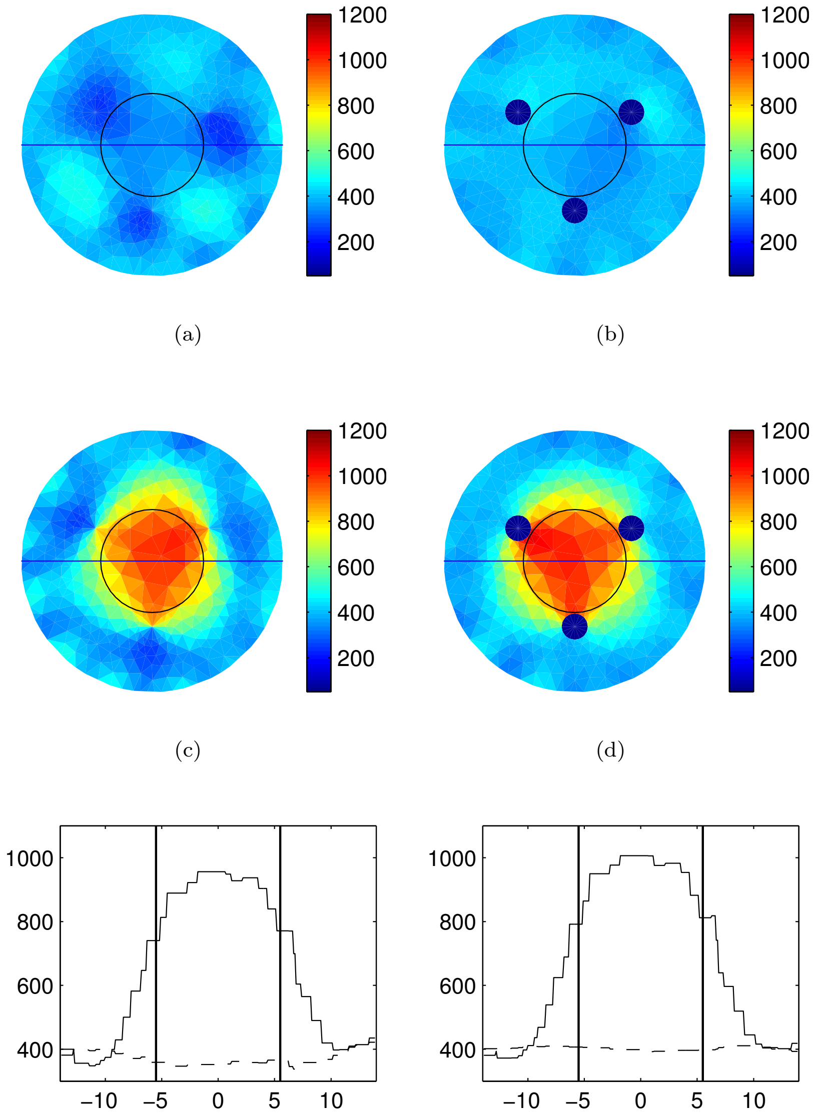

(a) (b) (c) (d) (e) (f)

Figure 5.8: Results for the Case 1. The vertical lines in (e) and (f) show the true width of the inhomogeneity (the diameter of the circle in the reconstructed images). Images (a), (c) and (e) were reconstructed with the general approach and (b), (d) and (f) with the prior information approach. In (a) and (b) there are only the rods in the domain and in (c) and (d) the air-core is present. The cross-sectional values averaged over 10 simulations (blue lines in the reconstructed images) are plotted in (e) and (f). The dashed lines are for the “empty domain” cases (no air-core, (a) and (b)) and the solid lines for the air-core cases ((c) and (d)).

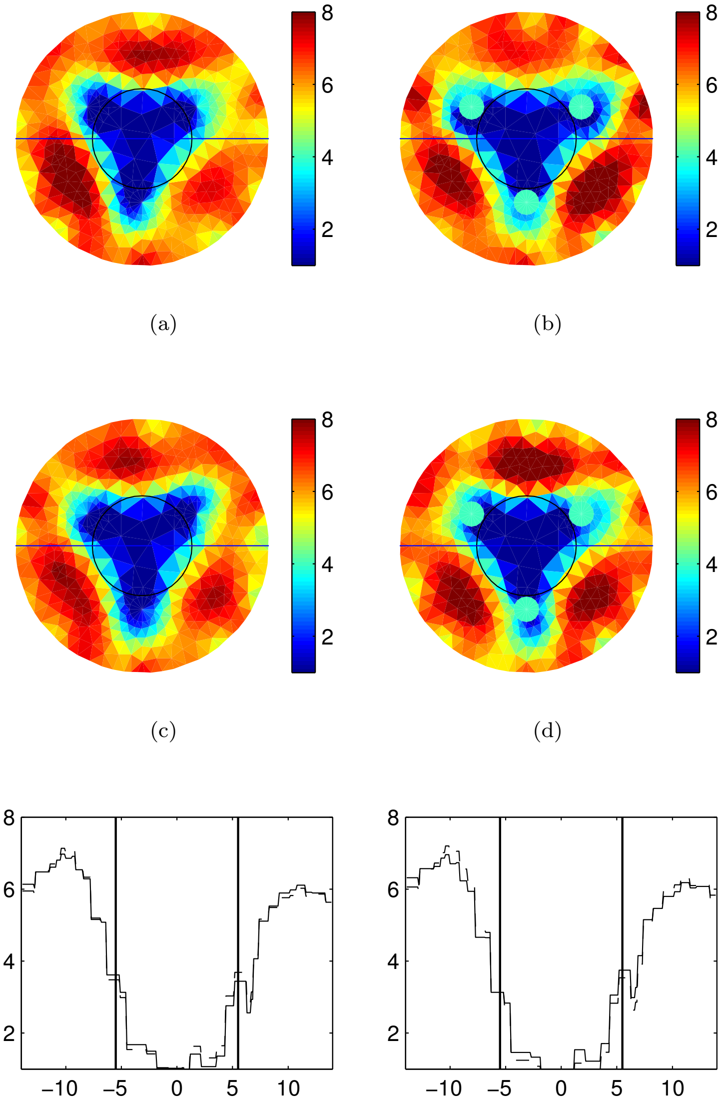

(a) (b)

(c) (d)

(e) (f)

Figure 5.9: Results for the Case 2. The vertical lines in (e) and (f) show the true width of the inhomogeneity (the diameter of the circle in the reconstructed images). Images (a), (c) and (e) were reconstructed with the general approach and (b), (d) and (f) with the prior information approach. In (a) and (b) there are only the rods in the domain and in (c) and (d) the air-core is present. The cross-sectional values averaged over 10 simulations (blue lines in the reconstructed images) are plotted in (e) and (f). The dashed lines are for the "empty domain" cases (no air-core, (a) and (b)) and the solid lines for the air-core cases ((c) and (d)).

Prior information approach

Taking into account the rods, the reconstructed resistivity distribution in the "empty domain" case becomes more homogeneous and the estimated value is almost exactly correct across the whole domain. The poorly conducting region can also be well detected.

It might look as if the general reconstruction would be better in detecting the poorly conducting region in the center since the maximum value of the resistivity in the center (approximately 1300 Ωcm in Figure 5.10(e), solid line) is nearer to the correct value (4000 Ωcm) than the estimate obtained with the prior information approach in Figure 5.10(f) (approximately 1100 Ωcm). However, the increase in the reconstructed value in Figure 5.10(e) is mainly due to the insulating rods in the object which makes the estimates to increase in the center (see the dashed line in the "empty domain" case in Figure 5.10(e)).

The difference of 25.9 % in the electrode voltages is slightly bigger than in the Case 1 in which the rods were highly conductive.

5.4 Summary

In this chapter, the effects of conducting internal structures on the reconstructed images were studied. An approach for taking into account the presence of internal structures was presented. In the simulations, it was concentrated on the case of detecting a poorly conducting region in the center of circular domain.

Numerical two-dimensional simulations showed that *a priori* information can in certain cases improve the reconstructions significantly. It was shown that, for example, the mixing paddle may disturb the reconstruction obtained by the general approach so much that centrally located air-core cannot be detected. With the prior information approach the presence of the paddle can be taken into account and the air-core can be fairly well detected.

In another simulation in which there were electrically separated conductors (rods) in the tank it was found that they do not much affect on the reconstruction and the centrally located inhomogeneity can be well detected with both reconstruction approaches. The prior information, locations and resistivity of the rods slightly improved the reconstructions. An artifact that was seen in the general approach (tendency to underestimate the resistivity) could be removed by taking into account the presence of the rods.

If the rods were electrically connected the centrally located inhomogeneity could not be detected and the prior information did not help in this case. The reason for this is the very low sensitivity in the center of the domain due to the shunting effect of the connected rods. Poor results in the connected rods –case could be overcome by making the rods non-conducting. In this case, the poorly conducting region in the center could be well detected with both approaches. The use of prior information removed the tendency of the general approach to overestimate the resistivities in the reconstruction that was due to the presence of

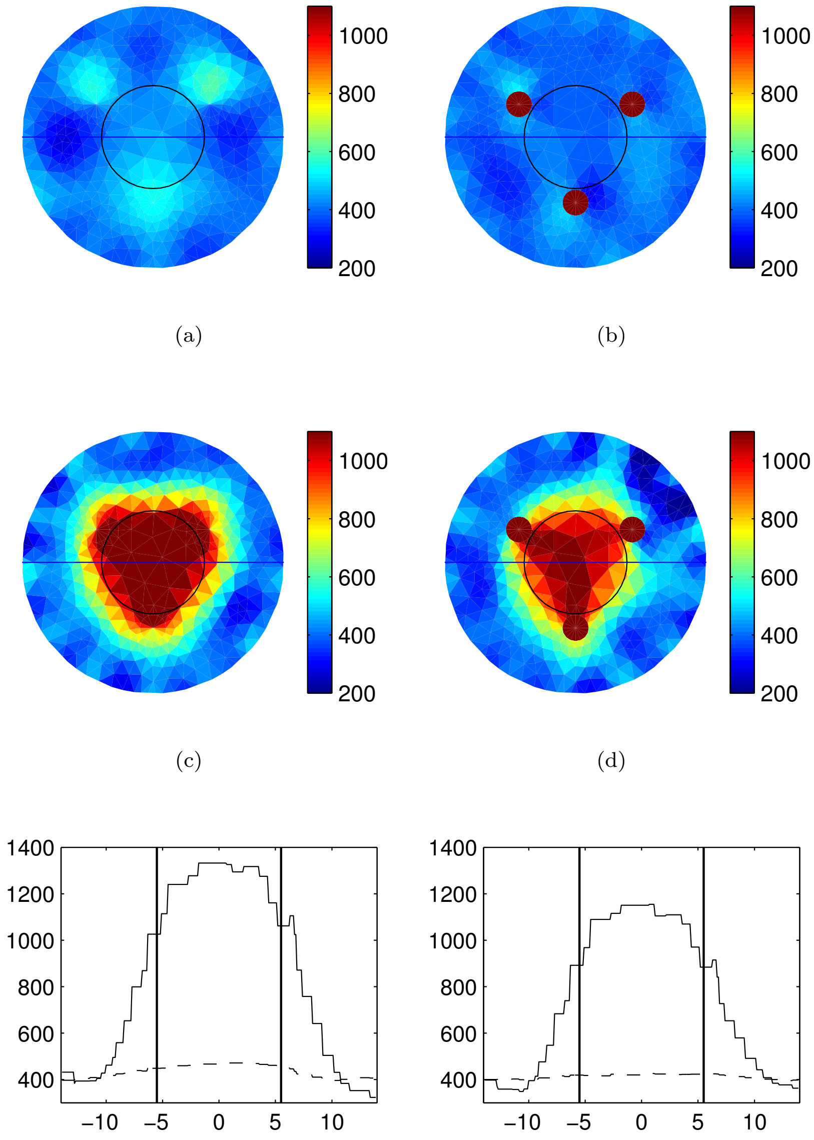

(a) (b)

(c) (d)

(e) (f)

Figure 5.10: Results for the Case 3. The vertical lines in (e) and (f) show the true width of the inhomogeneity (the diameter of the circle in the reconstructed images). Images (a), (c) and (e) were reconstructed with the general approach and (b), (d) and (f) with the prior information approach. In (a) and (b) there are only the rods in the domain and in (c) and (d) the air-core is present. The cross-sectional values averaged over 10 simulations (blue lines in the reconstructed images) are plotted in (e) and (f). The dashed lines are for the “empty domain” cases (no air-core, (a) and (b)) and the solid lines for the air-core cases ((c) and (d)).

the rods.

As a conclusion it can be said that if there are known internal structures in the object they should be taken into account in the reconstruction. Especially, if the structures are large, they tend to draw the estimated resistivities towards the resistivity value of the structure and in the worst case, prevent the interesting region to be reconstructed reliably. This tendency can be avoided by taking into account the structures by the reconstruction approach proposed in this chapter. If the internal structures form a poorly resistive path for the current to flow, it is recommendable to “cut” these paths or insulate the internal structures.

CHAPTER VI

Internal electrodes

6.1 Introduction

The sensitivity of EIT depends on the current density inside the object. In the areas where the current density is low the resistivity changes may not cause detectable changes on the measured voltages on the electrodes. In classical EIT one uses only the electrodes attached on the surface of the object and thus, the current density in the center of the object is quite low and the sensitivity is poor. In many cases there are *a priori* known internal structures near the center of the vessels which could be used as internal electrodes. By injecting currents through the internal electrode the current density and hence the sensitivity near the center of the vessel can be increased. Further, the internal electrodes produce more data which improves the image reconstruction.

The use of an internal reference electrode in EIT for medical purposes was studied in [53]. In that study it was shown that the use of the internal electrode significantly improves the resolution of EIT. In [116], the effects of internal electrodes to the sensitivity of EIT were studied by numerical simulations. On the basis of these simulations it can be said that the additional internal electrodes increase the quality of the reconstructed images. EIT with additional internal electrodes has been studied also in [165]. In this study a reconstruction approach based on boundary element method (BEM) was proposed to estimate conductivity values of a few predetermined regions with point like internal electrodes. Two dimensional numerical simulations in that study also clearly showed improvements in the conductivity estimates compared with traditional EIT with boundary electrodes only.

In this chapter, a finite element –based estimation approach which takes the internal structures into account in the modeling and utilizing these structures as internal electrodes is presented. The mathematical modeling is based on the complete electrode model of EIT. The proposed method utilizes two different internal electrode configurations. In addition, a directional smoothness constrained inversion for two-dimensional EIT (2D) presented in Chapter 3 is tested. These methods are tested with 2D numerical simulations and with laboratory experiments. The results are compared qualitatively and quantitatively with traditional EIT based on boundary measurements only.

6.2 Internal electrodes and current patterns in EIT

In traditional EIT, the electrodes are attached on the outer surface of the domain only. In this case, there are no any current sources within the domain as discussed in Chapter 3. If internal current sources exist, equation (3.17) is of the form $\nabla \cdot \sigma \nabla u = I_{\text{int}}$, where $I_{\text{int}} = \nabla \cdot \boldsymbol{J}_{\text{s}}(\boldsymbol{x})$. In this case, internal current density $\boldsymbol{J}_{\text{s}}(\boldsymbol{x})$ has to be modeled. This is easy to perform, if point like internal electrodes are used. This approach is given in [165]. In this chapter, different kind of approach is presented. It is assumed here, that an internal structure is inside the domain such that finite dimensional electrodes, not point like, can be attached on this structure. This type of a situation is valid for example in the case when there is a non-conducting rod in the center of the domain. In this case, the actual region is annular excluding the region occupied by the rod. For example, if four electrodes are attached on the surface of the rod, the finite element mesh of the domain looks as shown in Figure 6.1. Therefore, there actually are no any real *internal* electrodes but the domain differs from what has been used in conventional approaches. In the computations complete electrode model can be used by considering the domain Ω correctly and setting the electrodes e_ℓ in the correct locations on the outer and inner boundaries. Similarly, if there is a metallic rod in the domain, this can be modeled with a rod having one electrode on the surface of the rod, enclosing the whole structure.

As discussed in Chapter 3, currents can be injected in many different ways to the object, resulting in various current distributions in the domain. In this chapter, the following simple approaches are used. In the conventional approach with only the outermost surface electrodes, adjacent current injections are used, with adjacent voltage measurements. With one internal electrode, a one reference electrode approach is utilized in which the currents are injected successively between the internal reference electrode and all the other electrodes. The voltages were measured similarly. In four internal electrode case, the currents were injected between all the adjacent surface electrodes, between one internal and one surface electrode and again between all the adjacent internal electrodes. The voltages were measured similarly. For a more precise explanation of the data collection method, see Table 6.1.

6.3 Numerical simulations

One of the main interests in industrial process tomography is the detection of air distribution in stirrer vessels. Quite often this leads to situations in which the air bubbles create annular, low conducting region around the shaft of the rotor in the center of the vessel. Very often the shaft is metallic causing difficulties in standard EIT image reconstruction. In addition, the high contrast due to the low

Table 6.1: Data collection methods for the Cases 2 and 4. In the Case 3 the reference electrode is electrode number 1 and the boundary electrodes are numbered from 2 to 17. In the Case 4 the internal and boundary electrodes are numbered from 1 to 4 and from 5 to 20, respectively.

Case 3		Case 4	
Current injection	Voltage measurements	Current injection	Voltage measurements
1–2	1–2/1–3/.../1–17	1–2	1–2/2–3/.../4–1/1–5/.../20–5
1–3		2–3	
⋮	⋮	⋮	⋮
1–17	1–2/1–3/.../1–17	4–1	1–2/2–3/.../4–1/1–5/.../20–5
		1–5	1–2/2–3/.../4–1/1–5/.../20–5
		5–6	1–2/2–3/.../4–1/1–5/.../20–5
		⋮	⋮
		20–5	1–2/2–3/.../4–1/1–5/.../20–5

conducting air bubbles makes the reconstruction even more difficult.

In this section, a situation is considered in which there is an annular, low conducting region around the center of a two dimensional region, assumed to be a cross-section of a cylindrical stirrer vessel. There is a fixed shaft, conducting or insulating, in the center of the domain. The main interest is detection of the location of the low conducting region. The following reconstruction approaches are considered

1. Traditional reconstruction with adjacent current injection using 16 surface electrodes without any special *a priori* information. A metallic shaft was placed in the center of the domain.
2. The same as the Case 1. but the rod was taken into account in the mesh generation. The rod was not used for current injection or voltage measurements.
3. Approach in which the metallic shaft is used as an additional ground electrode.
4. Approach in which four additional electrodes are attached on the surface of the insulating shaft in the center of the tank.

In addition, for the Case 3. the effect of the anisotropic prior explained in Chapter 3 is tested.

In the Cases 1 and 2 the boundary electrodes are numbered from 1 to 16. In these cases a traditional adjacent method has been used, thus the number of the measurement was 256. In the Case 3 the metallic shaft is electrode number 1 and

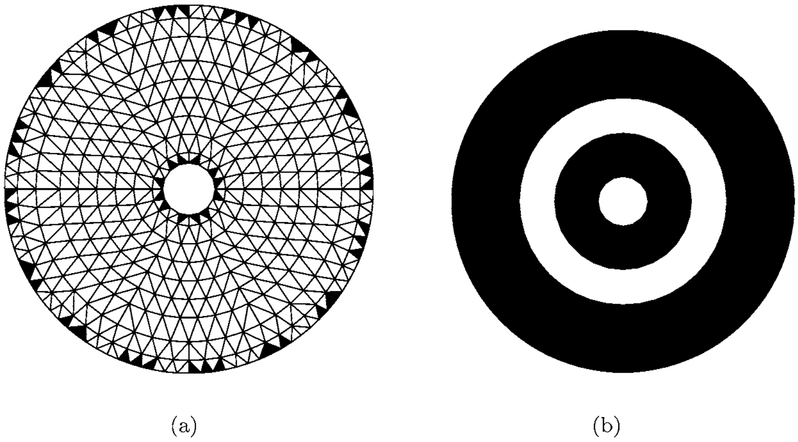
(a) (b)

Figure 6.1: (a) The 2D mesh used in the four internal electrode computations. The elements under the electrodes are marked with black elements. (b) The true resistivity distribution used in this work. The circle in the center depicts the rod and the annulus depicts the resistivity ring.

the boundary electrodes are numbered from 2 to 17. Also in this case the number of measurements is 256. Finally, in the Case 4 the four internal electrodes and boundary electrodes are numbered from 1 to 4 and from 5 to 20, respectively. In this case the number of the measurements is 441. The data collection methods for the Cases 3 and 4 are given in Table 6.1. Although, based on the reciprocity, half of the measurements are not linearly independent, all the measurements were used in the reconstruction. This is justified since in practice the measurements are noisy.

First, simulated electrode voltage data for a situation shown in Figure 6.1(b) is computed. In the FEM computation second-order basis function for potential distribution is used and the resistivity distribution is estimated on a piece-wise constant basis as in Chapter 5. The resistivity of the background was $\rho = 40$ Ωcm and the resistivity of the ring $\rho = 70$ Ωcm. In case 1, the finite-element mesh was circular, including the conducting shaft. The resistivity of the shaft was $\rho = 2.5 \cdot 10^{-6}$ Ωcm. In all other cases the finite-element mesh was as shown in Figure 6.1(a). This implies that the resistivity of the shaft is assumed to be infinite. The Gaussian, zero mean random noise having the variance of 1 % of the voltage range was added to the simulated voltages. In the estimation, Gauss-Newton method was used, which is in this case

$$\boldsymbol{\rho}_{i+1} = \boldsymbol{\rho}_i + \left[J_i^T J_i + \Gamma_{\mathrm{pr}}^{-1}\right]^{-1} \left[J_i^T(\boldsymbol{V} - U(\boldsymbol{\rho})) - \Gamma_{\mathrm{pr}}^{-1}\boldsymbol{\rho}_i\right]. \tag{6.1}$$

It is assumed here, that the measurement noise covariance matrix is I and the mean $\boldsymbol{\rho}^*$ is zero. The prior model is an anisotropic model presented in Chapter 3. The relative errors of the true resistivity distribution $\boldsymbol{\rho}_{\mathrm{t}}$ versus the estimated resistivity distribution $\boldsymbol{\rho}_{\mathrm{e}}$ as $\|\boldsymbol{\rho}_{\mathrm{t}}\|^2/\|\boldsymbol{\rho}_{\mathrm{t}}-\boldsymbol{\rho}_{\mathrm{e}}\|^2$ were computed. These are given in corresponding figures.

Four different cases introduced above were tested and the reconstructions are shown in Figures 6.2 and 6.3. It can be seen from the results, that if any assumptions regarding the internal conductor is not made, it is impossible to detect the low conducting region, see Figures 6.2(a) and 6.2(b). If the information on the presence of the conducting shaft is taken into account, the reconstruction shown in Figure 6.2(c) is obtained. The result is similar to the first case. The relative error in this case, however, is smaller than that in the previous one.

If the conducting shaft is utilized as an internal electrode and it is used for the current injection, one end up having much better reconstruction as seen in Figures 6.3(a) and 6.3(b). The poorly conducting annulus can be detected quite well even though it is spread over a wider region than it should be. Similarly, if it is possible to insulate the shaft from the surroundings and apply four additional electrodes on the surface of the shaft, a reconstruction shown in Figure 6.3(c) is obtained. The result is similar to the previous one and actually slightly worse in the center even though there are more electrodes and hence more measurement data than there were in the conducting shaft case. In these cases the relative errors are almost the same.

6.4 Laboratory measurements

In the laboratory experiments the geometry and structures inside the domain are similar to the situations in the simulations. Also the reconstructions are similar but now difference estimation method (3.84) is used instead of static method. According to equation (3.84), the difference estimation method is

$$\delta\boldsymbol{\rho} = \left[J_0^T J_0 + \Gamma_{\mathrm{pr}}^{-1}\right]^{-1} J_0^T \delta\boldsymbol{V}, \tag{6.2}$$

where the same assumption about the measurement noise covariance matrix is made as in the numerical simulations. Also the prior model is the same as in the numerical simulations.

All the measurements were carried out in a two-dimensional tank shown in Figure 6.4. The radius of the tank was 14 cm and its height was 10.5 cm. The tank was filled with saline solution. Stainless–steel electrodes were attached on the boundary of the tank. The width of the electrodes was 2.5 cm; thus they covered 45 % of the outer boundary of the tank. The height of the electrodes is the same as that of the tank. For the conducting shaft case, a stainless steel rod (of diameter 4 cm) was placed in the center of the tank. It was used as a grounded electrode during the current injection. For Case 4, a plastic rod (of diameter 4 cm) was used. Four additional electrodes were attached to the rod. These electrodes were made of thin copper tape. The width of the internal electrodes was also 2.5 cm. The poorly conducting annular region was simulated with a foam plastic ring of height 10.5 cm, shown in Figure 6.4(a). Since the electrodes and the foam plastic ring are of

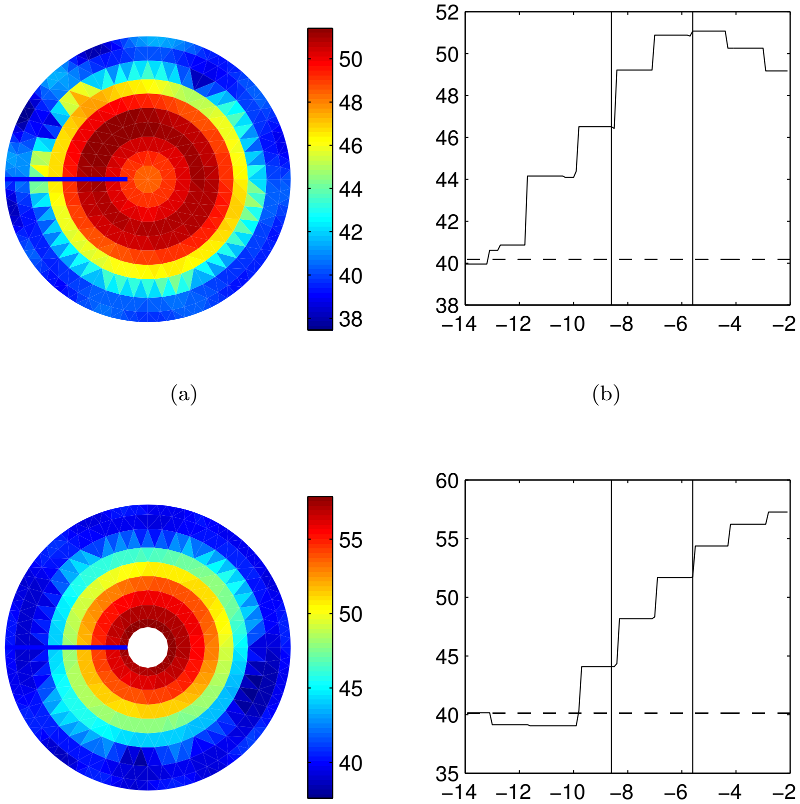

(a) (b)

(c) (d)

Figure 6.2: The reconstructions obtained from boundary measurements: (a) conventional reconstruction, (b) the profile along the radius in (a) (black line in (a)), (c) the reconstruction in which the central shaft is modeled as a non-current-carrying electrode and (d) the profile along the radius in (c). In both cases the regularization parameter $\alpha = 10^{-4}$. In (b) and (d) the solid lines are profiles and the dashed lines denote the estimated best homogeneous distribution. The relative error in (a) and (c) are 0.0137 and 0.0023, respectively. The unit of resistivity (color bar and ordinate) is Ωcm and the unit of radius (abscissa) is cm.

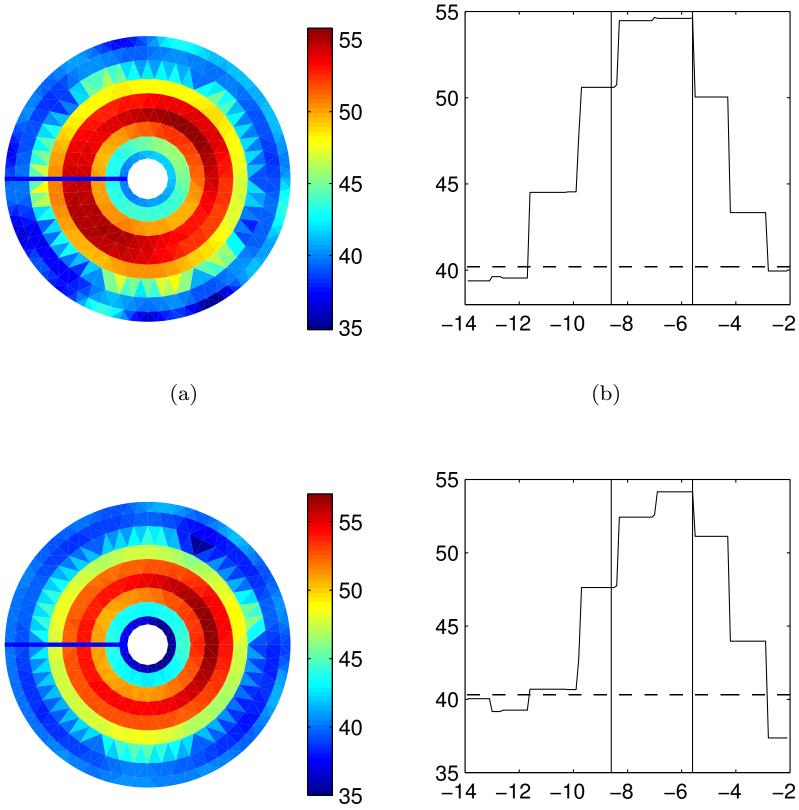

(a) (b)

(c) (d)

Figure 6.3: The reconstruction obtained from the boundary and additional internal measurements for (a) one grounded electrode and (c) four internal electrodes. For the explanations of (b) and (d) see Figure 6.2. In (a) and (c) the regularization parameter $\alpha = 10^{-4}$. The relative errors in (a) and (c) are 0.0013 and 0.0015, respectively. The units in figures are Ωcm and cm.

(a) (b)

Figure 6.4: The experimental arrangement. (a) The two-dimensional tank with 16 boundary electrodes. In the center of the tank there is also a grounded stainless steel electrode. The foam plastic ring is also in the tank. (b) The central rod with four internal electrodes.

the same height as the tank, the assumption of the two-dimensionality is justified. The conductivity of the annular region was about 75 % of the conductivity of the saline solution. The measurements were carried out using a modified version of the EIT measurement system introduced in [150].

6.4.1 Results of the reconstructions

The results of the tank experiments are shown in Figures 6.5 and 6.6. The reference voltages were measured with saline-filled tank and the actual measurement with the resistive object in the tank. The annular region should be seen as a greater resistivity $\delta\boldsymbol{\rho} > 0$, in the images. As in the simulations, the poorly conducting annulus cannot be detected with the traditional surface electrode approach, see Figure 6.5. Even when the conducting shaft is taken into account in the modeling but is not used as a current injecting electrode, the foam plastic ring cannot be seen, see Figure 6.5(c).

If the conducting shaft is used as an additional grounded electrode and it is exploited for the current injection and voltage measurements, the reconstruction improves substantially, see Figures 6.6(a) and 6.6(b). The poorly conducting annulus is well identified, even though the boundaries of the annulus are smoothed. The same effect was also seen in the simulations. If the shaft is insulated and four additional electrodes are attached to the shaft, one would assume to get an even better reconstruction. However, as it can be seen in the simulations, the result is not much better. The only improvement is the increase in accuracy of the background value near the boundary, Figure 6.6(b).

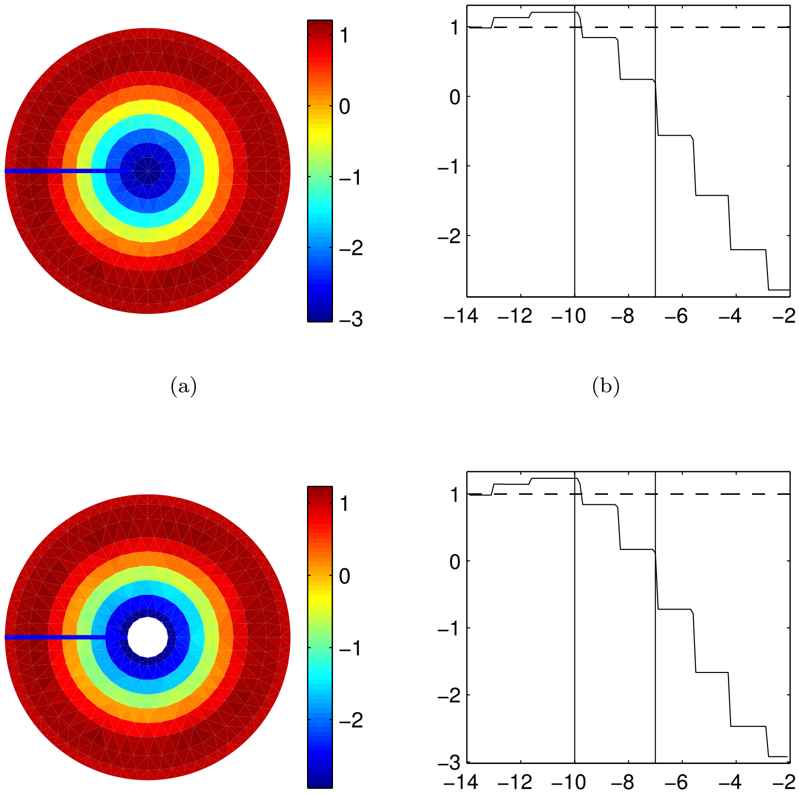

(a) (b)

(c) (d)

Figure 6.5: The reconstructions $\delta\boldsymbol{\rho}$ obtained from boundary measurements: (a) the conventional reconstruction, (b) the profile along the radius in (a) (black line in (a)), (c) the reconstruction in which central shaft is modeled as non-current-carrying electrode and (d) the profile along the radius in (c). In both cases the regularization parameter $\alpha = 5 \cdot 10^{-8}$. In (b) and (d) the solid lines are profiles and the dashed lines denote the estimated best homogeneous distribution.

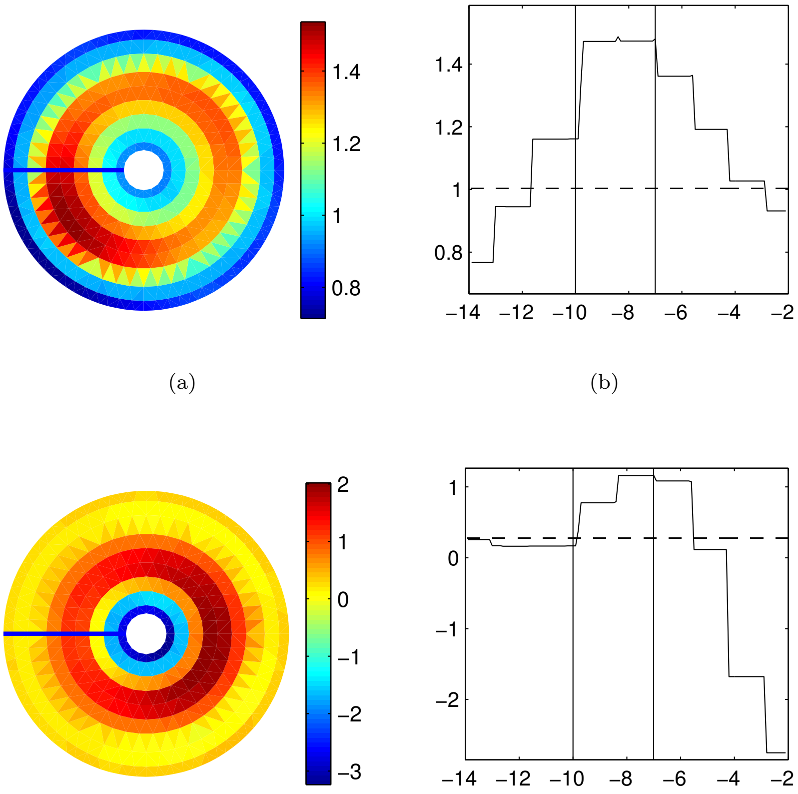

(a) (b)

(c) (d)

Figure 6.6: The reconstruction $\delta\boldsymbol{\rho}$ obtained from the boundary and additional internal measurements for (a) one grounded electrode and (c) four internal electrodes. For the explanations of (b) and (d), see Figure 6.5. In (a) regularization parameter $\alpha = 5 \cdot 10^{-8}$, whereas in (c) $\alpha = 10^{-5}$.

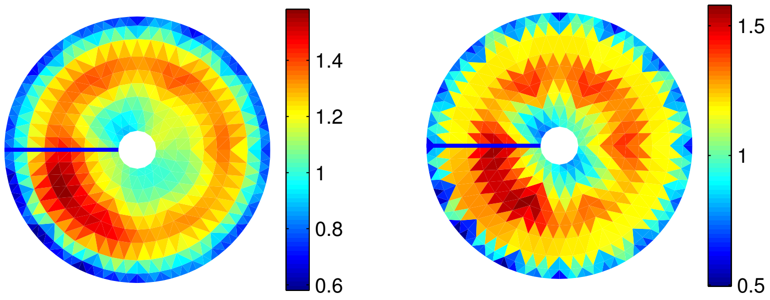

(a) $w^\theta = 1$, $w^r = 1$ (b) $w^\theta = 1$, $w^r = 30$

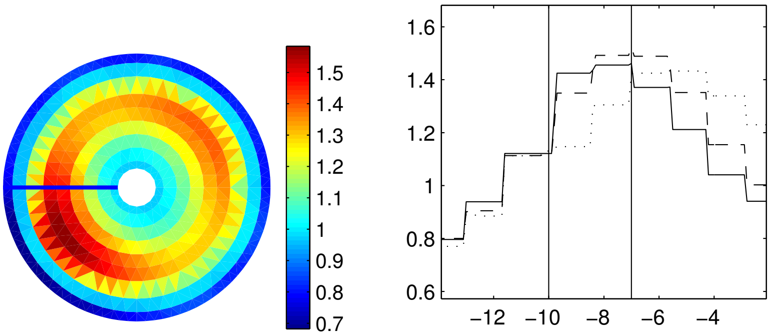

(c) $w^\theta = 30$, $w^r = 1$ (d)

Figure 6.7: The effect of prior information on the reconstruction: (a) with the assumption of isotropy (b) with the assumption of the smoothness along the radius (c) with assumption of rotational invariance and (d) the profiles along the radius (black lines in (a), (b) and (c)). In (d) the dashed line is for (a), the dashdot line is for (b) and the solid line (c).

6.4.2 Anisotropic prior

The effect of the anisotropic weighting in the regularization was tested with the real measurement case with the grounded electrode. The results are shown in Figure 6.7. The effect of the anisotropic prior is clearly seen in the images even though the actual resistivity values are quite similar, Figure 6.7(d). The density of the foam plastic annulus was not exactly constant, which is well seen in Figure 6.7(a) as a greater resistivity. Also, the same can be seen in Figure 6.7(c) although the increase is slightly smoothed out due to the assumption of (greater) smoothness in the angular direction.

6.5 Summary

In this chapter, reconstruction approaches that exploit internal structures by using them as additional internal electrodes was proposed. Also an approach for exploiting anisotropic prior information in the image reconstruction was tested.

By simulations and laboratory experiments it was shown that the internal structures can be used in the image reconstruction and the results were shown to be much better than without this prior information. It was shown that with the resistivity contrast ratio used in the study, the poorly conducting annular region cannot be detected without considering the internal structures in the reconstruction. It was also found that by using the conducting shaft as an additional internal electrode the final reconstruction is almost as good as with four additional electrodes. Therefore, in practice, with the low resistivity contrast ratio, it seems reasonable just to ground the conducting internal structure and use it for the current injection and voltage measurements. However, it should be pointed out that the current injection scheme in the case of four internal electrodes might not have been the optimal one and better reconstructions could be obtained by using different current patterns.

CHAPTER VII

Volume fraction estimation

7.1 Introduction

There are two different types of volume fraction information in process industry, *the volume fraction distribution* and *the bulk volume fraction.* The volume fraction distribution is percentual fraction of some material within another material as a function of spatial coordinates. For example, percentual fraction of gas within a liquid. The bulk volume fraction is the space-averaged value of the volume fraction distribution over some fixed volume. Sometimes, the bulk volume fraction is referred to as holdup.

The above mentioned volume fraction information of gas or solid plays a very important role in many industrial systems. For example, in three-phase reactors the bulk volume fraction of the different phases is a parameter that affects the hydrodynamics and kinetics of a process [167]. As a concrete example, the flotation column can be mentioned in which the gas holdup affects the flotation performance and hence the efficiency of the column. An example, in which the volume fraction distribution is of importance, is the estimation of the volumetric flow rate of two/three phase flow [114]. In this case, the cross-sectional volume fraction distribution of each phase and the velocity profile of the flow have to be determined. In the light of the above examples of industrial processes, accurate estimation of the volume fraction is very important.

The volume fraction can be measured using different measurement techniques. A method in which the radial gas volume fraction profile is estimated using attenuation of gamma radiation was presented in [174, 94]. One drawback of the radiation based method is that only a time averaged volume fraction distribution can be measured. This is due to the long measurement time required by this method. This kind of method is therefore not applicable in the cases in which the dynamical behavior of the process is significant compared to the measurement time. This drawback can be eliminated by using for example electrical methods. A method which was based on the measurement of the electrical bulk conductivity of the dispersion was developed in [167]. The relationship between the bulk volume fraction and the electrical conductivity of the dispersion can be found from the literature. Time response of this method is fast enough for dynamic processes. If the volume fraction distribution is of interest, this method is not adequate since only the bulk volume fraction can be estimated. Further benefit can be obtained if the volume fraction distribution of the phases can be determined, for example gas–liquid and solid–liquid mixers can be designed for greater efficiency and gas–liquid, gas–solid or gas–liquid–solid reactors can be controlled [185]. This spatial detail can be provided by process tomography equipment and in particular the above example applications can all be imaged using EIT.

7.2 Tomographic estimation of volume fraction distribution

Let us assume that the volume fraction distribution is parametrized and within the domain Ω it is identified by a vector $\boldsymbol{\phi} = (\phi_1, \phi_2, \ldots, \phi_m)^T \in \mathcal{M} \subset \mathbb{R}^m$ and it can be represented in the form

$$\phi(\boldsymbol{x}) = \sum_{i=1}^{m} \phi_i B_i(\boldsymbol{x}), \ \ \phi_i \in [0,1] \ \forall \ i, \tag{7.1}$$

where $B_i(\boldsymbol{x})$ are basis functions. Moreover, indirect noisy tomographic measurements $\boldsymbol{g} = (g_1, g_2, \ldots, g_n)^T \in \mathcal{D} \subset \mathbb{R}^n$ are made on the boundary of the domain $\partial\Omega$. The volume fraction distribution is related to these indirect measurements through known nonlinear operator $\widetilde{K} : \mathcal{M} \to \mathcal{D}$ as follows

$$\boldsymbol{g} = \widetilde{K}(\boldsymbol{\phi}) + \boldsymbol{v}, \tag{7.2}$$

where the operator $\widetilde{K}$ is deterministic model in which all relevant physical features of the measurement situation are included. It is important to note that, in all tomography techniques, the estimated quantity is not directly volume fraction distribution but some other physical quantity. For example, in gamma-densitometry tomography the estimated quantity is an attenuation coefficient of the medium [57]. Hence, the mathematical relationship between the estimated quantity and the volume fraction distribution is needed. With the aid of this relationship the following composite mapping can be derived

$$\widetilde{K}(\boldsymbol{\phi}) = K(f(\boldsymbol{\phi})) := (K \circ f)(\boldsymbol{\phi}), \tag{7.3}$$

where $K(\cdot)$ is the forward model modeling relationship between the measurements and estimated parameters. Moreover, $f(\boldsymbol{\phi})$ is the deterministic model between the estimated parameters and the volume fraction distribution. According to the equation (2.9) the likelihood density for the model (7.2) is given by

$$\pi(\boldsymbol{g} \mid \boldsymbol{\phi}) \propto \exp\left(-\frac{1}{2}(\boldsymbol{g} - \widetilde{K}(\boldsymbol{\phi}))^T \Gamma_v^{-1} (\boldsymbol{g} - \widetilde{K}(\boldsymbol{\phi})) \right). \tag{7.4}$$

In other words, the likelihood density is the conditional probability density of the measurements $\boldsymbol{g}$ given the parameters $\boldsymbol{\phi}$.

Now, according to (2.14) the posterior density can be written in the form

$$\pi(\boldsymbol{\phi} \mid \boldsymbol{g}) = \exp\Big(-\frac{1}{2}(\boldsymbol{g} - \widetilde{K}(\boldsymbol{\phi}))^T \Gamma_v^{-1}(\boldsymbol{g} - \widetilde{K}(\boldsymbol{\phi})) - \alpha W(\boldsymbol{\phi})\Big), \tag{7.5}$$

where α and $W(\boldsymbol{\phi})$ are the regularization parameter and regularizing functional, respectively. The posterior density can be used to calculate various estimates for the material distribution $\boldsymbol{\phi}$ as well as uncertainty estimates for these estimates, see Chapter 2.

7.2.1 Estimation of volume fraction distribution using EIT

Since the estimated quantity in EIT is conductivity distribution the material-to-conductivity mapping is needed. More precisely, in this case the mapping $S : (\boldsymbol{\phi}, \sigma_b) \mapsto \boldsymbol{\sigma}$ is needed for the estimation of local volume fraction distribution using EIT. The function S maps the value of the local volume fraction of the material and the background conductivity of the material to the conductivity of the domain.

Let us assume that the function S is known, the model (7.3) can be written in the form

$$\begin{aligned} \boldsymbol{V} &= U(S(\boldsymbol{\phi}, \sigma_b)) + \boldsymbol{\eta} \\ &= \widetilde{U}(\boldsymbol{\phi}, \sigma_b) + \boldsymbol{\eta}, \end{aligned} \tag{7.6}$$

where $\widetilde{U}$ is the composite mapping $(U \circ \boldsymbol{\sigma})(\boldsymbol{\phi}, \sigma_b)$. The equation (7.6) is now the model for the relationship between the local volume fraction distribution, the background conductivity and the voltages measured using EIT. Therefore, the posterior density for the local volume fraction distribution $\boldsymbol{\phi}$ and the background conductivity σ_b given data $\boldsymbol{V}$ can be written as

$$\begin{aligned} \pi(\boldsymbol{\phi}, \sigma_b \mid \boldsymbol{V}) \;\propto\; & \exp\Big(-\frac{1}{2}(\boldsymbol{V} - \widetilde{U}(\boldsymbol{\phi}, \sigma_b))^T \Gamma_v^{-1}(\boldsymbol{V} - \widetilde{U}(\boldsymbol{\phi}, \sigma_b)) \\ & -\alpha W(\boldsymbol{\phi}) - \gamma W(\sigma_b)\Big), \end{aligned} \tag{7.7}$$

where γ and $W(\sigma_b)$ are the regularization parameter and the regularizing functional for the background conductivity, respectively. It is assumed that the material distribution and the background conductivity are independent i.e. $\pi(\boldsymbol{\phi}, \sigma_b) = \pi(\boldsymbol{\phi})\pi(\sigma_b)$.

The positivity constraint (3.47) for the background conductivity and following constraint for the local volume fraction distribution are also necessary

$$\pi_\Delta(\phi_k) = \begin{cases} 1, & \text{if } 0 \leqslant \phi_k \leqslant 1, \quad \forall\, 1 \leqslant k \leqslant m \\ 0, & \text{otherwise} \end{cases}. \tag{7.8}$$

Note that this prior density is proper whereas the density of the positivity constraint (3.47) is improper.

7.2.2 Conductivity models for dispersion

The electrical conductivity of dispersions was widely investigated during the 19th and 20th centuries [125, 129, 17]. The conductivity of the dispersion depends on several properties of the dispersion. For example, shape, orientation, ordering, phase volume fraction and the conductivities of the dispersed and the background material will change the conductivity of the dispersion [17]. In this thesis it is assumed that the conductivity of the dispersion is a function of the phase volume fraction and the background conductivity only. Moreover, it is assumed here that the dispersion consist of two materials i.e. it is two-phase dispersion.

The simplest model for two-phase dispersion is the Maxwell model [125]

$$S(\phi, \sigma_b) = \sigma_b \frac{1 + 2\beta\phi}{1 - \beta\phi}, \tag{7.9}$$

where

$$\beta = \frac{\sigma_d - \sigma_b}{\sigma_d + 2\sigma_b}, \tag{7.10}$$

where σ_d is the conductivity of the dispersed material and σ_b is the conductivity of background. If the conductivity $\sigma_d = 0$, the $\beta = -1/2$, equation (7.9) reduces to

$$S(\phi, \sigma_b) = 2\sigma_b \frac{1 - \phi}{2 + \phi}. \tag{7.11}$$

The assumptions of the Maxwell model are that the particles are spherical, the dispersion is dilute ($\phi < 0.2$) and the particle size distribution is a delta function, which means that all the particles are of the same size.

The Maxwell model is used in this thesis and it is assumed that the dispersed material is air and therefore $\sigma_d = 0$, and the spherical shape of small air bubbles is not unrealistic. In this case equation (7.11) can be written in the form

$$S(\phi, \sigma_b; x_k) = 2\sigma_b \frac{1 - \sum_i^K \phi_i B_i(x_k)}{2 + \sum_i^K \phi_i B_i(x_k)} := S_k(\phi, \sigma_b), \tag{7.12}$$

where x_k is the k^{th} node in the finite element mesh and K is the number of the parameter of the volume fraction distribution. If the same discretization for the air volume fraction and conductivity distributions is used the function S_k reduces to

$$S(\phi, \sigma_b)_k = 2\sigma_b \frac{1 - \phi_k}{2 + \phi_k}. \tag{7.13}$$

Other possible models are Bruggeman's model [129] in which the particle size distribution is not a delta function but more realistic one and Fricke's model [18] in which the shape of the dispersed material can be elliptical.

7.2.3 The MAP estimation

In this section, the computation of the MAP-estimate of the air volume fraction distribution is presented. According to equation (2.32) MAP-estimate can be obtained using Gauss-Newton method which is also used here. In this presentation the posterior distribution is of the form of (7.7) such that the background conductivity is known. The iteration in this case can be written in the form

$$\begin{aligned}\phi_{i+1} = \phi_i \quad &+ \quad \kappa_i \left[J_i^T \Gamma_v^{-1} J_i + \frac{1}{2}\alpha H_i^W \right]^{-1} \\ &\left[J_i^T \Gamma_v^{-1}(\boldsymbol{V} - \widetilde{U}(\phi_i)) - \frac{1}{2}\alpha g_i^W \right], \qquad (7.14)\end{aligned}$$

where κ_i is the step length parameter. Moreover, the J_i is the Jacobian of the mapping $\widetilde{U}(\phi)$ with respect to ϕ. Since the mapping $\widetilde{U}$ is the composite mapping, the Jacobian can be obtained by the chain rule of the differentiation as

$$\begin{aligned} J(\phi) = \frac{\partial (U \circ S)(\phi)}{\partial \phi_\ell} \quad &= \quad \sum_{j=1}^{N} \frac{\partial U}{\partial \sigma_j}(S(\phi)) \frac{\partial S_j}{\partial \phi_\ell}(\phi) \ \forall\ 1 \leq \ell \leq K \qquad (7.15) \\ &= \quad J_U(S(\phi)) J_S(\phi), \qquad (7.16) \end{aligned}$$

where $J_U(\cdot)$ is the Jacobian of the mapping $U(\sigma)$ with respect to σ, (see the equation (3.68)) and $S(\cdot)$ is the mapping (7.9). The $J_S(\phi)$ is the Jacobian of the Maxwell model (7.9) with respect to ϕ, that is,

$$J_S(\phi) = \frac{\partial S}{\partial \phi} = \begin{bmatrix} \frac{\partial S_1}{\partial \phi_1} & \frac{\partial S_1}{\partial \phi_2} & \cdots & \frac{\partial S_1}{\partial \phi_K} \\ \frac{\partial S_2}{\partial \phi_1} & \frac{\partial S_2}{\partial \phi_2} & \cdots & \frac{\partial S_2}{\partial \phi_K} \\ \vdots & \vdots & \ddots & \vdots \\ \frac{\partial S_N}{\partial \phi_1} & \frac{\partial S_N}{\partial \phi_2} & \cdots & \frac{\partial S_K}{\partial \phi_N} \end{bmatrix} \in \mathbb{R}^{N \times K}, \ K \leq N. \qquad (7.17)$$

If the same discretization is used for the air volume fraction and conductivity distributions the Jacobian $J_S(\phi)$ can be written in the form

$$J_S(\phi) = \operatorname{diag}\left(\frac{\partial S_1}{\partial \phi_1}, \frac{\partial S_2}{\partial \phi_2}, \ldots, \frac{\partial S_N}{\partial \phi_N} \right) \in \mathbb{R}^{N \times N}, \qquad (7.18)$$

where diag$(\cdot)$ is the diagonal matrix in which the entries are

$$\frac{\partial S_k}{\partial \phi_k} = -\frac{2}{3} \frac{\sigma_b}{(1 + (1/2)\phi_k)^2}. \qquad (7.19)$$

The operators g_i^W and H_i^W in the equation (7.14) are the following derivatives

$$\begin{aligned} g_i^W \quad &= \quad \frac{\partial W}{\partial \phi_k}(\phi_i), \ 1 \leqslant k \leqslant m \qquad (7.20) \\ H_i^W \quad &= \quad \frac{\partial^2 W}{\partial \phi_k \partial \phi_j}(\phi_i), \ 1 \leqslant k, j \leqslant m. \qquad (7.21) \end{aligned}$$

In other words, they are the gradient and the Hessian of the regularization functional (2.11), respectively. By comparing equation (7.14) to equation (2.32) it can be seen that

$$
\begin{aligned}
g_i^W &= \frac{2}{\alpha}\Gamma_{\rm pr}^{-1}(\phi_i - \phi^*), & (7.22)\\
H_i^W &= \frac{2}{\alpha}\Gamma_{\rm pr}^{-1}. & (7.23)
\end{aligned}
$$

In other words, the Hessian matrix can be interpreted as a scaled inverse matrix of the prior covariance matrix and correspondingly the gradient matrix as the same scaled matrix multiplied by the difference between the current distribution ϕ_i and a priori known distribution ϕ^*.

7.3 Numerical simulations

In this section, the results of numerical simulations of the volume fraction estimation are shown. Two different cases are studied. In the first the 3D volume fraction distribution within a cylindrical tank is estimated. In the second the effect of the conductivity contrast between the background and dispersed material conductivity on the estimation is studied. Use of the internal electrode is also studied in this case. In this last case the simulations were carried out in 2D. In the both cases the Maxwell model (7.11) is used.

7.3.1 3D simulation

The estimation of the volume fraction distribution in 3D is presented. The simulations were carried out in a cylindrical tank. The radius and height of the tank were 20 cm and 44 cm, respectively. In the center of the tank there was a metal shaft having the radius of 2.5 cm. The shaft was used as a reference electrode. Moreover, 64 electrodes were located at the boundary of the tank. The part of the finite element mesh used in the computations is shown in Figure 7.1. The number of the elements was 6072 and the number of the nodes was 1344. In the FEM computations linear basis functions for the potential and conductivity were used. The currents were injected successively between all the boundary electrodes and the internal reference electrode. The voltages were measured similarly. The number of the data therefore was $64 \times 64 = 4096$.

The estimated volume fraction distribution was chosen to be

$$
\phi(r,z,\theta) = \begin{cases} 0.2, & \text{if } 7 \leqslant r \leqslant 14, \quad 0 \leqslant z \leqslant 28, \quad \forall\, \theta \\ 0.05, & \text{otherwise.} \end{cases} \qquad (7.24)
$$

The distribution is shown in Figure 7.2. Gaussian distributed random noise having the variance of 1 % of the voltage range was added to the simulated voltages. The contact impedances were assumed to be known and they were $z_\ell = 0.5\ \Omega\text{cm}^2\ \forall\, \ell$. Estimated images were solved using the Gauss-Newton iteration (7.14) in which the measurement noise covariance matrix was assumed to be an identity matrix i.e. $\Gamma_v = I \in \mathbb{R}^{n\times n}$. An anisotropic prior model presented in Section 3.3.2 was used as

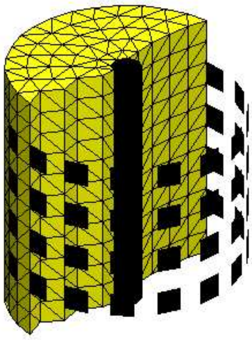

Figure 7.1: The 3D mesh used in the computations. Only half of the mesh is shown. The boundary electrodes and one internal electrode are also shown.

a prior. In this case, the regularization parameters for the radius, angle and height were $\alpha_r = 1 \cdot 10^{-7}$, $\alpha_\theta = 1 \cdot 10^{-3}$ and $\alpha_z = 1 \cdot 10^{-5}$, respectively. The step length was $\kappa_i = 0.2 \;\forall\; i$ and the initial distribution was chosen to be a homogeneous distribution the value being 0.5. Moreover, the conductivity distribution of the background was 0.2 mS/mm.

The result after 20 Gauss-Newton iterations is shown in Figure 7.3. It can be seen that the volume fraction distribution can clearly be identified. The shape and the value of the estimate are fairly good. The effect of the anisotropic prior can also be seen. The distribution is smooth in angular direction whereas abrupt change in the radial direction is not smoothed out. Also, the sharp edge in the height direction is clearly seen. The inner edge of the annular ring is also very clear which is obviously due to the use of the internal electrode. This is studied in more detail in the next numerical simulation in 2D. The error norm is shown in Figure 7.4. It can be seen that the convergence of the algorithm is quite slow. This is due the small constant step size parameter. The use of the optimal step size parameter presented in Chapter 4 would improve the convergence of the method.

7.3.2 Effect of conductivity contrast

The effect of the conductivity contrast between the background and dispersed material is studied. The results of traditional EIT and the internal electrode approaches are compared. Different volume fraction distributions are considered. As an example, the estimation of the air volume fraction in stirrer vessel is used.

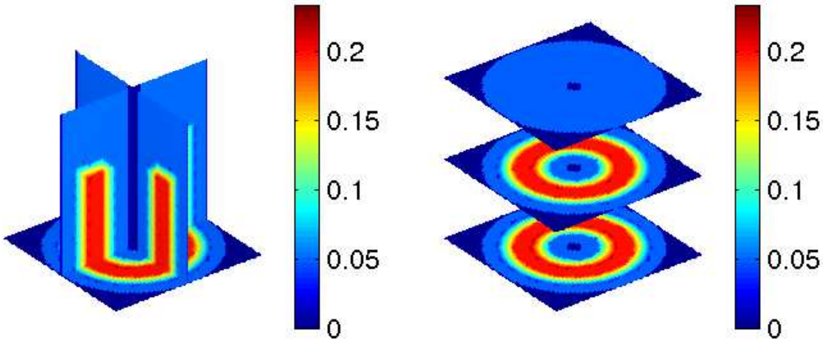

Figure 7.2: The true volume fraction distribution.

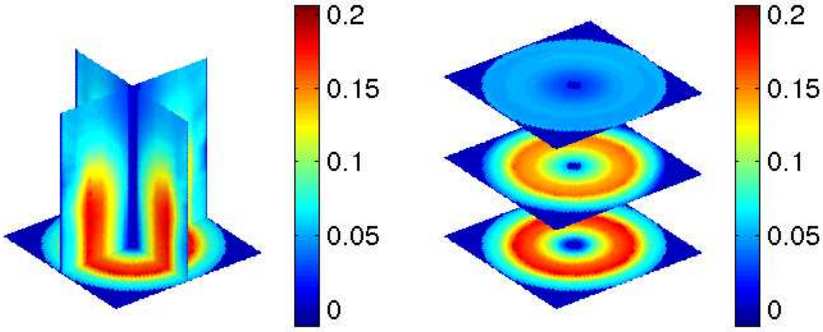

Figure 7.3: The estimated volume fraction distribution.

Moreover it is assumed that the air bubbles create annular, low conducting region around the shaft of the rotor in the center of the vessel.

All simulations were carried out in a 2D circular domain. The radius of the domain was 14 cm and in the center of the domain there was a shaft having the radius of 2 cm. In this case, the actual domain used in the computations is annular, excluding the domain occupied by the shaft. The finite element mesh used in the simulations is shown in Figure 7.5(a). In the FEM computations second order basis functions for the potential distribution approximation were used. The number of elements and nodes in the forward mesh were 732 and 1576, respectively. In the inverse problem the conductivity is estimated in linear basis. The number of the estimated parameters, i.e., the number of the nodes was 422, see figure 7.5(b).

As discussed above it is assumed that the volume fraction distribution is rota-

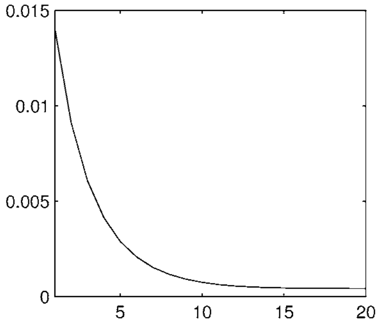

Figure 7.4: The error norm as a function of iteration number.

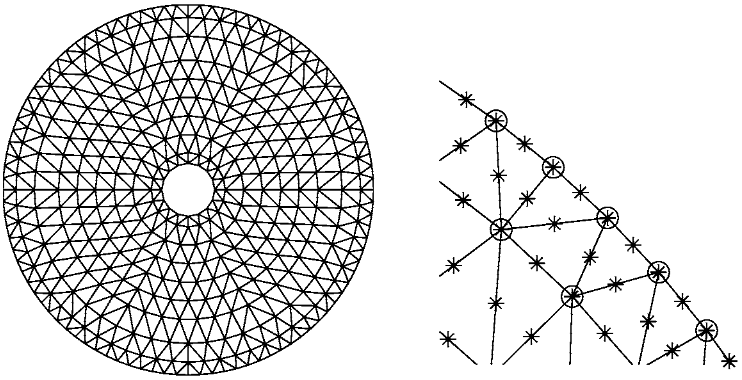

(a) (b)

Figure 7.5: (a) The 2D mesh used in the computations. (b) The part of the mesh. The circles and stars denote the nodes in which the conductivity and the potential are presented, respectively.

tionally invariant, the radial profile being Gaussian function as

$$\phi(\theta, r) = \phi_0 \exp(-a(r-b)^2), \ \forall\, \theta, \ 2 \leqslant r \leqslant 14, \tag{7.25}$$

where ϕ_0 is the maximum volume fraction at the position b and a is a parameter which controls the width of the distribution. In all the simulations the values of a and b were 0.05 and 7, respectively. The corresponding conductivity distributions were computed by equation (7.11). The conductivity of the liquid σ_b was 0.1 $(\Omega\mathrm{m})^{-1}$. Two radial profiles and one corresponding conductivity distribution are shown in Figure 7.6.

For the evaluation 17 different volume fraction distributions and the corresponding conductivity distributions were computed by varying the maximum volume fraction ϕ_0 between 0.15 and 0.97. The contrast ratio varied correspondingly between 1.24 and 43.5 and the mean volume fraction between 0.083 and 0.54. The contrast ratio is defined as the ratio of the maximum and minimum values of the conductivity distribution. For these distributions the simulated voltages on the electrodes were computed by the forward model using FEM. Gaussian distributed random noise of 1% was added in the simulated voltages. The estimates for the volume fraction distribution were computed by iterating the Gauss-Newton algorithm (7.14) 10 iterations. An identity matrix was used as a measurement noise covariance matrix. In the simulations, the anisotropic regularization scheme presented in Section 3.3.2 was utilized in which the annular nature of imaged distribution is taken into account. The convergence of the algorithm was ensured by visual examination. The regularization parameter α was also tuned by visual examination.

For each volume fraction distribution the bulk volume fraction ϕ_m is defined by the following formula

$$\phi_\mathrm{m} = \frac{1}{A} \int_A \phi(x) \mathrm{d}a, \tag{7.26}$$

where the A is the area/volume of the domain Ω. It should be noted that the bulk volume fraction ϕ_m can be same for different local volume fraction distributions. Moreover, the relative errors (RE) are computed as follows

$$\mathrm{RE} = \frac{\int_A (\phi(x) - \hat{\phi}(x))^2 \, \mathrm{d}a}{\int_A (\phi(x))^2 \, \mathrm{d}a}, \tag{7.27}$$

where ϕ and $\hat{\phi}$ are the true volume fraction distribution and the estimated volume fraction distribution, respectively.

In order to study the effect of the internal electrodes on the reconstruction the following three different approaches were considered

1. Traditional reconstruction with adjacent current injections and voltage measurements using 16 boundary electrodes. The shaft in the center is modeled as a non-current carrying electrode in the computations. The shaft is not used for current injection or voltage measurements.

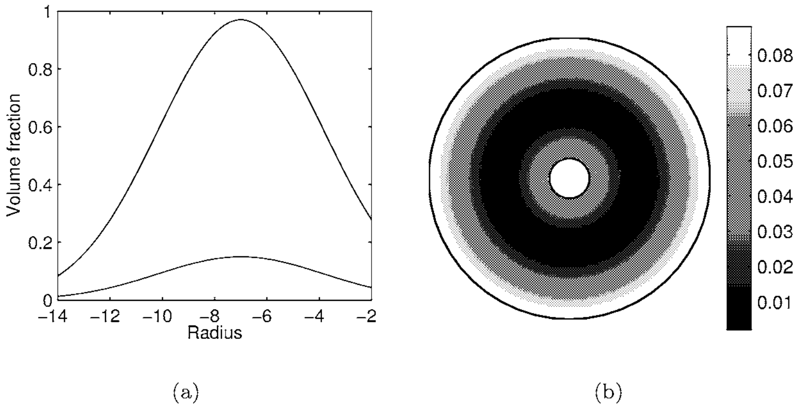

(a) (b)

Figure 7.6: (a) The radial volume fraction. In the lower line ϕ_0 is 0.15 and in the upper line 0.97. (b) The conductivity distribution corresponding the volume fraction distribution with $\phi_0 = 0.97$. The units of the radius and the conductivity are cm and Ωm^{-1}, respectively.

2. Approach in which the metallic shaft is used as an additional ground electrode. In this case currents are injected successively between the internal reference and all the other electrodes. The voltages are measured similarly.
3. Approach in which four additional electrodes are attached on the surface of the insulating shaft in the center of the tank. In this case the currents were injected between all the adjacent boundary electrodes, between one internal and one boundary electrode and finally between the adjacent internal electrodes. The voltages were measured similarly.

The estimated bulk volume fractions as a function of contrast ratio are shown in Figure 7.7(a). It can been seen that the approaches 1 and 2 overestimate the mean volume fraction with all contrast ratios. Only in the approach 3 the estimates are consistent with the true values. Since the bulk volume fraction can be the same for different volume fraction distributions the relative errors RE between the true and the estimated distributions were also computed.

The relative errors RE as a function of contrast ratio are plotted in Figure 7.7(b). It can be seen that in the approach 1 with the lowest contrast ratio the relative error is highest, the error being 0.289. This is caused by the conductive shaft in the center. In the first approach the relative error decrease as the contrast ratio increases, up to the value of 10. After that the error starts to increase which is due to the decreased sensitivity near the center of the domain. In the approaches 2 and 3 the relative errors are nearly equal below the contrast ratio of 10. In the approach 2 the error with the lowest contrast ratio is 0.027 and in the approach

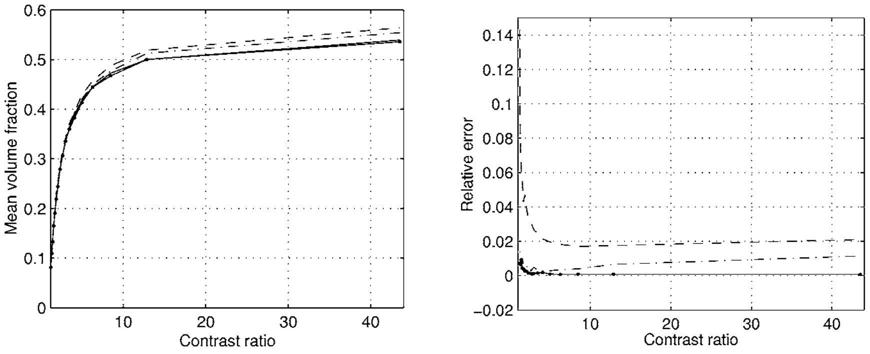

(a) (b)

Figure 7.7: (a) The mean volume fractions as a function of contrast ratio. (b) The relative errors as a function of contrast ratio. The solid line is for the true fraction, the dashed line is for the approach 1, the dotted line is for the approach 2 and the dash-dotted line is for the approach 3.

3 it is 0.009. With the highest contrast ratio these errors are 0.028 and 0.001, respectively. Only in the approach 3 the relative error remains the same with different contrast ratios.

To get a more closer view on the differences between the three approaches, the radial profiles of the estimated volume fraction distributions were computed and the results are shown in Figure 7.8. In the approach 1 with the lowest contrast ratio, the shaft disturbs the reconstruction substantially, especially near the center. This effect was also seen in the relative error in Figure 7.7(b). In the same approach with the highest contrast ratio the same effect can be seen but it is much weaker. However, still the estimates for the volume fraction in the center of the domain are unsatisfactory. In the approach 2, the effect of the shaft is avoided by using the shaft as internal electrode. However, the relative error for the value of the volume fraction in the innermost point is 0.67 for the lowest contrast ratio and 1.14 for the highest contrast ratio. Finally, in the third approach the estimated profiles are more consistent with the true profiles. The largest error can be seen in the maximum value of the profile with the lowest contrast ratio. The relative error in the innermost points for the lowest and highest contrast ratios is 0.09.

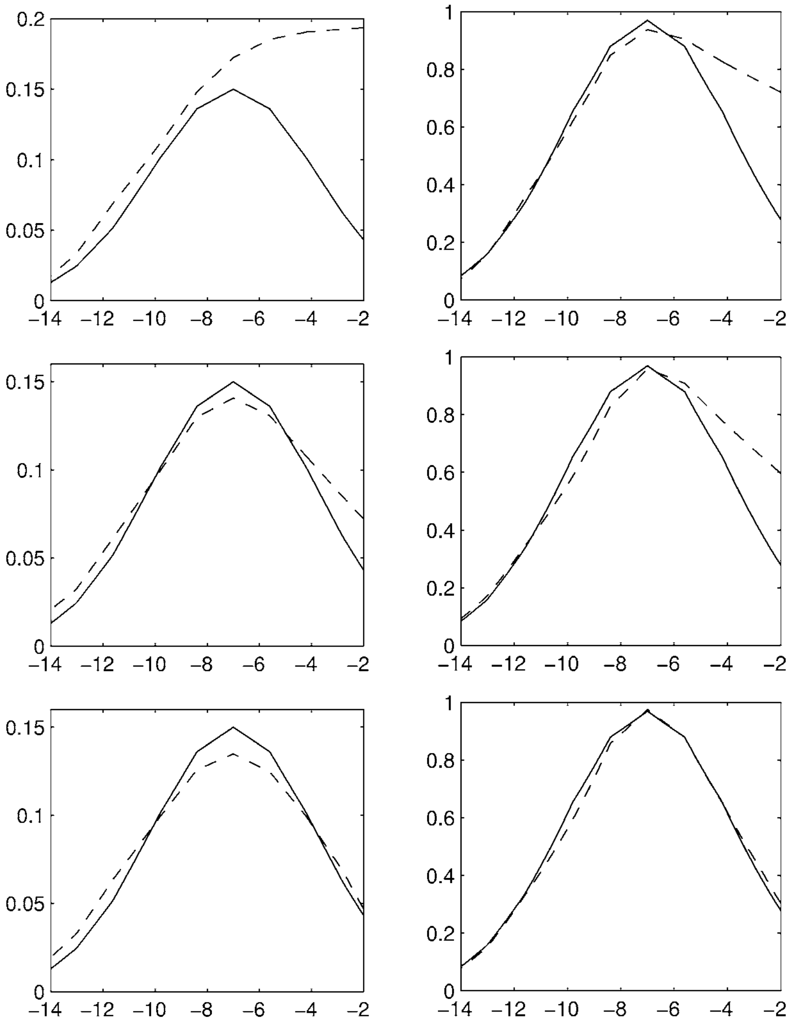

Figure 7.8: The radial local volume fractions. Top row is for the approach 1, middle row is for the approach 2 and bottom row is for the approach 3. The solid lines are the true profiles and the dashed lines are the estimated profiles. On the left column the profiles are for the case with the lowest contrast ratio and on the right column for the highest contrast ratio. In each figure the abscissa is the radius (cm) and the ordinate is the local volume fraction.

7.4 Laboratory experiment

In this section, laboratory experiments are presented. The aim is to study the volume fraction estimation of the gas-liquid mixture in a tank. The measurements are carried out with EIT measurement system developed in the Department of applied physics, University of Kuopio. The details of the measurement system can be found in [149]. The estimation method based on difference reconstruction scheme is used.

The experiments were carried out in a cylindrical tank. The radius and height of the tank were 200 mm and 520 mm, respectively. The tank was made of transparent plastic. Equally spaced 80 stainless steel electrodes were attached on the boundary of the tank such that they were in five different layers. The measurement tank is shown in Figure 7.9. The tank was filled with tap water.

The current injection protocol used in this experiment was not a traditional one. It was an opposite protocol modified for 3D case. In the first current injection opposite electrodes on the first and fourth electrode layers were used. The voltages were measured from the adjacent electrodes on each layers. In the second injection the current injection was rotated two electrodes anticlockwise and the injection layers were changed to second and fifth layers. This procedure was repeated until eight current injections were performed. For a more precise explanation of the current injection protocol, see Table 7.1. The number of data points collected using this protocol is 8 × 80 = 640. The amplitude and frequency of the current was 1 mA and 7812.5 Hz, respectively.

Table 7.1: The current injection protocol. The column numbers are the electrodes on each layer and row numbers are the layer numbers. The figures in the cells are the ordinal numbers of the current injection. The electrodes of the first current injection are denoted by circles.

		Electrode															
		1	2	3	4	5	6	7	8	9	10	11	12	13	14	15	16
Layer	1	①				3				5				7			
	2			2				4				6				8	
	3																
	4	5				7				①				3			
	5			6				8				2				4	

The estimation of the air volume fraction is based on the difference method presented in Section 3.3.3. In the case of volume fraction distribution a model between the conductivity and the volume fraction distributions has to be used. Since the dispersed material is air ($\sigma_d = 0$) the equation (7.11) is used. The whole estimation procedure is described stepwise as follows.

1. Measure a reference data set $\boldsymbol{V}_0$ with homogeneous conductivity distribution

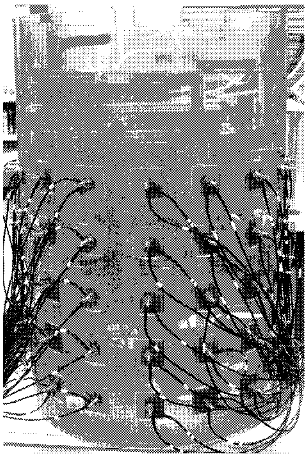

Figure 7.9: The tank used in the experiment.

such that air is not injected to the tank, i.e. $\phi_0 = 0$. Moreover, perform the repeated voltage measurements from the tank such that the current injection units are switched off. From these measurements compute the measurement noise covariance matrix which is of the form $\Gamma_v = \sigma_i^2 I \in \mathbb{R}^{n\times n}$, where σ_i^2 are the variances of the each individual measured voltages.

2. Compute the estimates for the homogeneous conductivity distribution $\boldsymbol{\sigma}_0$ (i.e. the conductivity of water $\boldsymbol{\sigma}_b$) and the contact impedances $\boldsymbol{z}_0$ using equations (4.9) and (4.14). It is assumed here that the contact impedance is the same on each electrode.

3. Construct a matrix K for the difference reconstruction, that is,

$$K = [J^T \Gamma_v^{-1} J + \Gamma_{\text{pr}}^{-1}]^{-1} J^T \Gamma_v^{-1}, \tag{7.28}$$

   where the Jacobian J is computed in the point $(\boldsymbol{\phi}_0, \boldsymbol{z}_0)$ using equation (7.15). Note that the volume fraction distribution $\boldsymbol{\phi}_0$ is zero. According to equations (7.13), (7.15) and (7.17) the Jacobian is therefore of the form $J(\boldsymbol{\phi})|_{\phi=0} = -(3/2)J(\boldsymbol{\sigma}_0)\boldsymbol{\sigma}_0$. Construct a prior covariance matrix Γ_{pr} according to equation (3.64).

4. Measure a data set $\boldsymbol{V}$ and compute an estimate for the volume fraction distribution as follows

$$\boldsymbol{\phi} = K(\boldsymbol{V} - \boldsymbol{V}_0). \tag{7.29}$$

5. Visualize the volume fraction distribution $\boldsymbol{\phi}$ and go back to item 4.

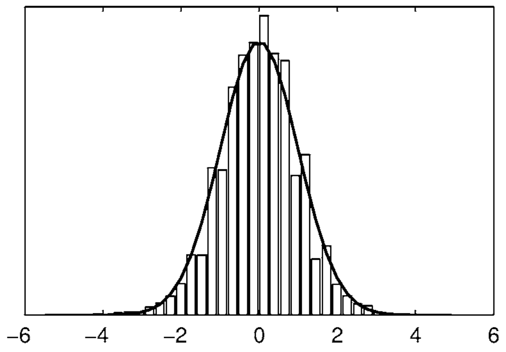

Figure 7.10: The measurement noise histogram. The mean is $-3 \cdot 10^{-23}$ and the variance is $\sigma^2 = 1 \cdot 10^{-9}$. The solid line is fitted Gaussian distribution. The factor of the abscissa is 10^{-4}.

Let us first consider the measurement noise covariance matrix mentioned in item 1. The measurement noise histogram of one measurement is shown in Figure 7.10. It can be seen that the distribution is Gaussian. It can also be seen that the mean of the distribution is essentially zero and hence the use of the zero mean Gaussian distribution as a noise model is justified. The assumption of the diagonal measurement noise covariance matrix is not valid in every case. For example, in noisy industrial environment the voltage measurement could be strongly correlated. The approximation and modelling errors also cause correlated voltage measurements [88]. In this case the mean of these errors are not necessarily zero.

The homogeneous conductivity $\boldsymbol{\sigma}_0$ and contact impedances $\boldsymbol{z}_0$ were estimated using the method presented in Chapter 4. The whole reference data set $\boldsymbol{V}_0$ was used as data for the computation. The computation was performed in the mesh in which the number of the elements and nodes were 59723 and 12553, respectively. The surface of the mesh is shown in Figure 7.11(a). It can be seen that the mesh is dense specially near the electrodes which reduces the approximation error. The reference voltage measurements corresponding to the first current injection are shown in Figure 7.12. The computed voltages are also shown in the same figure. Qualitatively, the fit seems to be tolerable. The squared error norm of the whole fit, i.e. $\|\boldsymbol{V}_0 - U(\boldsymbol{\sigma}_0, \boldsymbol{z}_0)\|^2$, is 0.0074. The estimated values of the homogeneous conductivity and contact impedance were 0.21 ± 0.01 mS/cm and 0.77 ± 0.03 $\Omega \cdot \mathrm{cm}^2$, respectively. The conductivity was also measured using a commercial conductivity probe[†] which gave the value of 0.24 mS/cm for the water conductivity. The difference between the measured values might be due to the many different aspects. For example, the estimation is sensitive to modelling

---

[†] Hanna Instruments DIST WP4 conductivity tester.

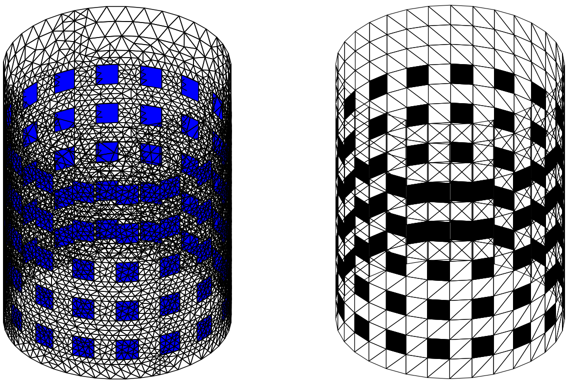

(a) Forward mesh (b) Inverse mesh

Figure 7.11: The meshes used in computations.

errors and also the homogeneous assumption is not necessarily valid.

The mesh used in the computation of the Jacobian is shown in Figure 7.11(b). In this case the number of the elements and nodes in the mesh were 6240 and 1358, respectively. The volume fraction distribution was approximated in piecewise linear basis and therefore also the Jacobian was computed in with respect to nodal values of the conductivity. The prior model which was used here is presented in Section 3.3.2. The fixed parameters were Gaussian distributed, that is $\boldsymbol{\phi}_{\mathcal{I}_2} \sim N(\boldsymbol{\phi}^*_{\mathcal{I}_2}, \Gamma_2^{-1})$, where the index set $\mathcal{I}_2$, i.e. the index set for the fixed parameters, was chosen to include all boundary nodes in vertical surface as well as one node in the middle of the both ends of the tank. Hence, the number of the fixed parameters was 450. The mean $\boldsymbol{\phi}^*_{\mathcal{I}_2}$ of these parameters was chosen to be zero. Moreover, the covariance matrix is of the form $\Gamma_2 = \sigma^2 I$, where the variance σ^2 is $1 \cdot 10^{-4}$. In other words, the fixed parameters were assumed to be independently and identically distributed. In the prior model the smoothness operator was anisotropic smoothness prior presented in Section 3.3.2. In this case it was assumed that the conductivity distribution is isotropic.

If the estimation method (7.29) is compared with the Gauss-Newton method (7.14) it can be seen that the presented method is a one step solution of G-N iteration ($i = 0$) based on the assumption that $\boldsymbol{\phi}_0 = \boldsymbol{\phi}^* = 0$, $\kappa = 1$ and $U(\boldsymbol{\phi}_0) = \boldsymbol{V}_0$. Note also that by using the proposed prior model the number of the unknown parameters is reduced from 1358 to 908, which improves the conditioning of the problem.

Finally in item 4 measurements are performed for which air was injected into the water filled tank through a sparger which was placed on the bottom of the tank, see Figure 7.13(a). The estimated air volume fraction distribution is shown in Figure 7.13(b). The location of air stream is well detected. The maximum

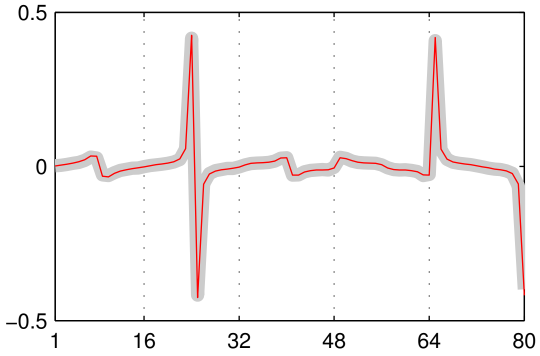

Figure 7.12: The reference voltage measurement corresponding to the first current injection. Thick gray line is for measured voltages and thin red line is for computed voltages. The dotted lines indicates the change of the electrode layer.

value of the air volume fraction is in the bottom of the tank and it is nearly 10 %. This is not probably high enough which is due to the linear approximation in the estimation procedure and the smoothness assumption in the prior model. It seems that air is spread out in upper layers and in the same time the air volume fraction decreases which is a natural behaviour. This phenomenon can also be seen in Figure 7.14 in which the air volume fraction distribution in different layers as a contour plot is shown. The maximum air volume fraction in the upper layer ($z = 50$ cm) is about 0.24 % which is obviously too low. This is due to both the above mentioned assumptions and the fact that the upper layer is too far from the sensing zone and therefore the sensitivity in that area is low. In this experiment the data acquisition time was 180 ms/frame which means that the frame rate was 5.5 frame/s.

7.5 Summary

In this chapter, the estimation of the volume fraction distribution using EIT was studied. The estimation method was based on statistical inversion. The method is tested with 2D/3D numerical simulations and a 3D laboratory experiment. In the numerical simulations also the use of the internal electrodes was studied.

It was also shown by numerical simulation that the MAP-estimation of the air volume fraction is possible. Moreover, it was shown by numerical simulations that by utilizing the internal electrodes the estimates are substantially improved especially in the center of the vessel and when the contrast ratios are low. It can also be said that with low contrast ratios it seems reasonable to use one grounded electrode for the current injection and voltage measurements. In practice this

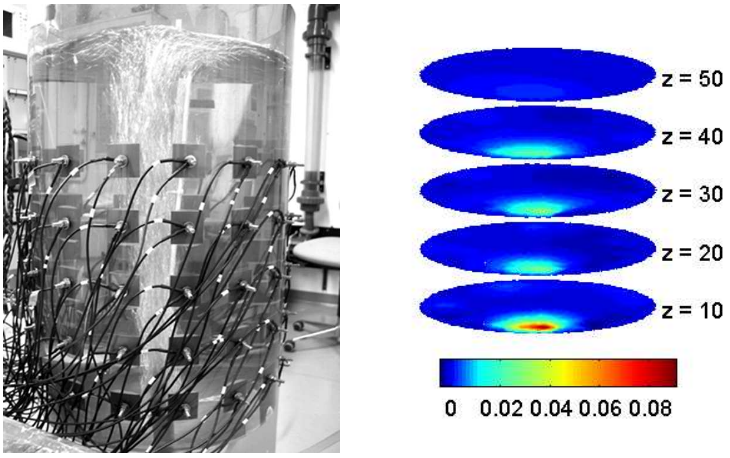

(a) (b)

Figure 7.13: (a) The air flow within the tank. (b) The estimate of the air volume fraction in different layers. Note that a modified colormap is used. The unit of the height is cm.

approach is also easier to implement than the four internal electrodes -approach. However, with the highest contrast ratios, the four internal electrodes -approach produced more satisfactory estimates than the other two approaches. This is due to the fact that in this approach we get more data from the central area.

The laboratory experiment of the air volume fraction estimation was also presented. In this case the estimation is based on the one step Gauss-Newton method. This method is closely related to the NOSER reconstruction method presented in [38]. By the experiment it was shown that the estimation of the air volume fraction distribution is possible in laboratory environment and the results are quite promising. The accuracy of the method is not necessarily adequate for all purposes and it could be improved using more steps in the G-N iteration.

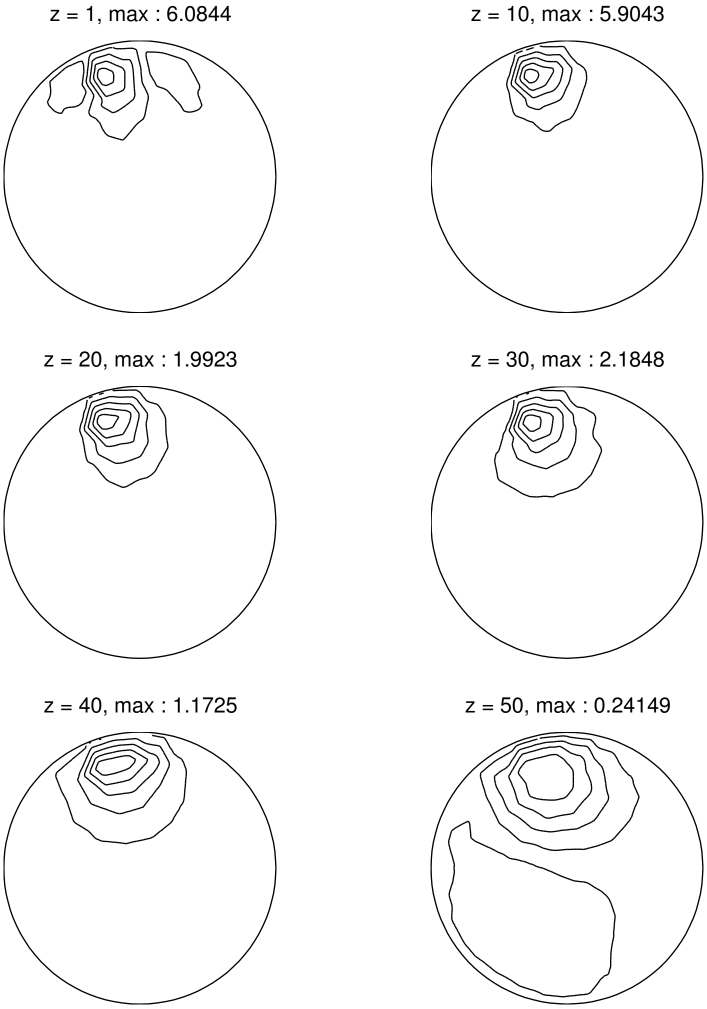

Figure 7.14: Percentage of air as contour plots.

Chapter VIII

Volume fraction prior model

8.1 Introduction

For many industrial process the bulk volume fraction of one phase such as gas or solid can be of considerable importance. For this reason it is often controlled within certain limits and therefore is known at least vaguely. Prior information on the bulk volume fraction can assist in tomographic inversion, even if this information is not precise. An example in which the bulk volume fraction is known is the sedimentation of suspensions of small particles in a fluid [32]. Specifically, in batch settling of suspension in a laboratory column, the bulk volume fraction of the particles is known quite accurately.

In this section, a novel prior model for the case in which information on the bulk volume fraction can be taken into account is presented. The proposed method is tested with 2D numerical simulations. The numerical examples are simple illustrative examples that show how the proposed prior model works.

8.2 Bulk volume fraction prior model

The bulk volume fraction is denote here by ϕ_{m}. Actually the expectation ϕ^*_{m} and variance $\sigma^2_{\phi_{\mathrm{m}}}$ of the bulk volume fraction are assumed to be known. The probability density of the bulk volume fraction is assumed to be a truncated Gaussian density, that is,

$$\pi(\phi_{\mathrm{m}}) \propto \begin{cases} \exp(-\frac{1}{2\sigma^2_{\phi_{\mathrm{m}}}}(\phi_{\mathrm{m}} - \phi^*_{\mathrm{m}})^2), & \phi_{\mathrm{m}} \in [0,1]. \\ 0, & \text{otherwise.} \end{cases} \tag{8.1}$$

The bulk volume fraction of the local volume fraction distribution $\boldsymbol{\phi}$ is defined mathematically as the following integral operator

$$\mathcal{K}\boldsymbol{\phi} = \frac{1}{|\Omega|}\int_{\Omega} \boldsymbol{\phi} \mathrm{d}\boldsymbol{x} =: \phi_{\mathrm{m}}, \tag{8.2}$$

where $|\Omega|$ is the area or the volume of the domain Ω and $\boldsymbol{\phi}$ is as in (7.1). The integral operator therefore can be written in the form

$$\mathcal{K}\phi = \kappa_1\phi_1 + \ldots + \kappa_i\phi_i + \ldots + \kappa_m\phi_m =: \phi_{\mathrm{m}}, \tag{8.3}$$

where the κ's are the weights of the numerical integration method[‡]. Further, one of the parameters can be solved as

$$\phi_i = h(\phi_{\mathcal{I}}) + \frac{1}{\kappa_i}\phi_{\mathrm{m}}, \tag{8.4}$$

where $\mathcal{I}$ is the index set $\{1, 2, \ldots, i-1, i+1, \ldots, m\}$ and the h is a known function of the parameter $\phi_{\mathcal{I}}$.

The prior density (i.e. the joint density of the parameters $\phi_k, k = 1, \ldots, m$) can be written in the form

$$\pi_{\mathrm{Pr}}(\phi_i, \phi_{\mathcal{I}}) = \pi_1(\phi_i \mid \phi_{\mathcal{I}})\pi_2(\phi_{\mathcal{I}}), \tag{8.5}$$

where π_1 is a conditional density of parameter ϕ_i given the rest of the parameters $\phi_{\mathcal{I}}$ and the density π_2 is the joint density of the rest of the parameters. The density π_1 is truncated Gaussian density and it is of the form

$$\pi_1(\phi_i \mid \phi_{\mathcal{I}}) \propto \begin{cases} \exp(-\frac{\kappa_i^2}{2\sigma_{\phi_{\mathrm{m}}}^2}(\phi_i - (\frac{\phi_{\mathrm{m}}^*}{\kappa_i} + h(\phi_{\mathcal{I}})))^2), & \phi_i \in [0, 1] \\ 0, & \text{otherwise.} \end{cases} \tag{8.6}$$

Moreover, the density π_2 is uniform density. See proof of the equation (8.6) in [73]. Note that the proposed prior model fulfills the constraint (7.8). In Section 8.3 the prior model and the corresponding densities will be explained in more detail in the case of two parameters ϕ_1 and ϕ_2.

In the prior density (8.5) the volume fraction distributions with the bulk volume fraction ϕ_{m} have high probability while other distributions have lower probability. Note also that the prior density is uninformative in certain direction, since the operator $\mathcal{K}$ is not a bijection. This feature will be seen in a numerical example in Section 8.3. The main difference between the proposed prior and for example a smoothness prior is that the proposed prior is global, which means that only a global property of the unknown distribution is constrained while in the smoothness prior the smoothness of the solution is locally constrained.

8.3 Numerical examples

In this section, two different numerical examples are shown. By these examples, an idea behind the volume fraction constraint is explained. The computations were carried out in two dimensional circular domain, see Figure 8.1. The area of the domain was chosen to be one. The domain was divided in two equal sized parts. It was assumed, that the volume fraction in both of the parts is constant, the values being ϕ_1 and ϕ_2, respectively. On the boundary of the domain three electrodes

---

[‡] Note, ϕ_m is the m^{th} parameter and ϕ_{m} is the bulk volume fraction.

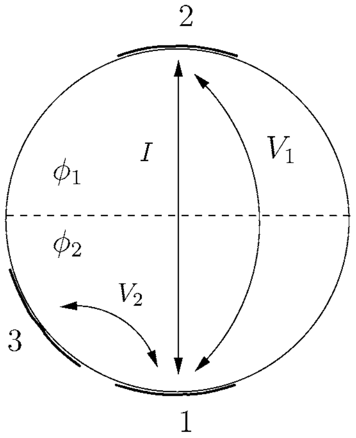

Figure 8.1: Schematic presentation of the examples.

were attached. As a current injection, only one current injection (I) was used and two voltage measurements (V_1 and V_2) were measured. The FEM computations were carried out in a mesh having 748 triangular elements and 428 nodes. For the potential distribution linear basis functions were used. Moreover, the conductivity was estimated in piecewise constant basis. The voltage data for the estimation problem was computed such that the volume fraction of the different parts was converted to the conductivity using the Maxwell model (7.9).

The measurement noise covariance matrix of the voltage measurements was constructed as follows. First, it was assumed that the noise of the voltage measurements consists of two independent parts. One was Gaussian, zero mean noise having the variance of 3 % of the voltage range V_r and the other one was also zero mean Gaussian noise having the variance of 3 % of each voltage value V_i hence $V_i \sim N(0, 0.03 \cdot (V_r + V_i))$. The first one represents noise that is common for every voltage measurement which can be, for example, induced from the measurement environment. The second represents the error in the voltage measurements. Next, 10000 samples from this density were drawn. The covariance matrix was calculated based on the samples. The covariance matrix is as follows

$$\Gamma_v = \begin{bmatrix} 2.7188 & 1.3644 \\ 1.3644 & 1.3435 \end{bmatrix}. \tag{8.7}$$

It can be seen that the noise of the voltage measurements are correlated and unidentically distributed. The correlation is due to the assumption of the common noise.

The discretization of the volume fraction distribution is chosen as follows

$$\phi(x, y) = \sum_{i=1}^{2} \phi_i \chi_i(x, y), \tag{8.8}$$

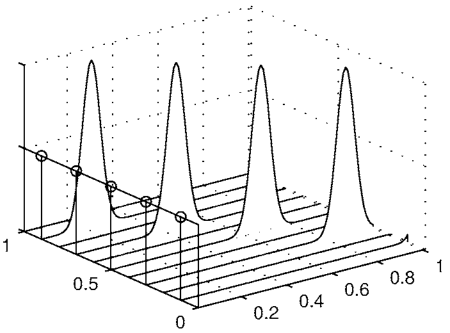

Figure 8.2: Prior probability density $\pi_{\mathrm{Pr}}(\phi_1, \phi_2)$. Five draws from uniform density $\pi_2(\phi)$ are marked by vertical lines with dots. The solid lines are for the conditional densities $\pi_1(\phi_2 \mid \phi_1)$. Left-handed horizontal axis is for the parameter ϕ_1 whereas right-handed axis is for the ϕ_2.

where $\chi_i, i = 1, 2$ are the characteristic functions of the domains $\Omega_i, i = 1, 2$, see Figure 8.1. The integral operator in the equation (8.6) can be written in discrete form

$$\begin{aligned} \mathcal{K}\phi &= \frac{1}{A}\int_A \Big(\phi_1\chi_1 + \phi_2\chi_2\Big)\mathrm{d}x\mathrm{d}y \\ &= \frac{1}{A}\Big(A_1\phi_1 + A_2\phi_2\Big) \\ &= (1/2)\phi_1 + (1/2)\phi_2 = \tilde{\mathcal{K}}\phi =: \phi_{\mathrm{m}}, \end{aligned} \tag{8.9}$$

where $\tilde{\mathcal{K}}$ is the vector $[1/2\ 1/2]$ and $\phi \in \mathbb{R}^2$ is the parameter vector. The parameter ϕ_2 can be solved from the equation (8.9) as

$$\phi_2 = 2\phi_{\mathrm{m}} - \phi_1. \tag{8.10}$$

Therefore in the equation (8.4) $\kappa_2 = 1/2$ and $h(\phi_1) = -\phi_1$. According to equation (8.5) the prior density can be written as

$$\pi_{\mathrm{Pr}}(\phi_1, \phi_2) = \pi_2(\phi_1)\pi_1(\phi_2 \mid \phi_1), \tag{8.11}$$

where

$$\pi_1(\phi_2 \mid \phi_1) \propto \begin{cases} \exp(-\frac{1}{2\sigma^2_{\phi_{\mathrm{m}}}}\frac{1}{4}(\phi_2 - (2\phi^*_{\mathrm{m}} - \phi_1))^2), & \phi_2 \in [0, 1] \\ 0, & \text{otherwise.} \end{cases} \tag{8.12}$$

It can be seen that this conditional density is a truncated Gaussian density with the expectation $E\{\phi_2 \mid \phi_1\} = 2\phi^*_{\mathrm{m}} - \phi_1$ and the variance $\sigma^2_{\phi_2 \mid \phi_1} = 4\sigma^2_{\phi_{\mathrm{m}}}$. These can also be easily verified from equation (8.10). Moreover, the density π_2 in equation

(8.11) is uniform between zero and one. An idea of the prior density is sketched in Figure 8.2. Five different samples are drawn from the uniform density $\pi_2(\phi_1)$ and the corresponding conditional densities $\pi_1(\phi_2 \mid \phi_1)$ are shown. It can be seen that the mean of the parameter ϕ_2 depends on the parameter ϕ_1 as it should be according to the conditional expectation $E\{\phi_2 \mid \phi_1\}$ presented above.

In both examples, the known bulk volume fraction ϕ_{m}^* and the variance $\sigma_{\phi_{\mathrm{m}}}$ of that were chosen to be 0.55 and 0.00395, respectively. Further, the values of the parameters ϕ_1 and ϕ_2 were chosen to be 0.8 and 0.3, respectively.

Known background conductivity, Case 1

In this case it is assumed that the background conductivity is known, the value being 0.5 mS/cm. Only two parameters (ϕ_1 and ϕ_2) therefore have to be estimated. The example is started by studying the probability densities associated with this case.

The probability densities are shown in Figure 8.3 as contour lines. In Figure 8.3(a) the likelihood density is presented in data space. Since the noise is correlated, the density contours are elliptical. Moreover, it can be seen that the variances of the voltages are unequal. Note that the scales of the ordinate and abscissa are different. It can also be seen that the density is a Gaussian density with mean of measured voltages. The shape of the density depends on the measurement noise covariance matrix Γ_v.

The likelihood density in parameter space is presented in Figure 8.3(b). It can be seen that the likelihood density is elongated near the correct values of the parameters which are [0.8 0.3]. Specially, the uncertainty of the parameter ϕ_2 is large. It can also be seen that the density is not Gaussian. This is due to the fact that the forward mapping $\widetilde{U}(\phi)$ is nonlinear. It is apparent that the maximum likelihood estimation is not adequate in this case.

The prior density (8.11) is shown in Figure 8.3(c). It can be seen that the probability mass of the prior density is concentrated near a straight line. Actually, the line is $\phi_2 = 2\phi_{\mathrm{m}} - \phi_1$. Thus, the role of the prior density is that it tends to pull the bulk volume fraction of the distribution towards the a priori known value without strictly constraining the solution to this value. It can also be seen that the infinitely many combinations of the parameters can give the same probability, which means that the prior density is uninformative in certain direction.

Finally, the posterior density i.e. the solution of the inverse problem is shown in Figure 8.3(d). The probability mass of the posterior density is concentrated near the correct values of the parameters. It can also be seen that the posterior density is also biased which means that the uncertainty of the parameters is correlated. Heuristically, it can be said that the posterior density is an intersection of the likelihood and the prior densities.

Next, the above example is studied in more detailed. The conditional mean (CM) and the maximum a posterior (MAP) estimates of the posterior density were computed. As mentioned in Chapter 2 that the computation of the conditional mean is an integration problem, so an MCMC scheme was used, see Chapter

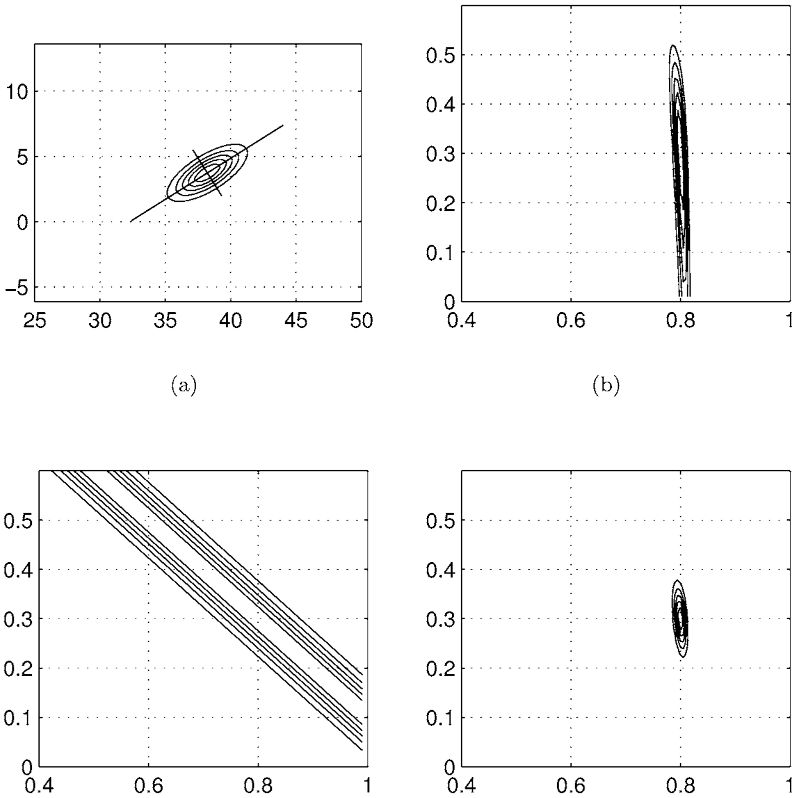

(a) (b)

(c) (d)

Figure 8.3: The probability densities associated with the first example. (a) Likelihood density in data space. The principle axes of the error ellipse are also presented. (b) Likelihood density in parameter space, (c) prior density, (d) posterior density . In (a) ordinate and abscissa are V_1 and V_2, respectively. In (b), (c) and (d) they are ϕ_1 and ϕ_2, respectively.

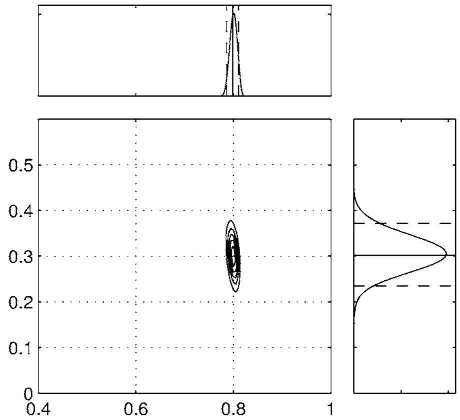

Figure 8.4: Posterior density and the marginal densities of both parameters. The solid and dashed lines in the marginal densities denote the conditional mean and the confidence limits. The ordinate and abscissa are ϕ_1 and ϕ_2, respectively.

2. Marginal densities and the posterior correlation of the parameters were also computed by using MCMC. The MAP estimate was computed with Gauss–Newton method. First, 100000 samples from the posterior density (7.5) with the prior model (8.5) were generated. The starting point of the Markov Chain was [0.7 0.7]. The burn-in period is chosen to be 100 samples to ensure that the draws were from the posterior density. The acceptance ratio was 0.1738. The good rule of thumb is that the acceptance ratio should be roughly 0.2 - 0.3 [60] thus the ratio is a little bit too small. On the other hand, the number of the samples is large and therefore the low acceptance ratio is accepted. The conditional mean (2.33), the marginal densities (2.38) and the 90% confidence limit (2.36) of the parameters were computed based on the samples. The posterior density, the marginal densities and the confidence limits with respect to both parameters are shown in Figure 8.4. It can be seen that the marginal density of the second parameter is wider than the first one which means that the first parameter is more reliable.

The posterior correlation matrix based on the samples is

$$R_{\phi \mid V} = \begin{bmatrix} 1 & -0.3867 \\ -0.3867 & 1 \end{bmatrix}. \tag{8.13}$$

It can be seen that the correlation between the parameters is negative. This can also be seen from the shape of the posterior density. This result is intuitively clear, since for example if the value of the first parameter increases, the value of the second parameter has to decrease in order to remain the bulk volume fraction the same. The results of this case are summarized in Table 8.1.

Next the MAP estimate of this example is computed using equation (7.14).

Table 8.1: Results of the Case 1. The AR is the acceptance ratio of the MCMC.

	ϕ_1	ϕ_2	AR
True	0.8000	0.3000	
CM	0.7989	0.3025	0.1738
Variance	0.0001	0.0017	

The regularization functional is now of the form

$$W(\phi) = \|(\tilde{\mathcal{K}}\phi) - \phi_{\mathrm{m}}\|^2. \tag{8.14}$$

The gradient of the functional can be obtained as

$$\begin{aligned} \frac{\partial}{\partial \phi_k}\left\{\|(\mathcal{K}\phi) - \phi_{\mathrm{m}}\|^2\right\} &= \frac{\partial}{\partial \phi_k}\left((\mathcal{K}\phi)^2 - 2(\mathcal{K}\phi)\phi_{\mathrm{m}} + {\phi_{\mathrm{m}}}^2\right) \\ &= \left(2\frac{\partial(\mathcal{K}\phi)}{\partial \phi_k}(\mathcal{K}\phi) - 2\phi_{\mathrm{m}}\frac{\partial(\mathcal{K}\phi)}{\partial \phi_k}\right) \\ &= 2\left((\mathcal{K}\phi) - \phi_{\mathrm{m}}\right)\frac{\partial(\mathcal{K}\phi)}{\partial \phi_k}, \end{aligned} \tag{8.15}$$

where

$$\frac{\partial(\mathcal{K}\phi)}{\partial \phi_k} = \frac{1}{|\Omega|}\left(\int_\Omega \frac{\partial \phi}{\partial \phi_k}\mathrm{d}\boldsymbol{x}\right). \tag{8.16}$$

Note that the volume integral depends on the discretization of the material distribution. For example, if the piecewise constant approximation is used, the equation can be written in the form

$$\frac{\partial(\mathcal{K}\phi)}{\partial \phi_k} = \frac{|\Omega_k|}{|\Omega|}, \tag{8.17}$$

where $|\Omega_k|$ is the area of the k^{th} element in the mesh.

Moreover, the Hessian can be obtained from the gradient

$$\begin{aligned} \frac{\partial g_W^{(i)}}{\partial \phi_j} &= 2\frac{\partial}{\partial \phi_j}\left((\mathcal{K}\phi) - \phi_{\mathrm{m}}\right)\frac{\partial(\mathcal{K}\phi)}{\partial \phi_k} + \left((\mathcal{K}\phi) - \phi_{\mathrm{m}}\right)\frac{\partial^2(\mathcal{K}\phi)}{\partial \phi_j \partial \phi_k}, \quad \forall \;\; j,k \\ &= 2\frac{\partial(\mathcal{K}\phi)}{\partial \phi_j}\frac{\partial(\mathcal{K}\phi)}{\partial \phi_k} + \left((\mathcal{K}\phi) - \phi_{\mathrm{m}}\right)\underbrace{\frac{\partial^2(\mathcal{K}\phi)}{\partial \phi_j \partial \phi_k}}_{=0} \\ &= 2(\nabla(\mathcal{K}\phi)) \times (\nabla(\mathcal{K}\phi))^T. \end{aligned} \tag{8.18}$$

In other words, the Hessian is the outer product of the gradient.

Two different initial guesses were chosen, which are named as run 1 (dashed line) and run 2 (solid line). The results are shown in Figure 8.5. The evolutions of the parameters and the posterior density are shown in Figure 8.5(a). It can be seen that both runs converge to the same solution which is the MAP estimate. The evolution of the bulk volume fraction as a function of the iteration number is shown in Figure 8.5(b). It can be seen that in both runs the algorithm constrains the bulk volume fraction to the known value which was 0.55. The main norm $\|V - \widetilde{U}(\phi)\|^2$ as a function of the iteration number is shown in Figure 8.5(c). It can be said that the norm is essentially zero after 30 iterations in both runs. It is important to note that it is not enough to ensure the convergence of this norm but also the convergence of the norm of the prior. Therefore, the prior norm $(\mathcal{K}\phi - \phi^*)^2$ also as a function of the iteration number is presented in Figure 8.5(d). It can be seen that the norm in the run 1 is zero in the beginning of the iteration. This is due to the fact that in this case the initial guess was chosen so that the bulk volume fraction is the known value 0.55 but the values of the parameters were incorrect being [0.3 0.8]. This can also be seen in Figures 8.5(a) and 8.5(b). In the beginning of the iteration the prior information on the bulk volume fraction is meaningless and therefore the information extracted from the voltage measurements have a crucial role. After about 10 iterations the prior information tends to pull the solution towards the correct solution. It can also be seen that the run 1 needs about 40 iterations in order to have the prior norm essentially zero.

Unknown background conductivity, Case 2

In this case, the background conductivity is assumed to be unknown. Therefore, three parameters have to be estimated, namely ϕ_1, ϕ_2 and the background conductivity σ_b. Estimation of these is based on the posterior density (7.7). In this case the prior density of the background conductivity is of the form

$$\pi(\sigma_b) \propto \exp\left(-\frac{1}{2\sigma_{\sigma_b}^2}(\sigma_b - \sigma_b^*)^2\right), \tag{8.19}$$

where σ_b^* is a prior guess of the background conductivity and $\sigma_{\sigma_b}^2$ is the variance of that. The known background conductivity σ_b^* was 0.5 and the variance of that 0.0224. First, the likelihood density is studied as in the case I. The likelihood density is shown in Figure 8.6. The same kind of elongation can be seen as in the case I. In this case the effect of the nonlinearity of the forward mapping can be seen better than in the Case 1.

Next the conditional mean, marginal densities, confidence limits and posterior correlation matrix were computed using Metropolis–Hastings algorithm. Therefore 100000 samples from the posterior density (7.7) were drawn. The starting point was [0.7 0.7 0.7]. Also in this case the burn-in period was chosen to be 100 samples. The acceptance ratio was 0.1405. The marginal densities, the conditional means and the 90 % confidence limits for each parameters are shown in Figure 8.7. It can be seen that also in this case the accuracy of the first parameter is better than the second one. Also it can be seen that the marginal density of the background conductivity is quite narrow which is due to the small variance of the prior density (8.19). It should also be noticed that the posterior variance of the background conductivity $\sigma^2_{\sigma_b}$ is smaller than the variance of the prior density, i.e. $\sigma^2_{\sigma_b,\text{post}} \leqslant \sigma^2_{\sigma_b}$. This result is known from literature, see for example [164, 88]. In Case 2, the posterior correlation matrix is as follows

$$R_{\phi,\sigma_b \mid V} = \begin{bmatrix} 1 & -0.8315 & 0.2236 \\ -0.8315 & 1 & -0.1809 \\ 0.2236 & -0.1809 & 1 \end{bmatrix}, \tag{8.20}$$

In this case the correlation between parameters ϕ_1 and ϕ_2 is stronger than in the case I. The correlations between ϕ_1 and σ_b, ϕ_2 and σ_b are almost the same but opposite in sign. This can be interpreted such that increase in the background conductivity can be compensated by increasing the value of the parameter ϕ_1 and by decreasing the value of the parameter ϕ_2. The results of this case are summarized in Table 8.2.

Table 8.2: Results of the Case 2. The AR is the acceptance ratio of the MCMC.

	ϕ_1	ϕ_2	σ_b [mS/cm]	AR
true	0.8000	0.3000	0.5000	
CM	0.7905	0.3068	0.4992	0.1405
variance	0.0203	0.0478	0.0219	

There is a question that arises after this example. If the background conductivity is known quite accurately and the stability and uniqueness problems arise when the background conductivity is parameterized, why is it not just assumed to be known to avoid these problems? The question is partly justified, but the Bayesian way of thinking is the natural way to take into account the uncertainty of the background conductivity. Moreover, when operating an industrial process, the background conductivity might change with respect to time and temperature.

8.4 Summary

In this chapter, a tomographic estimation of the material distribution within the process equipment was discussed and the particular prior model in which the bulk volume fraction is taken into account was proposed. The estimation was introduced from the statistical point of view. The properties of the method and the prior model was studied using two numerical simulations. On the basis of the simulations it can be said that the proposed prior model can assist in tomographic inversion. The simulations were quite simple ones and ultimate goal is the use of the proposed prior with more realistic volume fraction distributions. According to our preliminary tests with large number of the parameters, the proposed prior model alone is not sufficient and further prior information is needed.

An application in which the proposed prior model would be helpful is sedimentation process [32] mentioned in the introduction. The properties of solid-liquid suspensions can be characterized through observations of sedimentation. In this process the percentage fraction of the solid within a liquid is known quite accurately and that prior information can be taken into account. Moreover, there are three different regions in which the volume fraction values can be assumed to be homogeneous and hence the number of the parameters can be reduced.

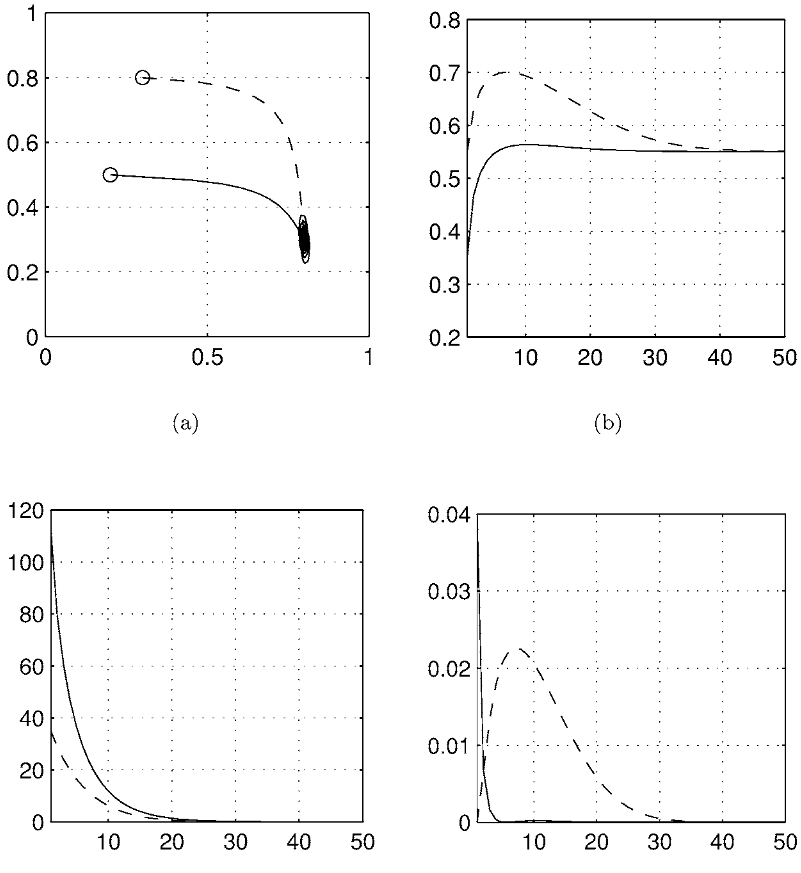

(a) (b)

(c) (d)

Figure 8.5: Solution of the Gauss–Newton estimation with two different initial guesses. (a) Evolution of the parameters and the posterior density. (b) Evolution of the bulk volume fraction. (c) Evolution of the main norm. (d) Evolution of the prior norm . In (a), the ordinate and abscissa are ϕ_1 and ϕ_2, respectively. In the (b), (c) and (d) the ordinate is the iteration number and the abscissa is the error.

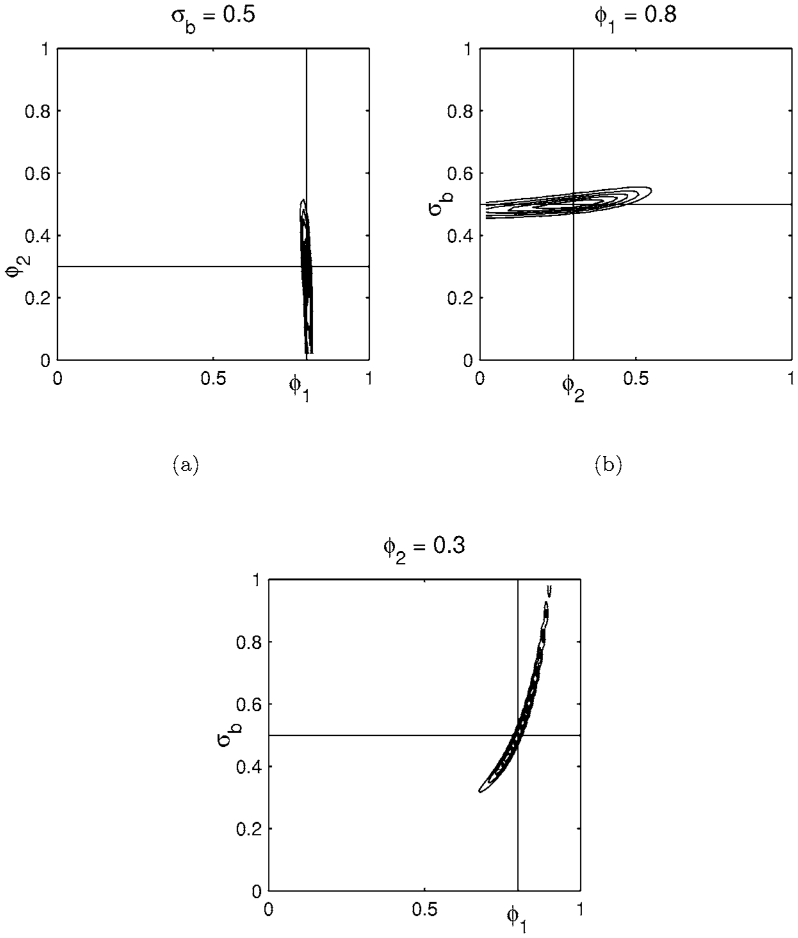

(a)

(b)

(c)

Figure 8.6: Likelihood density for the case II. (a) σ_b is constant (0.5), (b) ϕ_1 is constant (0.8), (c) ϕ_1 is constant (0.3). Vertical and horizontal lines denote correct values in each cases.

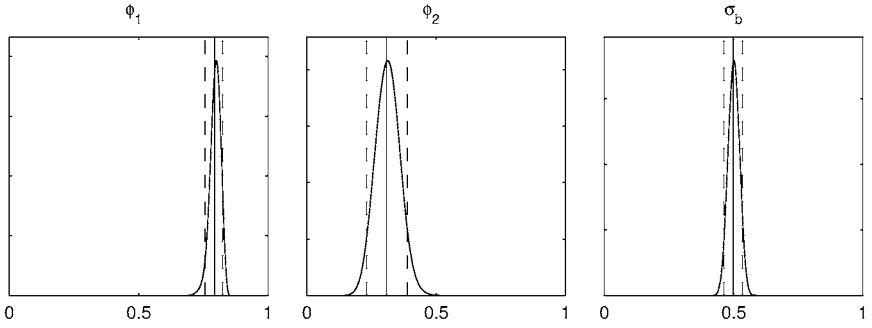

(a) (b) (c)

Figure 8.7: Marginal densities for estimated parameters. (a) ϕ_1, (b) ϕ_2 and (c) σ_b. The solid and dashed vertical lines denote the conditional means and 90 % credibility limits, respectively.

CHAPTER IX

Conclusions

In this thesis, novel estimation methods for electrical process tomography were studied. The methods were based on the statistical inversion theory. The developed methods were tested with numerical simulations and/or laboratory experiments in 2D and 3D.

In Chapters 2 and 3, the solid theoretical ground of this thesis was given. The basis of the statistical inversion theory was given in Chapter 2 in which the tomography technique was not yet specified and general notations therefore were used. The basic theory of the electrical impedance tomography technique, which was used in this thesis, was given in Chapter 3.

In Chapter 4, estimation of the electrode contact impedance was presented. The method was originally published in [69]. The method is based on the statistical inversion theory and especially MAP-estimates for the electrode contact impedances were computed. The proposed method was tested with laboratory experiments. On the basis of the experiments it seems that if the measurements with a uniform conducting medium can not be performed it might be hard to separate the contact impedances out from the internal impedivity distribution. This is due to ill-conditioning of the inverse problem. In this case the use of the voltage data measured on a current carrying electrodes and the wrong contact impedance values in the reconstruction of the absolute images would cause noisy images. This is specially the case in medical applications of EIT. In some cases, however, if some prior information for the contact impedances is available the estimation might be possible.

In Chapter 5, the effect of the known internal structures on the estimation of the conductivity and the method avoiding the effect were studied. The study was originally published in [72]. The method is based on the use of the a priori knowledge on the location and the conductivity of the structure. The knowledge can be taken into account in the construction of the Gaussian prior density distribution. The method was tested with 2D numerical simulations. It was shown by that in some conductive structure geometries the prior information of the structure may improve the estimation substantially. However, it was also shown that in a case in which the conductive structure encloses the region of interest by creating a low-resistivity path for current to flow, the proper reconstruction is impossible even with prior information of the structure. The proposed method has also been tested in nonstationary EIT in [98, 99]. In these papers both numerical simulations and laboratory experiments were studied. Also in [152] the approach was tested in nonstationary EIT using laboratory measurements.

In Chapter 6, the use of internal electrodes in EIT was studied. The study was originally presented in [70]. Also in [71] the use of the internal electrodes in the volume fraction estimation was studied. The presence of the internal electrodes was taken into account in the construction of the mesh. The approach was tested with 2D numerical simulations and laboratory experiments. The approach was also used in Chapter 7 in the case of volume fraction estimation. Simulations and laboratory experiments show that significant improvements in the estimation can be achieved using internal electrodes. The proposed method has also been tested in nonstationary EIT in [97].

In Chapter 7, the volume fraction estimation was studied. A part of this section was presented in [73]. The proposed method is based on the use of EIT and additional mapping between the conductivity and volume fraction distribution. The method was tested with a 3D numerical simulation. In this case the MAP-estimate was computed. The use of the internal electrodes for the volume fraction estimation in 2D was also studied. Laboratory experiment was also performed in which the estimation of the volume fraction distribution was based on the difference reconstruction scheme.

In Chapter 8, the novel prior model for the case in which information on the bulk volume fraction was taken into account was presented. The part of the chapter was originally presented in [73]. The method is based on the Gaussian prior density in which the information on the bulk volume fraction was encoded. The estimation method presented in Chapter 7 was used. The method was tested with simple illustrative numerical examples in 2D. In the examples MCMC-method was used to compute CM-estimate as well as the marginal densities and the confidence limits. Moreover, the MAP-estimate was computed. The simulations show that the proposed prior model can assist in the estimation. Due to the over simplified examples further studies have to be performed before the final conclusions of the method.

The methods presented in this thesis were tested with numerical simulations and laboratory experiments. A lot of further work remains although the applicability and usefulness of the methods were shown. All methods have to be tested with realistic laboratory experiments that are based on industrial interests. On the basis of these experiments the methods have to be upgraded such that interesting process quantities can be estimated as well. Furthermore, the final goal is to apply these methods in real industrial processes in process plants.

APPENDIX I

Proof of the equation (8.5)

Our starting point is the equation (8.4)

$$\phi_i = h(\phi_\mathcal{I}) + \underbrace{\frac{1}{\kappa_i}\phi_\mathrm{m}}_{\overline{\phi_\mathrm{m}}} . \tag{A.1}$$

The probability density of the parameter ϕ_i conditioned on $\phi_\mathcal{I}$ and $\overline{\phi_\mathrm{m}}$ is given by

$$\pi(\phi_i|\phi_\mathcal{I}, \overline{\phi_\mathrm{m}}) = \delta(\phi_i - h(\phi_\mathcal{I}) - \overline{\phi_\mathrm{m}}). \tag{A.2}$$

Let $\pi(\phi_\mathcal{I}, \overline{\phi_\mathrm{m}})$ denote the joint probability density of the $\phi_\mathcal{I}$ and $\overline{\phi_\mathrm{m}}$. Then the joint density of the $\phi_i, \phi_\mathcal{I}$ and $\overline{\phi_\mathrm{m}}$ can be written as

$$\begin{aligned} \pi(\phi_i, \phi_\mathcal{I}, \overline{\phi_\mathrm{m}}) &= \pi(\phi_i|\phi_\mathcal{I}, \overline{\phi_\mathrm{m}})\pi(\phi_\mathcal{I}, \overline{\phi_\mathrm{m}}) \\ &= \delta(\phi_i - h(\phi_\mathcal{I}) - \overline{\phi_\mathrm{m}})\pi(\phi_\mathcal{I}, \overline{\phi_\mathrm{m}}). \end{aligned} \tag{A.3}$$

To obtain the joint density of the parameters the variable ϕ_m is integrated out to get the prior density

$$\begin{aligned} \pi_\mathrm{pr}(\phi) = \pi(\phi_i, \phi_\mathcal{I}) &= \int_\mathbb{R} \delta(\phi_i - h(\phi_\mathcal{I}) - \overline{\phi_\mathrm{m}})\pi(\phi_\mathcal{I})\pi(\overline{\phi_\mathrm{m}})\mathrm{d}\overline{\phi_\mathrm{m}} \\ &= \pi(\phi_\mathcal{I})\pi_{\overline{\phi_\mathrm{m}}}(\phi_i - h(\phi_\mathcal{I})) \\ &= \pi(\phi_\mathcal{I})\pi(\phi_i|\phi_\mathcal{I}), \end{aligned} \tag{A.4}$$

where it is assumed that the $\pi(\phi_\mathcal{I}, \phi_\mathrm{m}) = \pi(\phi_\mathcal{I})\pi(\phi_\mathrm{m})$. The conditional density $\pi(\phi_i|\phi_\mathcal{I})$ can be obtained by the probability density of the bulk fraction. In the section 8.2 it is assumed that the probability density of the bulk volume fraction is truncated Gaussian distribution i.e. $\phi_\mathrm{m} \sim N_\mathrm{tr}(\phi_\mathrm{m}^*, \sigma_{\phi_\mathrm{m}}^2)$, hence the quantity $\overline{\phi_\mathrm{m}}$ is distributed as

$$\overline{\phi_\mathrm{m}} \sim N_\mathrm{tr}\left(\frac{1}{\kappa_i}\phi_\mathrm{m}^*, \frac{1}{\kappa_i^2}\sigma_{\phi_\mathrm{m}}^2\right). \tag{A.5}$$

The density of $\overline{\phi_{\mathrm{m}}}$ is therefore of the form

$$\pi(\overline{\phi_{\mathrm{m}}}) \propto \begin{cases} \exp(-\frac{\kappa_i^2}{2\sigma^2_{\phi_{\mathrm{m}}}}(\overline{\phi_{\mathrm{m}}} - \frac{\phi^*_{\mathrm{m}}}{\kappa_i})^2, & \overline{\phi_{\mathrm{m}}} \in [0,1]. \\ 0, & \text{otherwise.} \end{cases} \tag{A.6}$$

Now according to equation (A.4) the conditional density $\pi(\phi_i|\phi_{\mathcal{I}})$ is of the form

$$\pi(\phi_i|\phi_{\mathcal{I}}) = \pi_{\overline{\phi_{\mathrm{m}}}}(\phi_i - h(\phi_{\mathcal{I}})) \propto \begin{cases} \exp(-\frac{\kappa_i^2}{2\sigma^2_{\phi_{\mathrm{m}}}}(\phi_i - (\frac{\phi^*_{\mathrm{m}}}{\kappa_i} + h(\phi_{\mathcal{I}})))^2), & \phi_i \in [0,1]. \\ 0, & \text{otherwise.} \end{cases} \tag{A.7}$$

REFERENCES

[1] World Wide Web-page, http://www.cs.cornell.edu/home/vavasis/qmg-home.html.

[2] *Proceedings of 1st European Concerted Action on Process Tomography workshop*, Manchester, UK, 1992.

[3] *Proceedings of 2nd European Concerted Action on Process Tomography workshop*, Karlshure, Germany, 1993.

[4] *Proceedings of 3rd European Concerted Action on Process Tomography workshop*, Oporto, Portugal, 1994.

[5] *Proceedings of 4th European Concerted Action on Process Tomography workshop*, Bergen, Norway, 1995.

[6] *Proceedings of Frontiers in Industrial Process Tomography I*, CA, USA, 1995.

[7] *Proceedings of Frontiers in Industrial Process Tomography II*, Delft, Netherland, 1997.

[8] *Proceedings of 1st World Congress on Industrial Process Tomography*, Buxton, UK, 1999.

[9] *Proceedings of 2nd World Congress on Industrial Process Tomography*, Hannover, Germany, 2001.

[10] *Proceedings of 3rd World Congress on Industrial Process Tomography*, Banff, Canada, 2003.

[11] A. Adler and R. Guardo. Electrical impedance tomography: Regularized imaging and contrast detection. *IEEE Trans Med Imaging*, 15:170–179, 1996.

[12] G. Arfken. *Mathematical methods for physicists.* Academic Press, Inc., 3rd edition, 1985.

[13] S. R. Arridge. Optical tomography in medical imaging. *Inv Probl*, 15:R41–R93, 1999.

[14] S. Arulampalam, S. Maskell, N. Gordon, and T. Clapp. A tutorial on particle filters for on-line non-linear/non-Gaussian Bayesian tracking. *IEEE Trans Signal Processing*, 50(2):174 - 188, 2002.

[15] N.J. Avis and D.C. Barber. Adjacent or polar drive ?: Image reconstruction implications in electrical impedance tomography system employing filtered back projection. In *Proc 14th Int Conf IEEE Eng Med Biol Society*, pages 1689–1690, 1992.

[16] N.J. Avis and D.C. Barber. Image reconstruction using non-adjacent drive configurations. *Physiol Meas*, 16:A153–A160, 1994.

[17] S. Banisi, J. A. Finch, and A. R. Laplante. Electrical conductivity of dispersion: a review. *Minerals Eng*, 6(4):369–385, 1993.

[18] S. Banisi, J. A. Finch, and A. R. Laplante. Determination of holdup of flake-shaped particles in solid-water systems using conductivity. *Int J Miner Process*, 41:311–320, 1994.

[19] D.C. Barber and B.H. Brown. Applied potential tomography. *J Phys E: Sci Instrum*, 17:723–733, 1984.

[20] D.C. Barber and B.H. Brown. Recent developments in applied potential tomography. In Bacharac, editor, *Information processing in medical imaging*, pages 106–121. Martinus Nichoff, 1986.

[21] M. S. Beck, R. G. Green, A. B. Plaskowski, and A. L. Stott. Capacitance measurement applied to a pneumatic conveyor with very low solids loading. *Meas Sci Tech*, 1:561–564, 1990.

[22] M. S. Beck and A. Plaskowski. *Cross correlation flowmeters – their desing and application.* IOP publishing Ltd, 1987.

[23] M. A. Bennett, R. M. West, S. P. Luke, and R. A. Williams. The investigation of bubble column and foam processes using electrical capacitance tomography. *Minerals Eng*, 15:225–234, 2002.

[24] M. A. Bennett and R. A. Williams. Monitoring the operation of an oil/water separator using impedance tomography. *Minerals Eng*, 17:605–614, 2004.

[25] R. Binns, A. R. A. Lyons, A. J. Peyton, and W. D. N. Pritchard. Imaging molten steel flow profiles. *Meas Sci Tech*, 12:1132–1138, 2001.

[26] G. T. Bolton, C. W. Hooper, R. Mann, and E. H. Stitt. Flow distribution and velocity measurement in a radial flow fixed bed reactor using electrical resistance tomography. *Chem Eng Sci*, 59:1989–1997, 2004.

[27] K.G. Boone and D.S. Holder. Effect of skin impedance on image quality and variability in electrical impedance tomography: a model study. *Med Biol Eng Comput*, 34:351–354, 1996.

[28] A. Borsic. *Regularisation methods for imaging from electrical measurements.* PhD thesis, School of Engineering, Oxford Brookes University, 2002.

[29] W. Breckon. The problem of anisotropy in electrical impedance tomography. In *Proc 14th Int Conf IEEE Eng Med Biol Society*, pages 1734–1735, 1992.

[30] W.R. Breckon and M.K. Pidcock. Mathematical aspects of impedance imaging. *Clin Phys Physiol Meas, Suppl A*, 8:77–84, 1987.

[31] S.C. Brenner and L.R. Scott. *The Mathematical Theory of Finite Element Methods.* Springer, 1994.

[32] R. Burger and W. L. Wendland. Sedimentation and suspension flows: Historical perspective and some recent developments. *J Eng Math*, 41:101–116, 2001.

[33] J. E. Butler and R. T. Bonnecaze. Imaging of particle shear migration with electrical impedance tomography. *physics of fluids*, 11(8):1982–1994, 1999.

[34] A.P. Calderón. On an inverse boundary value problem. In W.H. Meyer and M.A. Raupp, editors, *Seminar on Numerical Analysis and its Applications to Continuum Physics*, pages 65–73, Rio de Janeiro, 1980. Brazilian Math. Society.

[35] J. Chaouki, F. Larachi, and M. P. Dudukivić. Nonivasive tomographic and velocimetric monitoring of multiphase flows. *Ind Eng Chem Res*, 36:4476–4503, 1997.

[36] M. Cheney and D. Isaacson. Distinguishability in impedance imaging. *IEEE Trans Biomed Eng*, 39:852–860, 1992.

[37] M. Cheney, D. Isaacson, and J. C. Newell. Electrical impedance tomography. *SIAM Rev*, 41:85–101, 1999.

[38] M. Cheney, D. Isaacson, J.C. Newell, S. Simske, and J. Goble. NOSER: An algorithm for solving the inverse conductivity problem. *Int J Imaging Systems and Technology*, 2:66–75, 1990.

[39] K.-S. Cheng, D. Isaacson, J.C. Newell, and D.G. Gisser. Electrode models for electric current computed tomography. *IEEE Trans Biomed Eng*, 36:918–924, 1989.

[40] K.-S. Cheng, S.J. Simske, D. Isaacson, J.C. Newell, and D. G. Gisser. Errors due to measuring voltage on current-carrying electrodes in electric current computed tomography. *IEEE Trans Biomed Eng*, 37:60–65, 1990.

[41] C. Cohen-Bacrie, Y. Goussard, and R. Guardo. Regularized reconstruction in electrical impedance tomography using a variance uniformization constraint. *IEEE Trans Med Imaging*, 16:562–571, 1997.

[42] J. L. Davidson, L. S. Ruffino, D. R. Stephenson, R. Mann, B. D. Grieve, and T. A. York. Three-dimensional electrical impedance tomography applied to a metal-walled filtration test platform. *Meas Sci Tech*, 15:2263–2274, 2004.

[43] C. Denyer. *Electronics for real-time and three-dimensional electrical impedance tomographs*. PhD thesis, Oxford Brooks University, Oxford, England, 1996.

[44] F. Dickin and M. Wang. Electrical resistance tomography for process tomography. *Meas Sci Tech*, 7:247–260, 1996.

[45] F. J. Dickin, B. S. Hoyle, A. Hunt, S. M. Huang O. Ilyas, C. Lenn, R. C. Waterfall, R. A. Williams C. G. Xie, and M. S. Beck. Tomographic imaging of industrial process equipment: techniques and applications. *IEE Proc-G*, 139(1):72–82, 1992.

[46] F. J. Dickin, R. A. Williams, and M. S. Beck. Determination of composition and motion of multicomponent mixtures in process vessels using electrical impedance tomography - I. Principles and process engineering applications. *Chem Eng Sci*, 48(10):1883–1897, 1993.

[47] D.C. Dobson and F. Santosa. Resolution and stability analysis of an inverse problem in electrical impedance tomography: dependence on the input current patterns. *SIAM J Appl Math*, 54:1542–1560, 1994.

[48] T. Dyakowski, R. B. Edwards, C. G. Xie, and R. A. Williams. Application of capacitance tomography to gas-solid flows. *Chem Eng Sci*, 52(13):2099–2110, 1997.

[49] T. Dyakowski, S. P. Luke, K. L. Ostrowski, and R. A. Williams. On-line monitoring of dense phase flow using real time dielectric imaging. *Powder technology*, 104:287–295, 1999.

[50] T. Dyakowski, S. J. Wang, D. Deldart, and M. S. Beck. Tomographic studies of flow patterns within a circulating fluidized bed. *Chem Eng Comm*, 175:117–130, 1999.

[51] P.M. Edic, D. Isaacson, G.J. Saulnier, H. Jain, and J.C. Newell. An iterative Newton-Raphson method to solve the inverse admittivity problem. *IEEE Trans Biomed Eng*, 45:899–908, 1998.

[52] E. O. Etuke and R. T. Bonnecaze. Measurement of angular velocities using electrical impedance tomography. *Flow Meas Instr*, 9:159–169, 1998.

[53] B.M. Eyüboglu and T.C. Pilkington. Intracavity electrical impedance tomography. In *12th Ann Int Conf IEEE Eng Med Biol Soc*, page 0130, 1990.

[54] Y. S. Fangary, R. A. Williams, W. A. Neil, and J. Bond I. Faulks. Application of electrical resistance tomography to detect deposition in hydraulic conveying systems. *Powder technology*, 95:61–66, 1999.

[55] A. E. Gelfand and A. F. M. Smith. Sampling based approaches to calculating

marginal densities. *J Amer Statist Assoc*, 85:398–409, 1990.

[56] S. Geman and D. Geman. Stochastic relaxation, Gibbs distributions and the Bayesian restoration of images. *IEEE Trans Pattern Anal Mach Intell*, 6:721–741, 1984.

[57] D. L. George, K. A. Shollenberger, J. R. Torczynski, T. J. O'Hern, and S. L. Ceccio. Three-phase material distribution measurements in a vertical flow using gamma-densitometry tomography and electrical-impedance tomography. *Int J Multiphase Flow*, 27:1903–1930, 2001.

[58] D.B. Geselowitz. An application of electrocardiographic lead theory to impedance pletysmography. *IEEE Trans Biomed Eng*, 18:38–41, 1971.

[59] S. J. Gibbs and L. D. Hall. What roles are there for magnetic resonance imaging in process tomography ? *Meas Sci Tech*, 7:827–837, 1996.

[60] W.R. Gilks, S. Richardson, and D.J. Spiegelhalter. *Markov Chain Monte Carlo in Practice*. Chapmann & Hall, 1996.

[61] D.G. Gisser, D. Isaacson, and J.C. Newell. Electric current computed tomography and eigenvalues. *SIAM J Appl Math*, 50:1623–1634, 1990.

[62] S. Gomez, M. Ono, C. Gamio, and A. Fraguela. Reconstruction of capacitance tomography images of simulated two-phase regimes. *Appl Num Math*, 46:197–208, 2003.

[63] A. Greenleaf, M. Lassas, and G. Uhlmann. Anisotropic conductivities that cannot be detected by EIT. *Physiol Meas*, 24:413–419, 2003.

[64] H. Griffiths. Magnetic inductance tomography. *Meas Sci Tech*, 12:1126–1131, 2001.

[65] C. W. Groetsch. *Inverse Problems in the Mathematical Sciences*. Vieweg, 1993.

[66] C. J. Grootveld. *Measuring & modeling of concentrated settling suspensions using electrical impedance tomography*. PhD thesis, Delft University of Technology, 1996.

[67] J. A. Gutierrez, T. Dyakowski, M. S. Beck, and R. A. Williams. Using electrical impedance tomography for controlling hydrocyclone underflow discharge. *Powder technology*, 108:180–184, 2000.

[68] W. K. Hastings. Monte Carlo sampling methods using Markov chains and their applications. *Biometrika*, 57:97–109, 1970.

[69] L. M. Heikkinen and T. Vilhunen R. M. West M. Vauhkonen J. P. Kaipio. Simultaneous reconstruction of electrode contact impedances and internal electrical properties, part II: Laboratory experiments. *Meas Sci Tech*, 13:1855 – 1861, 2002.

[70] L. M. Heikkinen, M. Vauhkonen, T. Savolainen, and J. P. Kaipio. Modelling of internal structures and electrodes in electrical process tomography. *Meas Sci Tech*, 12:1012–1019, 2001.

[71] L. M. Heikkinen, M. Vauhkonen, T. Savolainen, and J. P. Kaipio. Utilising internal electrodes in volume fraction estimation by electrical process tomography. In *Proceedings of 2nd world congress on industrial process tomography*, pages 191–197, 2001.

[72] L. M. Heikkinen, M. Vauhkonen, T. Savolainen, K. Leinonen, and J.P. Kaipio. Electrical process tomography with known internal structures and resistivities. *Inv Prob Eng*, 9:431–454, 2001.

[73] L. M. Heikkinen, R. W. West, and M. Vauhkonen. Utilizing prior information in the estimation of volume fraction distribution. *Int J Numerical Methods Engr*, 2005 (in press).

[74] G. F. Hewitt. *Measurement of two phase flow parameters*. Academic press, London, 1978.

[75] P. J. Holden, M. Wang, R. Mann, F. J. Dickin, and R. B. Edwards. Imaging stirred-

vessel macromixing using electrical resistance tomography. *AIChE J*, 44(4):780–790, 1998.

[76] P. Hua, J.G. Webster, and W.J. Tompkins. Effect of the measurement method on noise handling and image quality of EIT imaging. In *Proc 9th Int Conf IEEE Eng Med Biol Society*, pages 1429–1430, 1987.

[77] P. Hua, J.G. Webster, and W.J. Tompkins. A regularised electrical impedance tomography reconstruction algorithm. *Clin Phys Physiol Meas, Suppl A*, 9:137–141, 1988.

[78] P. Hua, E.J. Woo, J.G. Webster, and W.J. Tompkins. Iterative reconstruction methods using regularization and optimal current patterns in electrical impedance tomography. *IEEE Trans Med Imaging*, 10:621–628, 1991.

[79] P. Hua, E.J. Woo, J.G. Webster, and W.J. Tompkins. Finite element modeling of electrode–skin contact impedance in electrical impedance tomography. *IEEE Trans Biomed Eng*, 40:335–343, 1993.

[80] P. Hua, E.J Woo, J.G. Webster, and W.J. Tompkins. Using compound electrodes in electrical impedance tomography. *IEEE Trans Biomed Eng*, 40:29–34, 1993.

[81] Y. Hua, S. FuQun, X. Hui, and W. Shi. Three-dimensional analysis of electrical capacitance tomography sensing fields. *Meas Sci Tech*, 10:717–725, 1999.

[82] S. M. Huang, R. G. Green, A. Plaskowski, and M. S. Beck. A high frequency stray-immune capacitance transducer based on the charge transfer principle. *IEEE Trans on Instrum Meas*, 37(3):368–273, 1988.

[83] S. M. Huang, C. G. Xie, R. Thorn, D. Snowden, and M. S. Beck. Design of sensor electronics for electrical capacitance tomography. *IEE Proc-G*, 139(1):83–88, 1992.

[84] D. Isaacson. Distinguishability of conductivities by electric current computed tomography. *IEEE Trans Med Imaging*, 5:91–95, 1986.

[85] O. C. Jones, J. T. Lin, and L. Ovacik. Investigation of electrical impedance imaging relative to two-phase, gas-liquid flows. *Chem Eng Comm*, 118:299–325, 1992.

[86] O. C. Jones, J-T. Lin, L. Ovacik, and H. Shu. Impedance imaging relative to gas-liquig systems. *Nucl Eng desing*, 141:159–176, 1993.

[87] J. P. Kaipio, V. Kolehmainen, E. Somersalo, and M. Vauhkonen. Statistical inversion and Monte Carlo sampling methods in electrical impedance tomography. *Inv Probl*, 16:1487–1522, 2000.

[88] J. P. Kaipio and E. Somersalo. *Statistical and Computational Inverse Problems.* Applied Mathematical Sciences. Springer, 2004.

[89] J.P. Kaipio, V. Kolehmainen, M. Vauhkonen, and E. Somersalo. Inverse problems with structural prior information. *Inv Probl*, 15:713–729, 1999.

[90] J.P. Kaipio, A. Seppänen, E. Somersalo, and H. Haario. Statistical inversion approach for optimizing current patterns in EIT. In *3rd World Congress on Industrial Process Tomography, Banff, Canada*, pages 683–688, 2003.

[91] J.P. Kaipio, A. Seppänen, E. Somersalo, and H. Haario. Posterior covariance related optimal current patterns in electrical impedance tomography. *Inv Probl*, 20(3):919–936, 2004.

[92] J.P. Kaipio, E. Somersalo, P.A. Karjalainen, and M. Vauhkonen. Recursive estimation of fast impedance changes in electrical impedance tomography and a related problem. In R.L. Barbour, M.J. Carvlin, and M.A. Fiddy, editors, *Proc SPIE's 42nd Annual Meeting, Computational, experimental and numerical methods for solving ill-posed inverse imaging problems: medical and nonmedical applications*, pages 208–216, San Diego, USA, June 27-August 1, 1997. SPIE.

[93] A. C. Kak and M. Slaney. *Principles of computerized tomographic imaging.* IEEE

Press, 1988.

[94] A. Kemoun, B. C. Ong P. Gupta, M. H. Al-Dahhan, and M. P. Ducukovic. Gas holdup in bubble columns at elevated pressure via computed tomography. *Int J Multiphase Flow*, 27:929–946, 2001.

[95] S. H. Khan and F. Abdullah. Finite element modelling of electrostatic fields in process tomography capacitive electrode systems for flow response evaluation. *IEEE Trans on magnetics*, 29(6):2437–2439, 1993.

[96] S. H. Khan and F. Abdullah. Finite element modelling of multielectrode capacitive systems for flow imaging. *IEE Proc-G*, 140(3):216–222, 1993.

[97] K. Y. Kim, S. I. Kang, S. Kim, M. C. Kim, C. I. Kang, and J. Lee. Dynamic electrical impedance imaging of binary-mixture fields with external and internal electrodes. *Inv Prob Eng*, 12(5):471–483, 2004.

[98] K.Y. Kim, S.I. Kang, M.C. Kim, S. Kim, Y.J. Lee, and M. Vauhkonen. Dynamic image reconstruction in electrical impedance tomography with known internal structures. *IEEE Trans Magn*, 38:1301–1304, 2002.

[99] K.Y. Kim, S.I. Kang, M.C. Kim, S. Kim, Y.J. Lee, and M. Vauhkonen. Dynamic electrical impedance tomography with known internal structures. *Inv Prob Eng*, 11:1–19, 2003.

[100] K.Y. Kim, B.S. Kim, M.C. Kim, Y.J. Lee, and M. Vauhkonen. Image reconstruction in time-varying electrical impedance tomograhy based on the extended Kalman filter. *Measur Sci Technol*, 12:1032–1039, 2001.

[101] R.V. Kohn and M. Vogelius. Determining conductivity by boundary measurements II. Interior results. *Commun Pure Appl Math*, 38:643–667, 1985.

[102] A. Köksal and B. M. Eyüboğlu. Determination of optimum injected current paterns in electrical impedance tomography. *Physiol Meas*, 16:A99–A109, 1995.

[103] V. Kolehmainen. Static electrical impedance tomography (In Finnish). Master's thesis, University of Kuopio, Department of Applied Physics, 1997.

[104] V. Kolehmainen. *Novel Approaches to Image Reconstruction in Diffusion Tomography.* PhD thesis, University of Kuopio, Kuopio, Finland, 2001.

[105] V. Kolehmainen, M. Vauhkonen, P.A. Karjalainen, and J.P. Kaipio. Assessment of errors in static electrical impedance tomography with adjacent and trigonometric current patterns. *Physiol Meas*, 18:289–303, 1997.

[106] C.J. Kotre. A sensitivity coefficient method for the reconstruction of electrical impedance tomograms. *Clin Phys Physiol Meas, Suppl A*, 10:275–281, 1989.

[107] O. A. Laudal and R. Piene, editors. *The legacy of Niels Henrik Abel.* Springer, 2004.

[108] C.L. Lawson and R.J. Hanson. *Solving Least Squares Problems.* SIAM, 1995.

[109] J.M. Lee and G. Uhlmann. Determining anisotropic real-analytic conductivities by boundary measurements. *Commun Pure Appl Math*, 42:1097–1112, 1989.

[110] S. Levy. *Two-phase flow in complex systems.* John Wiley & Sons, inc., 1999.

[111] W. R. B. Lionheart. EIT reconstruction algorithms: pitfalls, challenges and recent developments. *Physiol Meas*, 25:125–142, 2004.

[112] W.R.B. Lionheart, J.P. Kaipio, and C. N. McLeod. Generalized optimal current patterns and electrical safety in EIT. *Physiol Meas*, 22:85–90, 2001.

[113] P. Lorrain and D. R. Corson. *Electromagnetism: principles and applications.* W.H. Freeman and Company, 2nd edition, 1990.

[114] G. P. Lucas, J. Cory, R. C. Waterfall, W. W. Loh, and F. J. Dickin. Measurement of the solids volume fraction and velocity distribution in solids-liquid flows using dual-plane electrical resistance tomography. *Flow Meas Instr*, 10:249–258, 1999.

[115] S. P. Luke and R. A. Williams. Industrial applications of electrical tomography to solids conveying. *Meas Cont*, 30:201–205, 1997.

[116] G. M. Lyon and J. P. Oakley. A simulation study of sensitivity in stirred vessel electrical impedance tomography. In M. S. Beck, E. Campogrande, M. Morris, R. A. Williams, and R. C. Waterfall, editors, *Tomography techniques for process design and operation*, pages 137–146, Southampton UK, 1993. Computational Mechanics Publications.

[117] Y. Ma, Z. Zheng, L. Xu, X. Liu, and Y. Wu. Application of electrical resistance tomography system to monitor gas/liquid two-phase flow in a horozontal pipe. *Flow Meas Instr*, 12:259–265, 2001.

[118] Y. T. Makkawi and P. C. Wright. Fluidization regimes in a convetional fluidized bed chatacterized by means of electrical capacitance tomography. *Chem Eng Sci*, 57:2411–2437, 2002.

[119] Y. T. Makkawi and P. C. Wright. Tomographic analysis of dry and semi-wet bed fluidization: the effect of small liquid loading and particle size on the bubbling behaviour. *Chem Eng Sci*, 59:201–213, 2004.

[120] R. Mann, F. J. Dickin, M. Wang, T. Dyakowski, R. A. Williams, R. B. Edwards, A. E. Forrest, and P. J. Holden. Application of electrical resistance tomography to interrogate mixing processes at plant scale. *Chem Eng Sci*, 52(13):2087–2097, 1997.

[121] R. Mann and M. Wang. Electrical process tomography: Simple and inexpensive techniques for process tomography. *Meas Cont*, 30:206–211, 1997.

[122] R. Mann, M. Wang, A. E. Forrest, P. J. Holden F. J. Dickin, T. Dyakowski, and R. B. Edwards. Gas-liquid and miscible liquid mixing in a plant-scale vessel monitored using electrical resistance tomography. *Chem Eng Comm*, 175:39–48, 1999.

[123] R. Mann, R. A. Williams, T. Dyakowski, F. J. Dickin, and R. B. Edwards. Development of mixing models using electrical resistance tomography. *Chem Eng Sci*, 52(13):2073–2085, 1997.

[124] T. Martin and J. Idier. A FEM based nonlinear MAP estimator in electrical impedance tomography. In *Proceedings IEEE ICIP'97*, 1997.

[125] J. C. Maxwell. *A Treatise of Electricity and Magnetism*, volume 1. Oxford university press, London, 3rd edition, 1892.

[126] E.T. McAdams, J. Jossinet, A. Lackermeier, and F. Risacher. Factors affecting electrode-gel-skin interface impedance in electrical impedance tomography. *Med Biol Eng Comput*, 34:397–408, 1996.

[127] H. McCann and D. M. Scott, editors. *Proceedings of SPIE, Process imaging for automatic control*, Boston, USA, 2000. SPIE.

[128] J.L. Melsa and D.L. Cohn. *Decision and Estimation Theory*. McGraw-Hill, 1978.

[129] R. S. Meredith and C. W. Tobias. *Advances in electrochemistry and electrichemical engineering*, chapter II. Conduction in heterogeneous systems, pages 15–47. New York, NY: Wiley, 1962.

[130] P. Metherall. *Three Dimensional Electrical Impedance Tomography of the Human Thorax*. PhD thesis, University of Sheffield, 1998.

[131] P. Metherall, D.C. Barber, R.H. Smallwood, and B.H. Brown. Three-dimensional electrical impedance tomography. *Nature*, 380:509–512, 1996.

[132] N. Metropolis, A. W. Rosenbluth, M. N. Rosenbluth, A. H. Teller, and E. Teller. Equations of state calculations by fast computing machine. *J Chem Phys*, 21:1087–1091, 1953.

[133] R. E. Miller. *Optimization. Foundations and applications.* John Wiley & Sons, Inc, New York, 2000.

[134] A.I. Nachman. Global uniqueness for a two-dimensional inverse boundary value problem. *Annals of Math*, 143:71–96, 1996.

[135] P. Neittaanmäki, M. Rudnicki, and A. Savini. *Inverse Problems and optimal shape desing in electricity and magnetism.* Oxford: Oxford University Press, 1996.

[136] J. P. Oakley and M. S. Bair. A mathematical model for the multi-electrode capacitance sensor. *Meas Sci Tech*, 6:1617–1630, 1995.

[137] G.P. Otto and W.C. Chew. Time-harmonic impedance tomography using the T-matrix method. *IEEE Trans Med Imaging*, 13:508–516, 1994.

[138] A. Papoulis. *Probability, Random Variables and Stochastic Processes.* McGraw-Hill, 1984.

[139] K. Paulson, W. Lionheart, and M. Pidcock. POMPUS: an optimized EIT reconstruction algorithm. *Inverse Problems*, 11:425–437, 1995.

[140] A. J. Peyton, Z. Z. Yu, G. Lyon, S. Al-Zeibak J. Ferreira, J. Velez, F. Linhares, A. R. Borges, H. L. Xiong, N. H. Saunders, and M. S. Beck. An overview of electromagnetic inductance tomography: description of three different systems. *Meas Sci Tech*, 7:261–271, 1996.

[141] M. Pidcock, S. Ciulli, and S. Ispas. Singularities of mixed boundary value problems in electrical impedance tomography. *Physiol Meas*, 16:A213–A218, 1995.

[142] P. A. T. Pinheiro, W. W. Loh, and F. J. Dickin. Smoothness-constrained inversion for two-dimensional electrical resistance tomography. *Meas Sci Tech*, 8:293–302, 1997.

[143] P. A. T. Pinheiro, W. W. Loh, M. Wang, R. Mann, and R. C. Waterfall. Three-dimensional electrical resistance tomography in a stirred mixing vessel. *Chem Eng Comm*, 175:25–38, 1999.

[144] A. Plaskowski, M. S. Beck, R. Thorn, and T. Dyakowski. *Imaging industrial flows: applications of electrical process tomography.* IOP publishing Ltd, 1995.

[145] N. Polydorides. *Image reconstruction algorithms for soft-field tomography.* PhD thesis, UMIST,University of Manchester Institute of Science and Technology, 2002.

[146] N. Polydorides and W. R. B. Lionheart. A Matlab toolkit for three-dimensional electrical impedance tomography: a contribution to the Electrical Impedance and Diffuse Reconstruction Software project. *Meas Sci Tech*, 13(12):1871–1883, 2002.

[147] C. R. Rao. *Linear statistical inference and its applications.* Wiley, New York, 1973.

[148] F. Santosa and M. Vogelius. A backprojection algorithm for electrical impedance imaging. *SIAM J Appl Math*, 50:216–243, 1990.

[149] T. Savolainen, L. M. Heikkinen, M. Vauhkonen, and J. P. Kaipio. A modular, adaptive electrical impedance tomography system. In *Proceedings of 3nd world congress on industrial process tomography*, pages 50–55, 2003.

[150] T. Savolainen, J.P. Kaipio, M. Vauhkonen, and P.A. Karjalainen. An EIT measurement system for experimental use. *Rev Sci Instr*, 67:3605–3609, 1996.

[151] J. M. Scaife, R. C. Tozer, and I. L. Freeston. Conductivity and permittivity images from an induced current electrical impedance tomography system. *IEE Proc, Sci Meas Technol*, 141:356–362, 1994.

[152] A. Seppänen, L. Heikkinen, T. Savolainen, E. Somersalo, and J.P. Kaipio. An experimental evaluation of state estimation with fluid dynamical models in process tomography. In *3rd World Congress on Industrial Process Tomography, Banff, Canada*, pages 541–546, 2003.

[153] A. Seppänen, M. Vauhkonen, E. Somersalo, and J.P. Kaipio. State space models

in process tomography – approximation of state noise covariance. *Inv Prob Eng*, 9:561–585, 2001.

[154] A. Seppänen, M. Vauhkonen, E. Somersalo, and J.P. Kaipio. Inference of velocity fields based on tomographic measurements in process industry. In *4th international conference on inverse problems in engineering: theory and practice, Angra dos Reis, Rio de Janeiro, Brazil*, pages 453–460, 2002.

[155] A. Seppänen, M. Vauhkonen, P.J. Vauhkonen, E. Somersalo, and J.P. Kaipio. Fluid dynamical models and state estimation in process tomography: Effect due to inaccuracies in flow fields. *J Electr Imaging*, 10(3):630–640, 2001.

[156] A. Seppänen, M. Vauhkonen, P.J. Vauhkonen, E. Somersalo, and J.P. Kaipio. State estimation in three dimensional impedance imaging – Use of fluid dynamical evolution models. In *Proceedings of 2nd World Congress on Industrial Process Tomography*, pages 198–206, 2001.

[157] A. Seppänen, M. Vauhkonen, P.J. Vauhkonen, E. Somersalo, and J.P. Kaipio. State estimation with fluid dynamical evolution models in process tomography – an application to impedance tomography. *Inv Probl*, 17:467–484, 2001.

[158] D. S. Sivia. *Data analysis, A Bayesian tutorial.* Oxford University press, 1996.

[159] E. Somersalo, M. Cheney, and D. Isaacson. Existence and uniqueness for electrode models for electric current computed tomography. *SIAM J Appl Math*, 52:1023–1040, 1992.

[160] J. Sylvester and G. Uhlman. The Dirichlet to Neuman map and applications. In D. Colton, R. Ewing, and W. Rundell, editors, *Inverse problems in partial differential equations*, chapter 8, pages 101–139. SIAM, Philadelphia, 1990.

[161] H. S. Tapp and A. J. Payton. A state of art review if electromagnetic tomography. In *3rd Congress on Industrial Process Tomography*, pages 340–346, Banff, Canada, 2003.

[162] H. S. Tapp, A. J. Peyton, E. K. Kemsley, and R. H. Wilson. Chemical engineering applications of electrical process tomography. *Sensors and actuators B*, 98:17–24, 2003.

[163] A. Tarantola. *Inverse Problem Theory.* Elsevier, 1987.

[164] A. Tarantola and B. Valette. Inverse problems = quest for information. *J Geophys*, pages 159–170, 1982.

[165] M. Tarvainen, M. Vauhkonen, T. Savolainen, and J.P. Kaipio. Boundary element method and internal electrodes in electrical impedance tomography. *Int J Numerical Methods Engr*, 50:809–824, 2001.

[166] A. N. Tihonov. Regularization of incorrectly posed problems. *Soviet Mathematics - Doklady*, 4:1624–1627, 1963.

[167] A. Uribe-Sales, C. O. Gomez, and J. A. Finch. A conductivity technique for gas and solids holdup determination in three-phase reactors. *Chem Eng Comm*, 49(1):1–10, 1994.

[168] M. Vauhkonen. *Electrical Impedance Tomography and Prior Information.* PhD thesis, University of Kuopio, Kuopio, Finland, 1997.

[169] M. Vauhkonen, P.A. Karjalainen, and J.P. Kaipio. A Kalman filter approach to track fast impedance changes in electrical impedance tomography. *IEEE Trans Biomed Eng*, 45:486–493, 1998.

[170] M. Vauhkonen, W.R.B. Lionheart, L.M. Heikkinen, P.J. Vauhkonen, and J.P. Kaipio. A MATLAB package for the EIDORS project to reconstruct two-dimensional EIT images. *Physiol Meas*, 22:107–111, 2001.

[171] P.J. Vauhkonen. *Image Reconstruction in Three-Dimensional Electrical Impedance*

Tomography. PhD thesis, University of Kuopio, Kuopio, Finland, 2004.

[172] P.J. Vauhkonen, M. Vauhkonen, and J.P. Kaipio. Fixed-lag smoothing and state estimation in dynamic electrical impedance tomography. *Int J Numerical Methods Engr*, 50:2195–2209, 2001.

[173] P.J. Vauhkonen, M. Vauhkonen, T. Mäkinen, P.A. Karjalainen, and J.P. Kaipio. Dynamic electrical impedance tomography – phantom studies. *Inv Prob Eng*, 8:495–510, 2000.

[174] U. Parasu Veera, A. W. PatWardhan, and J. B. Joshi. Measurement of gas hold-up profiles in stirred tank by gamma ray attenuation method. *Trans IChemE*, 79(A):648–688, 2001.

[175] T. Vilhunen, J.P. Kaipio, P.J. Vauhkonen, T. Savolainen, and M. Vauhkonen. Simultaneous reconstruction of electrode contact impedances and internal electrical properties: I. theory. *Measur Sci Technol*, 13:1848–1854, 2002.

[176] C. R. Vogel. *Computational Methods for Inverse Problems.* Frontiers in applied mathematics. SIAM, 2002.

[177] M. Wang. Inverse solutions for electrical impedance tomography based on conjugate gradients methods. *Meas Sci Tech*, 13:101–117, 2002.

[178] M. Wang and J. J. Cilliers. Detecting non-uniform foam density using electrical resistance tomography. *Chem Eng Sci*, 54:707–712, 1999.

[179] M. Wang, A. Dorward, D. Vlaev, and R. Mann. Measurements of gas-liquid mixing in a stirred vessel using electrical resistance tomography (ERT). *Chem Eng J*, 77:93–98, 2000.

[180] W. Warsito and L.-S.Fan. ECT imaging of three-phase fluidized bed based on three-phase capacitance model. *Chem Eng Sci*, 58:823–832, 2003.

[181] R. C. Waterfall, R. He, and C. M. Beck. Visualizing combustion using electrical impedance tomography. *Chem Eng Sci*, 52(13):2129–2138, 1997.

[182] J.G. Webster. *Electrical Impedance Tomography.* Adam Hilger, Bristol, UK, 1990.

[183] R. M. West, X. Jia, and R. A. Williams. Quantification of solid-liquid mixing using electrical resistance and positron emission tomography. *Chem Eng Comm*, 175:71–97, 1999.

[184] R. A. Williams. Tomographic imaging for modelling and control of mineral processes. *Chem Eng J*, 59:71–85, 1995.

[185] R. A. Williams and M. S. Beck. *Process Tomography: Principles, Techniques and Applications.* Butterworth-Heinemann, Oxford, 1995.

[186] R. A. Williams and M. S Beck, editors. *Process Tomography: Principles, Techniques and Applications*, chapter 6, Mutual inductance tomography. Butterworth-Heinemann, Oxford, 1995.

[187] R. A. Williams, F. J. Dickin, J. A. Gutiérrez, T. Dyakowski, and M. S. Beck. Using electrical impedance tomography for controlling hydrocyclone underflow discharge. *Control Eng Practice*, 5(2):253–256, 1997.

[188] R. A. Williams, T. Dyakowski, C. G. Xie, S. P. Luke, P. J. Gregory, R. B. Edwards, F. J. Dickin, and L. F. Gate. Industrial measurement and control of particulate processes using electrical tomography. In *1st European Concerted Action on Process Tomography workshop*, pages 3–15, Manchester, UK, 1995.

[189] R. A. Williams, X. Jia, and S. L. McKee. Development of slurry mixing models using resistance tomography. *Powder technology*, 87:21–27, 1996.

[190] E.J. Woo, P.Hua, J.G. Webster, W.J. Tompkins, and R. Pallas-Areny. Skin impedance measurements using simple and compound electrodes. *Med Biol Eng Comput*, 30:97–102, 1992.

[191] C. G. Xie, S. M. Huang, B. S. Hoyle, R. Thorn, C. Lenn, D. Snowden, and M. S. Beck. Electrical capacitance tomography for flow imaging: system model for development of image reconstruction algorithms and desing of primary sensors. *IEE Proc-G*, 139(1):89–98, 1992.

[192] C. G. Xie, S. M. Huang, C. P. Lenn, A. L. Stott, and M. S. Beck. Experimental evalutation of capacitance tomoghraphic flow imaging systems using physical models. *IEE Proc, Circuit Device Syst.*, 141(5):357–368, 1994.

[193] C. G. Xie, A. Plaskowski, and M. S. Beck. 8-electrode capacitance system for two-component flow identification, Part 2: Flow regime identification. *IEE Proc*, 136(4):184–190, 1989.

[194] C. G. Xie, A. Plaskowski, and M. S. Beck. 8-electrode capacitance system for two-component flow indentification, Part 1: Tomographic flow imaging. *IEE Proc*, 136(4):173–183, 1989.

[195] C. G. Xie, N. Reinecke, M. S. Beck, D. Mewes, and R. A. Williams. Electrical tomography techniques for process engineering applications. *Chem Eng J*, 56:127–133, 1995.

[196] C. G. Xie, A. L. Stott, A. Plaskowski, and M. S. Beck. Design of capacitance electrodes for concentration measurement of two-phase flow. *Meas Sci Tech*, 1:65–78, 1990.

[197] W. Q. Yang. Calibration of capacitance tomography system: a new method for setting system measurement range. *Meas Sci Tech*, 7:863–867, 1996.

[198] W. Q. Yang, M. S. Beck, and M. Byars. Electrical capacitance tomography - from desing to applications. *Meas Cont*, 28:261–266, 1995.

[199] W. Q. Yang, A. L. Scott, and M. S. Beck. High frequency and high resolution capacitance measuring circuit for process tomography. *IEE Proc, Circuit Device Syst.*, 141(3):215–219, 1994.

[200] W. Q. Yang, D. M. Spink, J. C. Gamio, and M. S. Beck. Sensitivity distributions of capacitance tomography sensors with parallel field excitation. *Meas Sci Tech*, 8:562–569, 1997.

[201] W. Q. Yang, A. L. Stott, and M. S. Beck. Development of capacitance tomographic imaging systems for oil pipeline measurements. *Rev Sci Instrum*, 66(8):4326–4332, 1995.

[202] T. York. Status of electrical tomography in industrial applications. *J Electr Imaging*, 10(3):608–619, 2001.

[203] M. Yu and D. E. Dougherty. Modified total variation methods for three-dimensional electrical resistance tomography inverse problems. *Water Resources Research*, 36(7):1653–1664, 2000.

Kuopio University Publications C. Natural and Environmental Sciences

C 171. Rautiala, Sirpa. Microbial exposure in remediation work.
2004. 74 p. Acad. Diss.

C 173. Tarvainen, Mika. Estimation Methods for Nonstationary Biosignals.
2004. 138 p. Acad. Diss.

C 174. Yppärilä, Heidi. Depth of sedation in intensive care patients. A neuropsysiological study.
2004. 104 p. Acad. Diss.

C 175. Sohlberg, Antti. Molecular small animal imaging with pinhole single-photon emission computed tomography.
2004. 104 p. Acad. Diss.

C 176. Kumlin, Timo. Studies on cancer-related effects of 50 Hz magnetic fields.
2004. 64 p. Acad. Diss.

C 177. Seppänen, Kari. Does mercury promote lipid peroxidation?: in vivo and in vitro studies concerning mercury and selenium in lipid peroxidation and coronary heart disease.
2004. 49 p. Acad. Diss.

C 178. Riikonen, Johanna. Modification of the growth, photosynthesis and leaf structure of silver birch by elevated CO2 and O3.
2004. 126 p. Acad. Diss.

C 179. Frank, Christian. Functional profiling of the xenobiotic nuclear receptors CAR and PXR.
2004. 87 p. Acad. Diss.

C 180. Rytkönen, Esko. High-frequency vibration and noise in dentistry.
2005. 80 p. Acad. Diss.

C 181. Seppänen, Aku. State estimation in process tomography.
2005. 117 p. Acad. Diss.

C 182. Ibrahim, Mohamed Ahmed. Plant essential oils as plant protectants and growth activators.
2005. 143 p. Acad. Diss.

C 183. Vuorinen, Terhi. Induced volatile emissions of plants under elevated carbon dioxide and ozone concentrations, and impacts on indirect antiherbivore defence.
2005. 98 p. Acad. Diss.

C 184. Savinainen, Juha. Optimized methods to determine ligand activities at the cannabinoid CB1 and CB2 receptors.
2005. 83 p. Acad. Diss.

C 185. Luomala, Eeva-Maria. Photosynthesis, chemical composition and anatomy of Scots pine and Norway spruce needles under elevated atmospheric CO2 concentration and temperature.
2005. 137 p. Acad. Diss.